

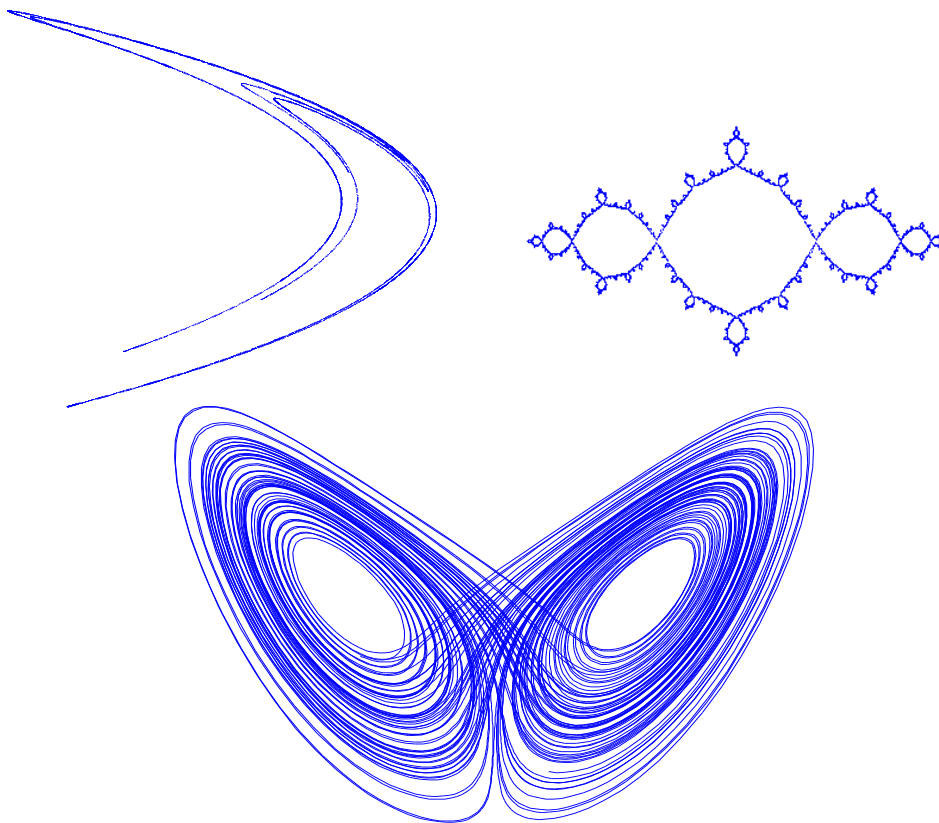


university of
 groningen

faculty of mathematics
 and natural sciences

Dynamics of Chaotic Systems and Fractals

Thomas G. de Jong



Bachelor Thesis in Applied Mathematics

August 2009

Dynamics of Chaotic Systems and Fractals

Summary

In this thesis we treat the dynamics of chaotic systems and fractals. Chaotic systems are defined as dynamical systems, which, although they are deterministic, show a certain non-predictable behaviour. Fractals are complicated geometric figures, that unlike conventional geometric shapes won't simplify when magnified. The characteristic behaviour of chaotic systems and fractals are treated; more specifically we study the Hénon map, Lozi map, Julia sets, Mandelbrot set and Lorenz attractor.

Bachelor Thesis in Applied Mathematics

Author: Thomas G. de Jong

Supervisor: Henk W. Broer

Date: August 2009

Institute of Mathematics and Computing Science

P.O. Box 407

9700 AK Groningen

The Netherlands

Contents

Preface	v
Introduction	vii
1 Dynamical systems: definitions and examples	1
2 The Hénon and Lozi maps	3
2.1 Hénon map and attractor	4
2.1.1 Attractor	6
2.1.2 Stable and unstable manifolds	8
2.2 Lozi map and attractor	14
2.3 Dimensions and measures of sensitivity	15
2.3.1 Dimensions	15
2.3.2 Sensitivity	21
2.3.3 Lyapunov dimension	28
2.3.4 Lyapunov bifurcation diagrams for the Hénon mapping and Lozi mapping . . .	29
2.4 Multiple attractors with fractal basin boundaries	37
2.4.1 The uncertainty exponent	38
2.4.2 The pendulum and three magnets	40
3 Julia Sets and Mandelbrot set	45
3.1 Newton method	45
3.1.1 Newton method for $z^2 - 1$	45
3.1.2 Newton method for $z^3 - 1$	46
3.2 Julia sets	49
3.2.1 Characterization of periodic points for Julia sets	50
3.2.2 Transitivity	53
3.2.3 Digression into topology: formalizing IFS	54
3.2.4 Computer graphical generation of Julia sets	57
3.2.5 Dynamics of Julia sets: equipotential curves and field lines	58
3.2.6 Dynamics of two Julia sets investigated	66
3.2.7 Julia sets: Connected sets and Cantor sets	68
3.3 Mandelbrot set	69
3.3.1 Numerical investigation of ∂M	70
3.3.2 External dynamics	72
3.3.3 Internal dynamics	76
3.3.4 Asymptotic similarity	79
4 The Lorenz attractor	89
4.1 Lorenz system	90
4.2 Lorenz attractor	91
4.2.1 Dynamics	91

4.2.2	Numerical investigation	94
4.2.3	Lyapunov exponents and numbers in flows	96
4.2.4	Attractor	98
4.3	Rössler attractor	99
4.4	A model for the Lorenz system	100
4.4.1	Creating a model for the Lorenz system	100
4.4.2	Return map	102
4.4.3	The Tucker attractor of the Lorenz model exists	104
4.4.4	One-dimensional dynamics	105
5	Concluding remarks	109
A	Lozi-map	111
A.1	Smoothed Lozi mapping	111
A.2	Proof $\mathcal{L}_{a,b} = \overline{W^u(X)}$	112
B	Base three expansion for the Triadic Cantor set	117
C	Numerical calculation of Lyapunov exponents	119
D	Riemann sphere	123
E	Path connectedness of $\hat{\mathbb{C}} \setminus K_f$	125
F	Self-similarity of Julia sets	127

Preface

A little learning is a dangerous thing, drink deep or do not taste the Pierian spring.

A. Pope, *An essay on criticism* (1711)

This Bachelor thesis has been written in the hope that any undergraduate maths student could read and come to understand it. The only prerequisites needed are an introductory course in metric spaces and topology, complex analysis and dynamical systems.

We have aimed to give a discussion of the dynamics of chaotic systems and fractals as complete as possible given the available time. Thus here and there we referred for a more extensive treatment to the literature. All in all this thesis has become a ‘lengthy’ piece of work, but of course this was not the doing of a single person. I would like to thank Prof. G. Vegter, Prof. H. Waalkens and A. E. Sterk who helped me during the course of the last three months either with supplying me with literature or helping me with the construction of algorithms or proofs. Furthermore I would like to thank my thesis advisor Prof. H. W. Broer not only for his guidance, but also for making me enthusiastic to explore the world of dynamical systems and fractals.

All the computer graphical images in this thesis were created with self-written MATLAB algorithms, although not completely without help. I would like to thank A. E. Sterk once again for his help on this.

Finally I would like to thank the following reviewers: E. A. Dijck, D. de Laat, H. Oosterhuis and A.E. Sterk.

Introduction

In this Bachelor thesis we study the dynamics of chaotic systems and fractals. Chaotic systems are defined as dynamical systems, which, although they are deterministic, show a specific non-predictable behaviour. This is due to the fact that they are highly sensitive to perturbations in initial states. This sensitivity manifests itself in the exponential growth of perturbations as time progresses. Fractals are shapes with infinitely complex boundaries, which unlike conventional geometrical shapes, won't simplify when magnified.

We present in this thesis the characteristic behaviour of a number of chaotic systems and fractals; more specifically we will be treating Hénon and Lozi maps in chapter 2, Julia sets and the Mandelbrot set in chapter 3 and the Lorenz attractor in chapter 4. Chapter 1 will briefly cover the definition of dynamical systems. In chapter 2 and chapter 3 we restrict ourselves in general to two- and one-dimensional systems; in chapter 4 we thoroughly investigate a three-dimensional system. The important definitions concerning chaotic systems will be given in chapter 2, however we will only restrict ourselves to a specific set of mappings (discrete mappings, see chapter 1), these definitions will be extended in chapter 4 to the general case. One may say that chapter 2 and chapter 4 are mainly devoted to the dynamics of chaotic systems and chapter 3 explores the dynamics of fractals. These chapters are not completely unrelated to each other since chaotic systems are closely related to fractals and vice versa. Although we give a lot of numerically assisted proofs we will only briefly discuss the theory behind the algorithms used and refer for a more extensive treatment to the literature. The same applies to the theoretical proofs, we mainly restrict ourselves to sketches and refer the reader to the literature for a full proof.

Chapter 1

Dynamical systems: definitions and examples

In dynamical systems theory one studies deterministic systems. This means that for a given initial state all future states are determined. All possible states together form the *state space* which is represented by M . A point $x \in M$ represented with respect to time, $x(t)$, shall be called an evolution; the curve $t \mapsto x(t)$ shall also be called an evolution. We now define an operator which can map an initial state to the corresponding state at time $t \in T$, where T is a given *time set*:

$$\Phi : M \times T \mapsto M.$$

This operator is called the *evolution operator* of the dynamical system. Most of the treated examples in this thesis will have a time set, T , given by \mathbb{Z} or \mathbb{R}^k with $k = 1, 2, \dots$, i.e. a discrete and a continuous time set. In the exceptional case we have that $T = \mathbb{Z}_+$.

We will discuss the two properties of the evolution operator. Firstly an initial state, $x \in M$, will stay unchanged under the evolution operator for a time interval of zero length. More formally

$$\Phi(x, 0) = x.$$

Secondly we have the property that

$$\Phi(\Phi(x, t_1), t_2) = \Phi(x, t_1 + t_2).$$

Let us define the evolution of the general dynamical system, which is given for an initial state $x \in M$ by the map $t \mapsto \Phi^t(x) := \Phi(x, t)$, thus an evolution. Specifically for a continuous time set, we can consider x as a point which ‘flows’ along t , hence Φ^t is also called the flow over the time t .

Given the above, we have the following definition of dynamical system.

Definition 1.1 (Dynamical system) *A dynamical system, denoted by (M, T, Φ) , consists of a state space M , a time set set $T \subseteq \mathbb{R}$, being an additive semi group, and an evolution operator $\Phi : M \times T \mapsto M$ satisfying the group property, i.e. $\Phi(x, 0) = x$ and $\Phi(\Phi(x, t_1), t_2) = \Phi(x, t_1 + t_2)$ for all $x \in M$ and for all $t_1, t_2 \in T$.*

We will present two examples of dynamical systems: one with a discrete time set and one with a continuous time set.

Example: Logistic mapping

The Logistic mapping is a mapping from $[0, 1]$ to $[0, 1]$ given by

$$x_{n+1} = \mu x_n(1 - x_n), \quad \mu \in (0, 4], \quad n = 0, 1, 2, \dots$$

This is a simplified model which describes the population of a species taking overpopulation into account [8]. The state space is given by $M = [0, 1]$. We are now dealing with a discrete time set defined for $n = 0, 1, 2, \dots$, hence $T = \mathbb{Z}_+$. The evolution operator must then map the solution one step ahead in time. Hence the evolution operator is given by $\Phi(x_{n-1}, 1) = \Phi^1(x_{n-1}) = x_n$, this specific evolution is also referred to as time-one map.

Example: Free undamped pendulum

The differential equation which describes the undamped pendulum is given by

$$\phi'' = -\omega^2 \phi.$$

Thus it is a continuous system, consequently the time set is given by $T = \mathbb{R}$. The evolution operator must correspond to an unique determination of the future; defining $\Phi(\phi(0), t) = \phi(t)$ won't suffice, since the flow is also dependent on the initial velocity. Hence $M = \mathbb{R}^2$ and we have $\Phi(\phi(0), \phi'(0), t) = (\phi(t), \phi'(t))$.

For more examples we refer to [8].

Chapter 2

The Hénon and Lozi maps

The Hénon mapping defines a dynamical system, (M, T, Φ) , with $M = \mathbb{R}^2$, $T = \mathbb{Z}$ and evolution operator

$$\Phi^1 = H_{a,b} : (x, y) \mapsto (y + 1 - ax^2, bx).$$

The equation $H_{a,b}(x, y) = (y + 1 - ax^2, bx)$, which is referred to as the Hénon transformation or Hénon mapping, was originally suggested by Michel Hénon as a model which is as simple as possible, yet exhibits the same essential properties as the Lorenz system [22]. We investigate the Lorenz system in chapter 4.

Applying the Hénon transformation for parameters $a = 1.4$ and $b = 0.3$ to an initial state, we observe that the orbit is attracted to the invariant shape displayed in figure 2.1.

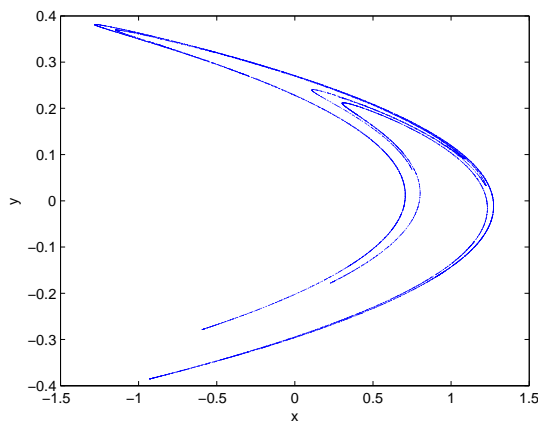


Figure 2.1: Recursively applying $H_{1.4,0.3}(x, y)$ 15000 times to a single initial state: the shape which attracts the orbit for the given parameters is called the Hénon attractor.

The invariant shape to which the Hénon map $H_{1.4,0.3}(x, y)$ is attracted in the figure above is called the Hénon attractor. This attraction to an invariant set takes also place for other parameters, since these set look like the Hénon attractor we refer to these as Hénon-like attractors.

In this chapter we first direct our attention to some of the elementary properties of the Hénon map with corresponding attractors. We will come to the conclusion that this a complicated systems and hence we will aim to simplify it by creating a piecewise linear version of the Hénon map: the Lozi

map. The Lozi map lends itself much more easily to theoretical investigation. In this chapter, we will also introduce techniques with which we can measure certain characteristic behaviour. We will use these methods to investigate the Lozi and Hénon map in the (a, b) -parameter plane.

We will see that for the Hénon mapping all initial states are attracted to the attractor, with the exception of the points which diverge to infinity. However it is also possible that there exists two sets which converge to two different Hénon-like attractors for a single Hénon map; this occurrence is discussed in the last section of this chapter. The dynamics of these multiple attractors is also seen back in a physical model: the pendulum with three magnets. This model is investigated at the end of the last section.

2.1 Hénon map and attractor

We first discuss the Hénon transformation or Hénon map. This map can be decomposed into three sub-transformations.

1. Bend up or fold up:

$$H_1(x, y) = (x, y + 1 - ax^2).$$

2. Contracting in x direction (for $|b| < 1$):

$$H_2(x, y) = (bx, y).$$

3. Reflecting in the line $y = x$:

$$H_3(x, y) = (y, x).$$

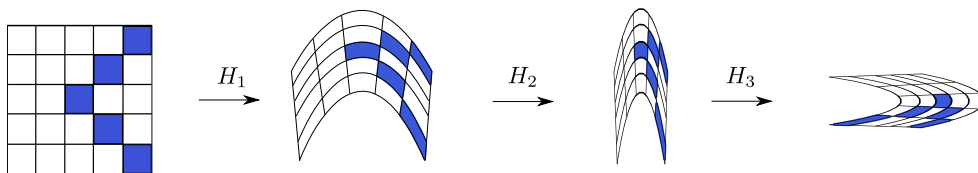


Figure 2.2: The three sub-transformations that make up the Hénon transformation: bending (H_1), contracting in x direction (H_2) and finally reflecting (H_3).

Together these form the Hénon transformation, $H_{a,b}(x, y) = H_3(H_2(H_1(x, y)))$. This process of recursively applying transformations to an object is called an iterated function system, abbreviated IFS. We will formalize the definition of an IFS in section 3.2.3.

To get a better idea of the transformation which takes place at each iteration, we can consider the paradigm of kneading dough. You first stretch the dough in such a way to create a parabolic shape (H_1). Then you contract it by folding it back together again (H_2) and finally you flip the dough (H_3). After several iterations one sees that it converges to an invariant shape, the Hénon attractor.

We get a better visual idea of the bending, contracting and reflecting if we consider applying the Hénon map to a square. Using once again the parameters $a = 1.4$ and $b = 0.3$, we obtain figure 2.3. We see that the square gets stretched and folded at each iteration until it finally begins to resemble the Hénon attractor.

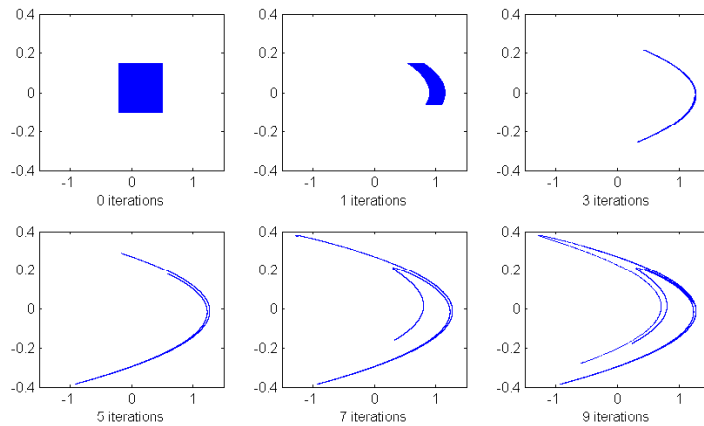


Figure 2.3: Applying the Hénon transformation for a number of iterations to a square. Observe the strong presence of folding and stretching at each iteration.

From figure 2.3 we observe that the bending is very clearly visible. The bending in the Hénon mapping has as a consequence that points which are initially near to each other will move away. We can verify this numerically. Take an initial state (x_0, y_0) and a perturbed initial state $(x_0 + \epsilon, y_0)$, take ϵ for example 10^{-4} . In figure 2.4 we have numerically generated the orbits of the initial state (blue line) and perturbed initial state (red line) corresponding to the map $H_{1.4,0.3}$, for clarity reasons we have connected two consecutive iterations with a line.

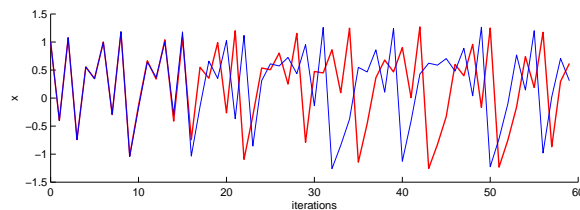


Figure 2.4: Sensitivity on initial values for the map $H_{1.4,0.3}$: orbit of initial state (blue line) and perturbed initial state (red line); for clarity reasons we have connected two consecutive iterations with a line. One observes that at the beginning these orbits are almost identical, but after a while they show totally different behaviour.

One sees that at the beginning both orbits are almost identical, but as we continue iterating they become totally different. This phenomenon is called sensitivity and is characteristic for a chaotic system. We treat this subject in more detail in section 2.3.2.

2.1.1 Attractor

We have been using the word attractor already a few times, without giving a formal description. What is an attractor? An attractor attracts an open area, say U , to itself. Informally an attractor is the biggest attracting ω -limit in U . The ω -limit set is defined as follows.

Definition 2.1.1 (ω -limit set discrete T) Let $\Phi^1 = f : M \rightarrow M$ and $x_0 \in M$. The ω -limit set of the orbit $\{f^n(x_0)\}$ is given by

$$\omega(x_0) = \{y \in M \mid \exists \{n_j\}_{j \in \mathbb{N}} \subset \mathbb{Z}_+, \text{ such that } n_j \rightarrow \infty \text{ and } f^{n_j}(x) \rightarrow y\}.$$

Informally one can describe the ω -limit set of an orbit as the set of points to which the orbit gets arbitrarily close to infinitely many times.

A simple example of an ω -limit set of an orbit is a sink. The ω -limit set of an orbit may or may not have points in common with the corresponding orbit. Indeed in the case of an orbit converging to a sink, the ω -limit set will have no points in common with the corresponding orbit. Although it is tempting to think that ω -limit sets correspond only to attracting orbits, this is not true since any periodic orbit is an ω -limit set [1].

We will state some properties concerning ω -limit sets:

- non-empty.
- compact.
- invariant under f .
- transitive, meaning that for any points $x_1, x_2 \in \omega(x)$ and open neighbourhoods $U_j, j = 1, 2$ such that $x_j \in U_j$, there exists an orbit which begins in U_1 and passes through U_2 .

We won't treat the proofs of these properties as they can be found in [14, 1].

We come now to the definition of attractor.

Definition 2.1.2 (Attractor, discrete T) Let $\Phi^1 = f : M \rightarrow M$ and let $x_0 \in M$, then $\omega(x_0)$ is called an attractor if there exists an arbitrarily small neighbourhood U of $\omega(x_0)$ such that $f(U) \subset U$ and such that

$$\bigcap_{i=0}^{\infty} f^i(U) = \omega(x_0).$$

The condition makes sure that we are dealing with the biggest ω -limit set in U .

Remarks:

- This definition of attractor is defined for a discrete time set but can be extended to a continuous time set. However since we will only be considering discrete cases in this chapter we will be postponing the discussion of the continuous cases to section 4.2.4.
- The condition 'such that $\bigcap_{i=0}^{\infty} f^i(U) = \omega(x)$ ' can be replaced by 'such that for all $y \in U$ one has $\omega(y) \subset \omega(x)$ ' [8].
- There exists many variations of the definition of an attractor. Some examples of literature which use different definitions of attractors are [8], [14] and [1].

Attractors for the Hénon map also exist for parameters other than those corresponding to the Hénon attractor. We write for the attractor corresponding to a Hénon map, with parameters a and b , $\mathcal{H}_{a,b}$. These are called Hénon-like attractors. It is also not the case that for all a, b we attain an attractor. For example take the maps $H_{a,b}$ with $|b| > 1$, it then follows from H_3 that we will be dealing with a repelling set.

For the Hénon attractor, $a = 1.4$ and $b = 0.3$, we write \mathcal{H} , the corresponding mapping shall be written as H .

The name Hénon attractor is slightly misleading, since it is still unproven that it is an attractor in the sense of definition 2.1.2 [8]. However we can make this hypothesis numerically plausible. Following definition 2.1.2 we need to find a $U \subset \mathbb{R}^2$ such that $H(U) \subset U$ and $\mathcal{H} \subset U$. This region U is called a trapping region, since once an orbit enters U it can never leave. An example of such a trapping region for the Hénon attractor was suggested by M. Hénon himself [22]. Take the polygon $ABCD$ with vertices given by

$$\begin{aligned} A &= (-1.33, 0.42), & B &= (1.32, 0.133), \\ C &= (-1.245, -0.14), & D &= (-1.06, -0.5). \end{aligned}$$

The image under H is bounded by four parabolae. We have given the numerical result in figure 2.5.

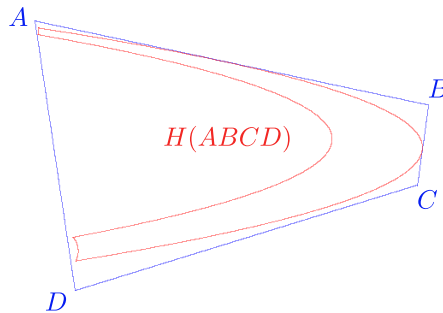


Figure 2.5: Trapping region $ABCD$ with corresponding image $H(ABCD) \subset ABCD$.

Thus we have that $H(ABCD) \subset ABCD$. We then may conclude that

$$\mathcal{H} \subset \bigcap_{i=0}^n H^i(ABCD).$$

Numerically it seems plausible that as $n \rightarrow \infty$ equivalence of the above holds. We have now completely omitted the discussion whether the Hénon attractor is indeed an ω -limit set and this is still an open problem [8].

Let us now continue with questions arising from the previously constructed trapping region. For we could ask ourselves which points converge to the attractor and which do not. In the numerical generated figure 2.6 we have drawn the Hénon attractor in red and the points which converge to the Hénon attractor in blue. The set which converges to the Hénon attractor is called the basin of attraction.

Definition 2.1.3 (Basin of attraction) *When $\Lambda \subset M$ is an attractor, the basin of attraction of Λ is given by the set*

$$A(\Lambda) = \{x \in M \mid \omega(x) \subset \Lambda\}.$$

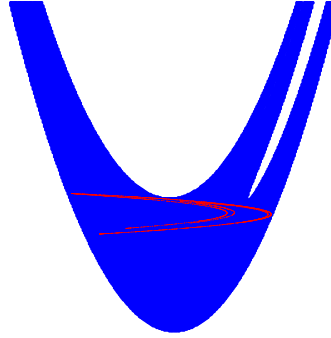


Figure 2.6: Basin of attraction of the Hénon attractor in blue, with the Hénon attractor in red.

Basins of attraction and their boundaries will form an important part in our investigation of systems in later sections.

Let us now once again return to the trapping region. One can use the existence of a trapping region to prove that the Hénon attractor has zero area as we shall show in the proof of the proposition below.

Proposition 2.1.1 *The Hénon attractor has empty interior.*

Proof. From linear algebra we have the result that the area near a point is reduced (or expanded) by a factor equal to the determinant of the Jacobian matrix in the absolute value. For the Hénon map we obtain

$$|\det(DH(x, y))| = \left| \det \begin{pmatrix} -2ax & 1 \\ b & 0 \end{pmatrix} \right| = |b|.$$

Thus the area contraction per iterate corresponds to $|b| = 0.3$.

Each iteration contracts the area by 0.3, meaning that the area of $H^i(ABCD)$ will be reduced after i -steps by 0.3^i . Thus as we increase the steps i , the area will converge to zero. $\mathcal{H} \subset \bigcap_{i \geq 0} H^i(ABCD)$, thus the attractor has empty interior. \square

2.1.2 Stable and unstable manifolds

Let us investigate the fixed points of H . Solving $H(x, y) = (x, y)$ yields

$$x = \frac{-0.7 \pm \sqrt{6.09}}{2.8}, \quad y = 0.3x.$$

Approximations of the above result gives the two solutions: $(0.63, 0.19)$ and $(-1.13, -0.34)$. The former is a point of interest since it lies on the attractor as is numerically verified in figure 2.7, henceforth we call this fixed point p .

Let us now turn to the dynamics around the fixed point p on the Hénon attractor. DH_p has two eigenvalues which we will denote by λ_1, λ_2 . Straightforward computation yields that $|\lambda_1| > 1 > |\lambda_2|$ implying that we are dealing with a fixed saddle point. So there will be a set diverging from this point corresponding to $|\lambda_1| > 1$, the unstable manifold and there will be a set converging to this point which corresponds to $|\lambda_2| < 1$, the stable manifold. We are now ready for some definitions.

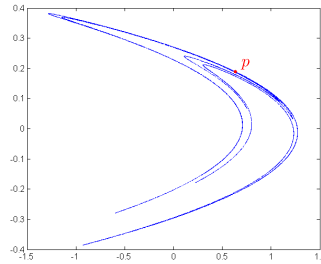


Figure 2.7: The fixed point p located on the Hénon attractor.

Definition 2.1.4 (Local stable and local unstable manifold) Let $f : \mathbb{R}^2 \rightarrow \mathbb{R}^2$ be a diffeomorphism with a fixed saddle point p . Take U to be an open neighbourhood of p . The local unstable manifold is then defined by

$$W_U^u(p) = \{q \in U \mid f^j(q) \in U \quad \forall j \leq 0\}$$

The local stable manifold is then defined by

$$W_U^s(p) = \{q \in U \mid f^j(q) \in U \quad \forall j \geq 0\}$$

Remark: In the literature the unstable, stable manifold are also denoted as $W_{\text{loc}}^u(p)$, $W_{\text{loc}}^s(p)$ respectively.

Consider the linearised Hénon map around the point p :

$$H_{\text{lin}}(\xi, \eta) = (\lambda_1 \xi, \lambda_2 \eta).$$

Here ξ and η are new coordinates chosen in such a way that the origin is translated to p and the coordinate axes point in the directions of v_1 and v_2 , the eigenvectors of λ_1 and λ_2 . We have depicted the evolutions near the saddle fixed point of H_{lin} in figure 2.8.

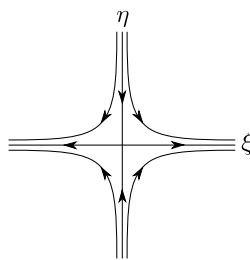


Figure 2.8: Evolutions near the saddle fixed point of the linearised Hénon map in (ξ, η) -coordinates.

One observes that the ξ - and η -axis are H_{lin} -invariant. Points on the ξ -axis will move away from p under iteration of H_{lin} , while points on η -axis are attracted to p . In this linear case the local manifolds are given by the eigenvectors v_1 and v_2 . All of this holds when higher order terms are neglected. However something still remains of this when higher terms are no longer neglected, as we see from the following theorem.

Theorem 2.1.1 (Property invariant local manifolds) *For a diffeomorphism f , with saddle fixed point p , eigenvalues λ_1, λ_2 and eigenvectors v_1 and v_2 as above, then there exists a neighbourhood U of p such that for $W_U^u(p), W_U^s(p)$ there exists a smooth curve that contains the point p and is tangent to v_1, v_2 , respectively. Furthermore we have that for all $q \in W_U^u(p), q \in W_U^s(p)$, respectively, $\lim_{n \rightarrow -\infty} f^j(q) = p, \lim_{n \rightarrow \infty} f^j(q) = p$.*

We won't supply the reader with the proof but instead refer to [25].

The *global stable* and *unstable manifolds* are then defined by

$$W^u(p) = \bigcup_{j>0} f^j(W_U^u(p)) \quad \text{and} \quad W^s(p) = \bigcup_{j<0} f^j(W_U^s(p)).$$

Numerical computation of stable and unstable manifolds

To get a better understanding how to construct these global manifolds let us present a method how to generate these numerically. We take once again the fixed saddle point p with eigenvalues $\lambda_1 > 1 > \lambda_2$ and corresponding eigenvectors v_1 and v_2 . We will just present the case for $W^u(p)$, the case for $W^s(p)$ can be obtained in a similar manner. For the numerical approximations of $W^u(p)$ we first take a short line segment $[p - \epsilon v_1, p + \epsilon v_1]$. The smaller the ϵ the better the approximation for the $W^u(p)$ (the order of the error is given by $O(\epsilon^2)$ [8]). Divide the line segment into N equidistant points, iterating these k -times forwards and connecting these points will give us $W^u(p)$. Of course the approximation of the global manifold is dependent on the choices of parameters: ϵ, k and N . It can be proven that we can approximate a segment of $W^u(p)$ to any given length up to an arbitrary precision by an appropriate choice of ϵ, k and N . A proof of this statement makes use of ideas used in the proof of theorem 2.1.1.

Remark: Under the circumstances that we have a linear local unstable manifold decreasing the ϵ in $[p - \epsilon v_1, p + \epsilon v_1]$ won't decrease the error, for $[p - \epsilon v_1, p + \epsilon v_1]$ is equal to the local unstable manifold in an ϵ neighbourhood of p . By definition of $W^u(p)$ the numerical result will be the best possible approximation.

We have numerically approximated the global unstable and stable manifold of $H_{1.4,0.3}$ in figure 2.9.

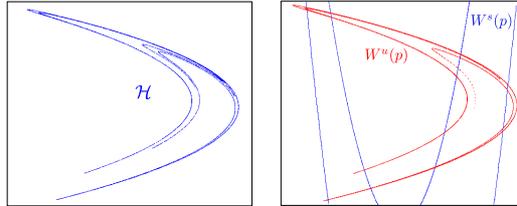


Figure 2.9: Left: The Hénon attractor \mathcal{H} . Right: The unstable manifold, $W^u(p)$, and stable manifold, $W^s(p)$ of the corresponding Hénon map. Observe the similarity between the Hénon attractor and the unstable manifold.

Observing $W^u(p)$ one immediately sees a similarity with the Hénon attractor, one might even hypothesize that

$$\overline{W^u(p)} = \mathcal{H}. \quad (2.1)$$

The above statement is still an open problem. Specifically the case $\overline{W^u(p)} \supseteq \mathcal{H}$. In 1991 M. Benedicks and L. Carlson proved that this is true for a variety of Hénon like mappings, \mathcal{H}_b^a , for $|b|$ is small and for many values of a . The proof makes use of a relation between the Logistic mapping and Hénon mapping. For the proof we shall refer to [6].

Proving that $\overline{W^u(p)} \supseteq \mathcal{H}$ is not too difficult, we can make use of the earlier shown contracting property of the Hénon attractor. We will prove this in proposition 2.1.2.

Homoclinic orbits

B. Szewc and F. Tangerman proved around 1981 that $\overline{W^u(p)} \supseteq \mathcal{H}$. Their proof makes use of homoclinic points.

Definition 2.1.5 (Homoclinic points) *Let p be a hyperbolic fixed point, then we say that q is a homoclinic point, or homoclinic to p , if $p \neq q \in W^s(p) \cap W^u(p)$.*

A lot of interesting dynamics take place near the orbit corresponding to the homoclinic point, i.e. homoclinic orbit. It is not too hard to see that for a homoclinic point, q , $f^n(q)$ with $n \in \mathbb{N}$ will also be a homoclinic point. Thus if we can prove that if $W^s(p)$ and $W^u(p)$ intersects once at a point other than p , then these manifolds will intersect infinitely many times. Hence one speaks of the dynamics around a homoclinic orbit. An example of these complex web-crossings which result from the homoclinic orbit is displayed in figure 2.10.

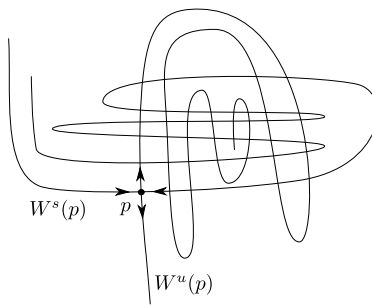


Figure 2.10: If $W^s(p)$ and $W^u(p)$ intersects once at a point other than p , then these manifolds will intersect infinitely many times: each forward iterate and each backward iterate is a homoclinic point.

Smale showed that the existence of a homoclinic orbit implies the presence of a horseshoe like map. The horseshoe map is a diffeomorphism $h : \mathbb{R}^2 \rightarrow \mathbb{R}^2$ which maps a rectangle, D , onto a horseshoe shape as figure 2.11 suggests. Furthermore we assume that h preserves vertical and horizontal directions. On the components in figure 2.11 h is a contraction in horizontal direction and an expansion in vertical direction. For a more extensive treatment of the horseshoe map of Smale we refer to [8].

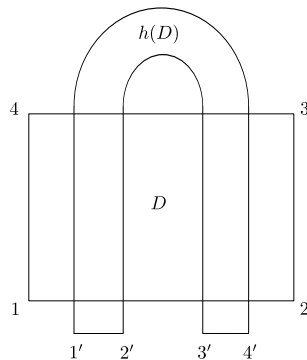


Figure 2.11: The vertices 1, 2, 3, 4 of rectangle D are mapped onto the vertices $1'$, $2'$, $3'$, $4'$ of the horseshoe shape $h(D)$.

We can construct a horseshoe-like map near any homoclinic orbit, this is indicated in figure 2.12.

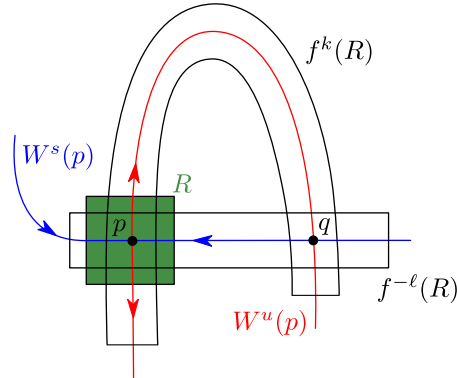


Figure 2.12: Under forward, backward iteration of f , the square R is stretched along $W^u(p)$, $W^s(p)$, respectively. There exist k, ℓ such that $f^k(R)$ and $f^{-\ell}(R)$ contain the homoclinic point q ; consequently $f^{k+\ell}$ is a horseshoe-like map with domain $f^{-\ell}(R)$ and image $f^k(R)$.

First take a square, R , containing a fixed point p of an invertible map f with an homoclinic orbit. Under iteration of f , R will stretch along the unstable manifold, $W^u(p)$, and under iteration of f^{-1} , R will stretch along the stable manifold, $W^s(p)$. Then there exists a k such that $f^k(R)$ extends along $W^u(p)$ such that it includes a homoclinic point q . Similarly we have that there exists a ℓ such that $f^{-\ell}(R)$ extends along $W^s(p)$ such that it also includes q . Observe from figure 2.12 that $f^{k+\ell}$ is a horseshoe like map with domain $f^{-\ell}(R)$ and image $f^k(R)$. For an extensive dynamical investigation of the behaviour around homoclinic orbits we refer to [30].

Let us now continue the Szewc and Tangerman argument; we present the proposition with proof below.

Proposition 2.1.2 *Let $f : \mathbb{R}^2 \rightarrow \mathbb{R}^2$ be a diffeomorphism with a hyperbolic fixed saddle point p with the following properties:*

- $W^u(p)$ and $W^s(p)$ have a homoclinic intersection q with $p \neq q$.
- $|\det(Df)| < 1$.
- $W^u(p)$ remains in a bounded region of \mathbb{R}^2 .

Then there exists an open non-empty set $U \subset \mathbb{R}^2$ such that for $x \in U$ we have that $\omega(x) \subseteq \overline{W^u(p)}$ i.e. for $n \rightarrow \infty$ the distance between $f^n(x)$ and $W^u(p)$ becomes zero.

Proof. Take as $U \subset \mathbb{R}^2$ the bounded open subset in between segments of $W^u(u)$ and $W^s(u)$; this is possible since we have a homoclinic intersection. We refer to the arcs which enclose U as ℓ_u, ℓ_s respectively, as is indicated in figure 2.13.

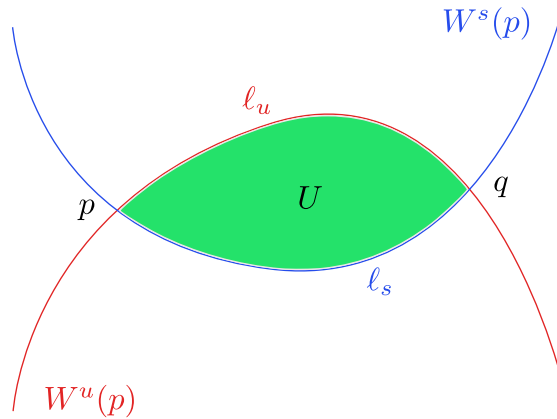


Figure 2.13: In this figure we have visually represented all the ‘components’ in the proof of the proposition: p is the fixed point of $\omega(x)$, q is the homoclinic intersection and ℓ_u and ℓ_s are the arcs corresponding to the bounded region by the unstable manifold $W^u(p)$ and stable manifold $W^s(p)$ respectively. We have however just drawn a single homoclinic intersection, of course we actually have infinite homoclinic intersections, the union of all these arcs will make ℓ_u , ℓ_s respectively and the union of the enclosed areas will be U .

Let us then consider $f^n(U)$ for $n \geq 0$. We know that $f^n(\ell_s)$ for big n will converge to p , furthermore $f^n(\ell_u)$ will stay bounded since $W^u(p)$ is bounded. We can now conclude that $f^n(U)$ stays in a bounded part of \mathbb{R}^2 . Thus we have that $|\det(Df)| < 1$ on $\bigcup_{n \geq 0} f^n(U)$ or in other words for $n \rightarrow \infty$ we have that the area of $f^n(U)$ will go to zero.

We have that for $x \in U$ and $n > 0$, for n big, it holds that $f^n(x)$ will get arbitrarily close to $W^u(p)$, since the boundary of $\overline{W^s(p)}$, $f^n(\ell_s)$, has decreasing length. Thus we obtain by the definition of the ω -limit set that $\omega(x) \subseteq \overline{W^u(p)}$. \square

The above proposition can be applied to the Hénon attractor. It still needs to be proven that the Hénon attractor contains a homoclinic point. This is shown in [28], but we have also made this numerically plausible in figure 2.9. We already have seen that $|\det(DH)| < 1$ and $W^u(p)$ is bounded, hence $\overline{W^u(p)} \supseteq \mathcal{H}$.

2.2 Lozi map and attractor

As we have now seen the Hénon mapping is not as simple as it looks. Instead we can investigate a simplified model: the Lozi mapping. The Lozi mapping is a piecewise linear model of the Hénon mapping given by the evolution operator:

$$\Phi^1 = L_{a,b} : (x, y) \mapsto (1 + y - a|x|, bx) .$$

The only difference between the Hénon and Lozi mapping is that the x^2 -term is replaced by the $|x|$ -term. R. Lozi suggested the values $a = 1.7$ and $b = 0.5$ to obtain an attractor which looks like a linearised version of the Hénon-attractor, see figure 2.14.

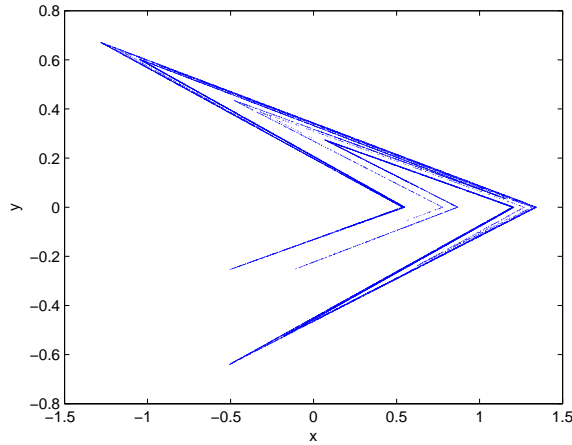


Figure 2.14: Recursively applying $HL_{1.7,0.5}(x, y)$ 15000 times to a single initial state. The shape which attracts the orbit for the given parameters is called the Lozi attractor.

We denote the attractor corresponding to a Lozi mapping, the Lozi-like attractor, by $\mathcal{L}_{a,b}$. Specifically for the Lozi-attractor, the attractor corresponding to the map $\mathcal{L}_{1.7,0.5}$, we write \mathcal{L} .

The Lozi mapping is not everywhere differentiable since the derivative at $|x|$ is undefined for $x = 0$. Due to this loss of smoothness we cannot apply certain results of dynamical systems theory. Another consequence of the loss of smoothness is that there won't exist a conjugacy between the Hénon and Lozi map. However we can create a smooth map which approximates the Lozi map. A construction of such a map can be found in Appendix A.1, for a more extensive investigation of this smoothed Lozi map we refer to [3].

For the Lozi mapping we can prove for specific parameter values that it is indeed an attractor. The proof is based on showing that $\mathcal{L}_{a,b} = \overline{W^u(X)}$, where X corresponds to the fixed saddle point in $\mathcal{L}_{a,b}$. The proof of $\mathcal{L}_{a,b} = \overline{W^u(X)}$ consists out of two parts: first we make assumptions on the parameters such that we can construct a trapping region, see figure 2.15, and then we use this trapping region to prove the equality $\mathcal{L}_{a,b} = \overline{W^u(X)}$. An important property is that we can make $W_U^u(X)$ and $W_U^s(X)$ explicit since the system is piecewise linear. The proof is rather long and technical, hence we have postponed it to Appendix A.2.

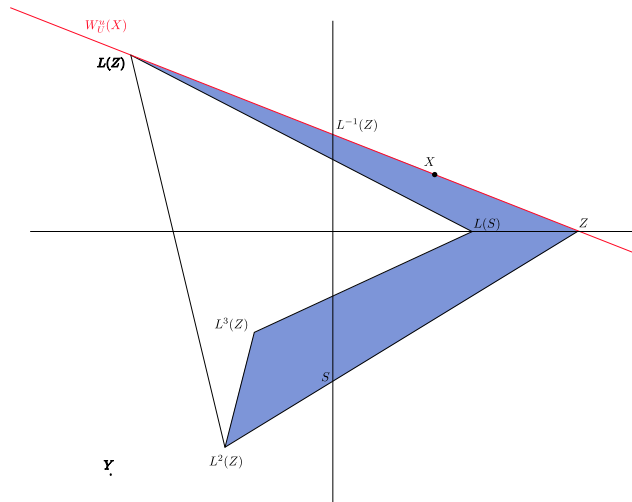


Figure 2.15: This figure is used in the construction of the trapping region of the Lozi map. X and Y are saddle fixed points, with X the fixed point in $\mathcal{L}_{a,b}$ with unstable manifold $W_u^u(X)$. The triangle $ZL(Z)L^2(Z)$, call this F , gets mapped onto the polygon $ZL(Z)L(S)L^3(Z)L^2(Z)$. Observe that this isn't a trapping since $L(F) \subseteq F$; this is due to the fact that $W_u^u(X)$ is f invariant. However we can prove that there exists an open neighbourhood of F which is a trapping region, see Appendix A.2.

2.3 Dimensions and measures of sensitivity

In the previous section we mainly explored statements which are closely connected to attractors with saddle points. We now investigate properties which say something more globally about the shape and behaviour of orbits in attractors.

2.3.1 Dimensions

On first look the Hénon attractor appears to be a set of connected sections of parabolae. However if we magnify part of the Hénon attractor more 'curves' become visible, see figure 2.16.

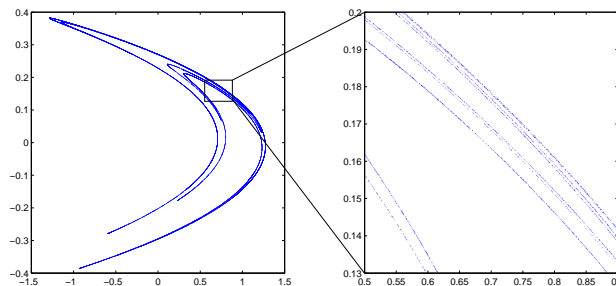


Figure 2.16: Magnification of the Hénon attractor. Observe the emerging fractal structure which is a result of the bending which takes place in the Hénon transformation.

These infinite sections of parabolae are the result of the folding in the Hénon map. Hence the Hénon attractor isn't a conventional geometric object, which will simplify if magnified, but a fractal.

We would like to define a measure for the ‘denseness’ of a fractal. One can quantify this by a concept of fractal dimension, which expresses that if an object lies more dense in \mathbb{R}^n the closer the dimension will be to n and vice versa.

Fractal and Boxcounting dimension

Let us define the fractal dimension.

Definition 2.3.1 (Fractal dimension) *Take $A \subset \mathbb{R}^n$ with A a non-empty bounded set, we denote the minimum number of balls with radius $\epsilon > 0$ needed to cover A by $N(A; \epsilon)$. The fractal dimension of A is then given by*

$$D_f(A) = \lim_{\epsilon \rightarrow 0} -\frac{\log(N(A; \epsilon))}{\log \epsilon}.$$

For every $\epsilon > 0$, $N(A; \epsilon)$ is finite, because A is bounded. We have that $N(A; \epsilon) \geq 1$, thus $D_f(A) \geq 0$. Furthermore one can prove that for $A \subset \mathbb{R}^n$ we have that $D_f(A) \leq n$ [5], hence $0 \leq D_f(A) \leq n$.

For ϵ ‘small enough’ we can make have the approximation

$$N(A; \epsilon) \approx C \cdot \epsilon^{-D_f(A)}. \quad (2.2)$$

We conclude from approximation 2.2 that for $\epsilon \rightarrow 0$, $N(A; \epsilon)$ will go to infinity. However for the special case that A is finite $N(A; \epsilon)$ will be bounded.

Generating a cover of open balls is not always such a handy method to find $N(A; \epsilon)$, especially if we want to numerically calculate the fractal dimension, but one can prove that the fractal dimension will stay unchanged if we take a cover of just touching n -dimensional cubes. This leads us to the following theorem.

Theorem 2.3.1 (Boxcounting Dimension) *Take $A \subset \mathbb{R}^n$ with A a non-empty bounded set, we shall denote the number of closed just touching n -dimensional cubes with sides length $\epsilon > 0$ needed to cover A by $\tilde{N}(A; \epsilon)$. We then define the boxcounting dimension by*

$$D_B(A) = \lim_{\epsilon \rightarrow 0} -\frac{\log(\tilde{N}(A; \epsilon))}{\log \epsilon}.$$

We then have that $D_B(A) = D_f(A)$.

The proof is a bit technical, we refer to [5]. However one can also view the boxcounting dimension as a definition in a different metric to the fractal dimension, since balls are squares in a different metric. Consequently the properties of the fractal dimension also apply to the boxcounting dimension.

We present two examples in which we theoretically determine the boxcounting dimension.

Example: Boxcounting dimension of the unit square

Denote the unit square by $S(1)$. Let us take a cover of squares with sides of length ϵ satisfying $\frac{1}{n+1} \leq \epsilon \leq \frac{1}{n}$ for $n > 0$. Then we will have that $n^2 \leq \tilde{N}(S(1); \epsilon) \leq (n+1)^2$, rewriting this inequality we obtain

$$\left(1 - \frac{1}{\epsilon}\right)^2 \leq n^2 \leq \tilde{N}(S(1); \epsilon) \leq (n+1)^2 \leq \left(\frac{1}{\epsilon} + 1\right)^2.$$

By the definition of the boxcounting dimension we have

$$-\lim_{\epsilon \rightarrow 0} \frac{\log\left(\frac{1}{\epsilon} - 1\right)}{\log(\epsilon)} \leq D_B(S(1)) \leq -\lim_{\epsilon \rightarrow 0} \frac{\log\left(\frac{1}{\epsilon} + 1\right)}{\log(\epsilon)}.$$

The left and right limit converge to 2, thus we obtain the expected result that $D_B(S(1)) = 2$. From this statement it follows that any bounded set $A \subset \mathbb{R}^2$ with non-empty interior has boxcounting dimension 2. Place A inside a square and then draw a square inside the interior, this leads to an upper and lower bound from which it follows that that $D_B(A) = 2$.

Example: Boxcounting dimension of the Triadic Cantor set

Define C_n by

$$C_n = \begin{cases} C_0 = [0, 1], \\ C_n = \frac{1}{3}C_{n-1} \cup (\frac{2}{3} + \frac{1}{3}C_{n-1}) \text{ for } k \geq 0. \end{cases}$$

We have represented this construction process of C_n in figure 2.17.



Figure 2.17: Construction of the Triadic Cantor set by C_n .

The Triadic Cantor set (also called the Middle-third Cantor set) is defined as $C = \bigcap_{k=0}^{\infty} C_k$. Observe by construction of the Cantor set that if part of the boundary is magnified it won't simplify, hence the Cantor set is a fractal. As the name implies there also exist other Cantor sets, which remove different parts of the initial segment C_0 , these are called the Middle- α Cantor sets [23].

The length of each of the connected components of the Triadic Cantor sets is given by $\lim_{n \rightarrow \infty} 1/3^n = 0$. The Triadic Cantor set is uncountable, for a proof see Appendix B. We conclude that C is an uncountable set with Lebesgue measure zero. This implies that C still contains points other than the endpoints of each connected component, take for example the point $1/4$. For an extensive discussion we refer to [18].

We will now provide a sketch for the theoretical determination of the boxcounting dimension of the the Triadic Cantor set. A full proof can be found in [18].

Let us first find a cover for C_n . C_n contains 2^n components with length $\epsilon_n = 3^{-n}$, thus $\tilde{N}(C_n; 3^{-n}) = 2^n$. One can use this cover for C since $C \subset C_n$, furthermore a better cover of length ϵ_n won't exist. Assuming that no better ϵ cover exists, a straightforward computation yields:

$$D_B(C_n) = \lim_{n \rightarrow 0} -\frac{\log(\tilde{N}(C; \epsilon_n))}{\log(\epsilon_n)} = \frac{\log(2)}{\log(3)}.$$

Thus the Triadic Cantor set has a dimension which is not a positive integer. This is the case for many fractals. The word fractal is derived from the Latin word 'fractus' meaning broken, since fractals in general have a dimension not equal to a positive integer, a 'broken' dimension.

Remark: There also exist fractals which have a dimension equal to a positive integer. For example the Mandelbrot set is a subset of $\mathbb{C} \cong \mathbb{R}^2$ and it has a boundary with fractal dimension 2.

Numerical determination of the boxcounting dimension

Numerically assisted proofs of the boxcounting dimension for complex fractals are in general more tempting to perform than a proof with pen and paper. We present an outline on the numerical approximation of the boxcounting dimension.

Suppose we know M points of the set $A \subset \mathbb{R}^n$, denote $A_M = \{x_i \in A | 1 \leq i \leq M\}$. Divide \mathbb{R}^n into n -dimensional cubes with sides of length ϵ . For a small ϵ but not too small we have $\tilde{N}(A_M; \epsilon) \approx \tilde{N}(A; \epsilon)$. Determining the boxcounting dimension directly by the definition yield the the equation:

$$D_B(A_M) \approx -\frac{\log(\tilde{N}(A_M; \epsilon))}{\log(\epsilon)}. \quad (2.3)$$

To see why this will give unsatisfactory results, let us give a different approximation of the boxcounting dimension. By approximation (2.2) we have $\tilde{N}(A_M; \epsilon) \approx C \cdot \epsilon^{-D_B(A_M)}$ thus we have that

$$D_B(A_M) \approx -\frac{\log(\tilde{N}(A_M; \epsilon)) - \log(C)}{\log(\epsilon)}. \quad (2.4)$$

For $\epsilon \rightarrow 0$ the value of $\log(C)/\log(\epsilon)$ in (2.4) will disappear and both approximations are equivalent. However if would increase ϵ equation (2.3) will give a bad approximation, since the contribution of $\log(C)/\log(\epsilon)$ won't be negligible in approximation (2.4). Thus we need to use approximation (2.4), but how can we calculate this if the value of C is unknown? This problem can be overcome by using a method which not just uses a single $\tilde{N}(A_M; \epsilon)$, but a series of coverings. Let us for example take $\epsilon_0 > \epsilon_1$, then we have that

$$\begin{aligned} D_B(A_M) &\approx -\frac{\log(C \cdot \epsilon_0^{-D_B(A_M)}) - \log(C \cdot \epsilon_1^{-D_B(A_M)})}{\log(\epsilon_0) - \log(\epsilon_1)} \\ &\approx -\frac{\log(\tilde{N}(A_M; \epsilon_0)) - \log(\tilde{N}(A_M; \epsilon_1))}{\log(\epsilon_0) - \log(\epsilon_1)}. \end{aligned}$$

We can extend this method by determining $\tilde{N}(A_M; \epsilon_k)$ corresponding to a series of values $\epsilon_0 > \epsilon_1 > \dots > \epsilon_m$. We can now generate a logarithmic plot of ϵ_k and $\tilde{N}(A_M; \epsilon_k)$. Since we have that $\log(\tilde{N}(A_M; \epsilon_1)) \approx \log(C \cdot \epsilon^{-D_f(A)})$ we must have that for ϵ 'small enough' we will get a linear function through the data points. Of course in reality this doesn't happen, hence we shall fit a linear function through the data points, using for example the least squares method. The tangent of this linear function will then determine the boxcounting dimension.

Example: Numerical approximation boxcounting dimension of Hénon attractor

When reconsidering the magnification of part of the Hénon attractor as displayed figure 2.16, one observes that we can investigate the parabolae segments in ‘directions’ which make up the structure of the Hénon attractor: the ‘Cantor’ direction and the curve direction; as is shown in figure 2.18.

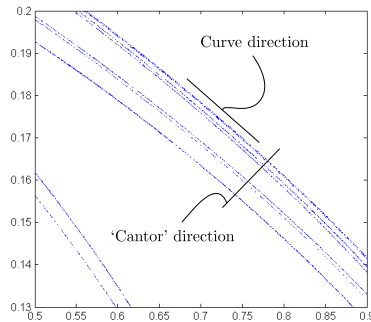


Figure 2.18: We can investigate the curves in the Hénon attractor in two direction: The ‘Cantor’ direction and the curve direction.

In the Cantor direction we observe a Cantor like structure which will correspond to a dimension smaller than one, in the curve direction we expect a dimension of one. Hence it seems plausible that the dimension of the Hénon attractor must equal one plus a fractional amount, thus the Hénon attractor is a fractal.

The Cantor like structure is a consequence of the folding in the Hénon attractor and determines the local and global structure. Hence we expect that the local dimension, the dimension of a magnification of a segment of the Hénon attractor, will be equal to the global dimension of the Hénon attractor. To verify this numerically we generate a log plot $N(\mathcal{H}; \epsilon)$ versus ϵ , see figure 2.19.

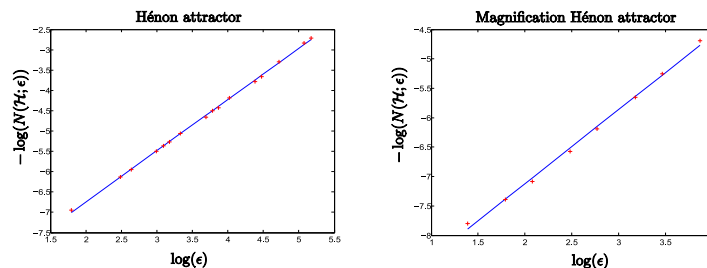


Figure 2.19: The numerical log plots of $N(\mathcal{H}; \epsilon)$ versus ϵ for the Hénon attractor and a magnification of the Hénon attractor. The approximation of the boxcounting dimension is given by the tangent of the lines. The Hénon attractor has boxcounting dimension 1.27 and the magnification has boxcounting dimension 1.26.

The approximation of the boxcounting dimension is given by the tangent of the linear functions in the figure above. The approximated boxcounting dimension of the Hénon attractor yields 1.27 and the boxcounting dimension of the magnification yields 1.26. As expected we have a dimension of one plus a fractional amount. Furthermore we conclude that the local dimension is almost equal to the global dimension.

Remark: The actual boxcounting dimension of the Hénon attractor is given by 1.28 [23]. Our calculated dimension in figure 2.16 differs slightly from the dimension calculated in the literature. This is due to the fact that we have made the algorithm very time efficient, but in doing so some of the precision is lost.

The dimension of the magnification of the Hénon attractor in figure 2.16 is a bit too low. This is due to fact that we need to calculate the Hénon attractor by iterating an initial state for more iterations, this will make the lines almost connected in the magnification and hence increase the dimension.

Numerically determining the dimension with boxcounting has some practical problems, since the used cover might actually not be the minimum cover. This would mean that the estimate of $N(A; \epsilon)$ can be too high. For example take the two different covers for the object in figure 2.20.

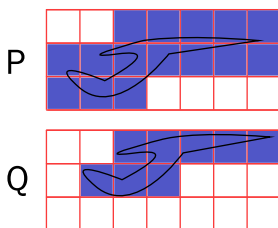


Figure 2.20: Two different covers of squares for the same object: The cover P has 16 squares and the cover Q has only 8 squares.

In the worst case scenario, P , we cover the object by 16 squares, while the minimum cover, Q , has a cover of only 8 squares. As we decrease ϵ still something of this problem remains. This problem arises from the fact that it is not checked how well the cover of squares are filled.

Correlation dimension

We can take a probabilistic view on the numerical problems that arise from the boxcounting dimension. The boxcounting dimension doesn't check what the odds are that a point x is in a n -dimensional cube. The correlation dimension does take this into account. The correlation dimension uses the probability of finding two independently chosen points in a single cube to calculate the dimension, in doing so it takes the fill of a cube into account. For we have that the higher the probability that a point x can be found in a cube, the 'denser' the cube is filled.

Definition 2.3.2 (Correlation dimension) Let $A \subset \mathbb{R}^n$. Cover A by n -dimensional balls, Q_i , with radius $\epsilon > 0$ and $1 \leq i \leq K$. The probability to find a point $x \in A$ in a Q_i shall be denoted by p_i . Define the minimum sum of all these probabilities by

$$P(\epsilon; X) = \inf_{Q_i} \sum_{i=1}^K p_i^2.$$

The correlation dimension is then given by

$$D_C(X) = \lim_{\epsilon \rightarrow 0} \frac{\log(P(A; \epsilon))}{\log \epsilon}$$

only for the cases that this limit exists.

Similarly to the boxcounting dimension we can define a version of the correlation dimension where Q_i will corresponds to cubes instead of balls. An important property of the correlation dimension is

$$D_C(A) \leq D_f(A). \quad (2.5)$$

We will skip the proof and refer to [33]. We also have that in most cases the correlation dimension gives a better approximation of the fractal dimension than the approximation of the boxcounting dimension. The approximation of the fractal dimension by correlation dimension is allowed since in a lot of cases equality holds in statement 2.5 [10], however this is not always the case. For example the approximated correlation dimension of the Hénon attractor is equal to 1.21 while the approximated boxcounting dimension is equal to 1.28 [10].

Remark: There are various definitions of dimension. For a more extensive description of other dimension definitions we refer to [5, 23].

2.3.2 Sensitivity

A sensitive system has the property that two points which start near to each will separate as time progresses. More formally we have the following definition.

Definition 2.3.3 (Sensitivity discrete time set) *Let (M, d) be a metric space, then a map $\Phi^1 = f : M \rightarrow M$ with the restriction $f|_U$ has sensitive dependence on initial values if and only if there exists a constant $\delta > 0$ such that the following holds: for any initial value $x_0 \in U$ and any (small) $\epsilon > 0$, there exists an initial value $y_0 \in U$ with $d(y_0, x_0) < \epsilon$ and there exists an $n \geq 0$ such that $d(f^n(y_0), f^n(x_0)) > \delta$.*

Definition 2.3.4 (Chaotic, ‘Devaney’) *An attractor Λ generated by the map f is called chaotic if and only if the restriction $f|_\Lambda$ has sensitive dependence on initial values.*

Remarks:

- Definition 2.3.4 resembles closely the definition of chaotic from Devaney. However it is not completely the same since Devaney has an alternative definition of attractor [13].
- There also exists alternative definitions of chaotic we refer to [8] and [27].

At the beginning we have already taken a quick look at the sensitivity of the Hénon map, recall figure 2.4. Although there is good numerical evidence that the Hénon attractor is chaotic this is an open conjecture. However it is proven that for certain parameter values chaotic Hénon-like attractor take place [6].

As a short intermezzo, let us take a look at a system for which we can prove sensitivity.

Baker transformation

The Baker transformation or ‘period doubling map’ is given by the evolution operator

$$\Phi^1 = B : x \longmapsto 2x \bmod 1.$$

The state space is given by $M = [0, 1)$.

Using the kneading paradigm we can view the Baker transform as the stretching of dough by a factor two and then cutting of the piece that exceeds $[0, 1)$. We then repeat the process for the cut off piece, as is made clear in figure 2.21, where we set $B(x_n) = x_{n+1}$.

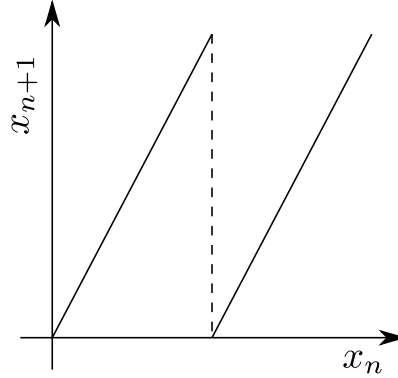


Figure 2.21: The Baker transformation visualized by the graph of x_{n+1} with respect to x_n .

Let us consider rewriting the state space in terms of a binary expansion. Then we can write a state $x_0 = 0.a_1a_2\dots$ with $a_i \in \{0, 1\}$. Writing down the n -orbit of x_0 for the Baker transformation yields

$$\begin{aligned} x_0 &= 0.a_1a_2a_3\dots, \\ x_1 &= 0.a_2a_3a_4\dots, \\ x_2 &= 0.a_3a_4a_5\dots, \\ &\vdots \\ x_n &= 0.a_{n+1}a_{n+2}a_{n+3}\dots \end{aligned}$$

An iterate x_n shifts the first n iterates ‘away’, hence this operation is called a shift. Geometrically this will mean that if we have that x_n with $a_{n+1} = 0$ the n th iterate will be contained in the left interval $[0, 1/2)$, I_0 , and if $a_{n+1} = 1$ the iterate will be contained in the right interval $[1/2, 1)$, I_1 . Thus for a finite binary expansion the positions of the orbit $\{x_0, x_1, \dots\}$ with respect to I_0 and I_1 will determine the binary expansion of the initial state x_0 .

By making use of a binary representation of the states we can prove sensitive dependence on initial values for the Baker transformation.

Proposition 2.3.1 *The Baker transformation has sensitive dependence on initial values.*

Proof. Take the metric space $\{M, d\}$ with $M = [0, 1)$ and $d(x, y) = |x - y|$ with $x, y \in M$. For an initial value $x_0 = 0.a_1a_2\dots$ with $a_i \in \{0, 1\}$ we have that

$$\Phi^1 : 0.a_1a_2a_3\dots \mapsto 0.a_2a_3\dots$$

There exists a $y_0 = 0.b_1b_2b_3\dots$ with $b_i \in \{0, 1\}$ such that $|y_0 - x_0| < \epsilon$. Then take a k such that $a_k \neq b_k$. We can assume without doing any harm that $a_k = 0$ and $b_k = 1$, thus we obtain four possibilities:

- (a) $\Phi^{k-1}(y_0) = 0.01\dots \in (1/4, 1/2]$, $\Phi^{k-1}(x_0) = 0.10\dots \in [1/2, 3/4)$
- (b) $\Phi^{k-1}(y_0) = 0.01\dots \in (1/4, 1/2]$, $\Phi^{k-1}(x_0) = 0.11\dots \in [3/4, 1)$
- (c) $\Phi^{k-1}(y_0) = 0.00\dots \in [0, 1/4)$, $\Phi^{k-1}(x_0) = 0.10\dots \in [1/2, 3/4)$
- (d) $\Phi^{k-1}(y_0) = 0.00\dots \in [0, 1/4)$, $\Phi^{k-1}(x_0) = 0.11\dots \in [3/4, 1)$

In case (b)(c)(d) we have $|\Phi^{k-1}(y_0) - \Phi^{k-1}(x_0)| > 1/4$. If we have case (a) then iterate again until it is equivalent to one of the cases (b)(c)(d) (by interchanging x_0 and y_0 if necessary), if this is not the case we will have an infinite binary expansion with $\Phi^{k-1}(y_0) = 0.01010101010\dots \in (1/4, 1/2]$, $\Phi^{k-1}(x_0) = 0.1010101010\dots \in [3/4, 1)$, by solving the infinite sums we obtain that $|\Phi^{k-1}(y_0) - \Phi^{k-1}(x_0)| > 1/4$. \square

For a more extensive treatment of the Baker transformation we refer to [1].

Measuring sensitivity: Lyapunov exponent and Lyapunov number

We now restrict ourselves to dynamical systems with a discrete time set. For simplicity we define $\Phi^1(x) = f(x)$. We extend the definitions to a continuous time set in section 4.2.3.

To measure the sensitivity of a dynamical system we need to quantify the error propagation, i.e the magnification per iterate of the distance between the points $f^n(x)$ and $f^n(y)$ with y chosen in a neighbourhood of x . First consider the one-dimensional map $f : \mathbb{R} \rightarrow \mathbb{R}$.

Take x_0 an initial state and y_0 the perturbed x_0 . We define the error after k iterations by $E_k = x_k - y_k$. Take a n -periodic orbit and observe that we can rewrite the relative error growth (E_n/E_0) of the orbit as

$$\frac{E_n}{E_0} = \frac{E_n}{E_{n-1}} \cdot \frac{E_{n-1}}{E_{n-2}} \cdot \dots \cdot \frac{E_1}{E_0}.$$

By doing this we are averaging the relative growth, this will lead to a better approximation. Furthermore we can rewrite the relative error per iteration as

$$\frac{E_k}{E_{k-1}} = \frac{f(x_k + E_{k-1}) - f(x_k)}{E_{k-1}} \Rightarrow \lim_{E_0 \rightarrow 0} \frac{E_k}{E_{k-1}} = f'(x_k).$$

Decreasing the initial error to zero yields an approximation of the relative error growth:

$$\lim_{E_0 \rightarrow 0} \frac{E_n}{E_0} \approx f'(x_n) \cdot f'(x_{n-1}) \cdot \dots \cdot f'(x_0).$$

The above equation is a cumulative amount of relative errors. Since the approximation uses n -iterations to get a relative error of E_n/E_0 , the relative average error per iteration will be given by $(E_n/E_0)^{\frac{1}{n}}$. Since we are also dealing with non-periodic orbits we have that $n \rightarrow \infty$. Now we can quantify the average error propagation as follows for the one-dimensional case.

Definition 2.3.5 (Lyapunov number and exponent for the one-dimensional case) Let $f : \mathbb{R} \rightarrow \mathbb{R}$ be a smooth map.

1. The Lyapunov number $\ell(x_0)$ of an orbit of $\{x_0, x_1, \dots\}$ is defined as

$$\ell(x_0) = \lim_{n \rightarrow \infty} (|f'(x_{n-1}) \cdot f'(x_{n-2}) \cdot \dots \cdot f'(x_0)|)^{\frac{1}{n}}$$

if this limit exists.

2. The Lyapunov exponent is defined $h(x_0)$ as

$$h(x_0) = \lim_{n \rightarrow \infty} \frac{1}{n} (\log |f'(x_{n-1})| + \log |f'(x_{n-2})| + \dots + \log |f'(x_0)|)$$

if this limit exists.

Lyapunov exponents are nothing else than $\log(\ell(x_0))$, however we have chosen to use Lyapunov numbers and exponents and not just Lyapunov numbers (or exponents), since depending on the circumstances it is easier to use Lyapunov numbers (or exponents). It follows that if a statement applies for Lyapunov numbers, exponents this can be extended to Lyapunov exponents, numbers, respectively.

Remarks:

- Lyapunov numbers and exponents do not have to exist for every orbit. This is the case when there exists an x_i in an orbit such that $f'(x_i) = 0$.
- If x_0 is a k -periodic point, then it follows that the Lyapunov number is given by $\ell(x_0) = (|f'(x_{k-1}) \cdot \dots \cdot f'(x_0)|)^{\frac{1}{k}}$.

Lyapunov numbers represent the relative average error per iteration. We want to use Lyapunov numbers to define a chaotic orbit. If a Lyapunov number is greater than one, the orbits of initial values which start near each other will separate, i.e. the orbit shows sensitivity. Sensitivity must be a property of a chaotic orbit, but we will also need that a chaotic orbit won't show any sign of predictable behaviour. Hence we come to the definition of asymptotically periodic.

Definition 2.3.6 (Asymptotically periodic) *An orbit $\{x_0, x_1, \dots, x_n, \dots\}$ is called asymptotically periodic if it converges to a periodic orbit as $n \rightarrow \infty$ i.e. there exists a periodic k -orbit $\{y_0, y_1, \dots, y_k\}$ such that*

$$\lim_{n \rightarrow \infty} |x_n - y_n| = 0.$$

A chaotic orbit for the one-dimensional case is defined as follows.

Definition 2.3.7 (Chaotic orbit, one-dimensional case) *Let $f : \mathbb{R} \rightarrow \mathbb{R}$ and let $\{x_0, x_1, \dots\}$ be a bounded orbit of f . This orbit is called chaotic if and only if*

1. *the orbit $\{x_0, x_1, \dots\}$ is not-asymptotically periodic.*
2. *the Lyapunov number $\ell(x_0)$ is greater than one.*

Example: Baker transformation continued

Let us show that by the above definition the Baker transformation is chaotic. Let us first find a not asymptotically periodic orbit, consider the initial state in binary expansion given by

$$x_0 = 0.0100011011000001\dots$$

which consists out of all the possible binary expansions. It follows that the corresponding orbit is not asymptotically periodic.

One has that $\Phi^{1'}(x) = 2$. For the Lyapunov number one obtains

$$\ell(x_0) = \lim_{n \rightarrow \infty} (|\Phi^{1'}(x_{n-1}) \cdot \Phi^{1'}(x_{n-1}) \cdot \dots \cdot \Phi^{1'}(x_0)|)^{\frac{1}{n}} = 2 > 0.$$

Hence the Baker transformation has a chaotic orbit.

The Hénon map is not on \mathbb{R} but on \mathbb{R}^2 and at the end of this thesis we would also like to know the Lyapunov numbers for systems on \mathbb{R}^3 . So we desire to expand definition 2.3.5 to a map $f : \mathbb{R}^m \rightarrow \mathbb{R}^m$. Instead of defining a single number we measure the propagation of the relative error along m orthogonal directions, r_1, \dots, r_m . The first value will be the direction in which the separation is the greatest (or least contracting), and shall be called r_1 . The second value will be the greatest separation chosen from all directions perpendicular to the first and shall be called r_2 . The third will then be the greatest value such that it is perpendicular to the first and second etc. One can find these Lyapunov numbers and exponents of an orbit x_0 in the following way first take a m -dimensional unit sphere around x_0 and iterate it n -times with the map f . It will then be elongated such that the sphere is mapped onto an ellipsoid. The change per iterate of the axis of this ellipsoid will then correspond to the Lyapunov number. In figure 2.22 we have represented the process for a map $f : \mathbb{R}^2 \rightarrow \mathbb{R}^2$.

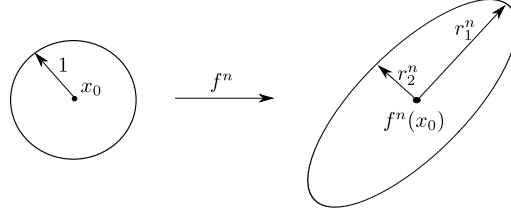


Figure 2.22: The mapping of a unit circle centred at x_0 under $f^n(x_0)$ onto the ellipsoid. The axis of greatest separation is given by r_1^n . r_2^n corresponds to the axis (of greatest separation) perpendicular to the axis of r_1^n .

One also observes an interesting property of the Lyapunov numbers from figure 2.22: the area contraction (or expansion) per iterate is given by $r_1^n \cdot r_2^n$ and thus the average area contraction (or expansion) is given by $r_1 \cdot r_2$. Extending this observation to the m -dimensional case, we have that the average area contraction (or expansion) is the product of r_1, \dots, r_m in absolute sense.

We are more interested in the infinitesimal behaviour around the orbit of x_0 . Hence the formal definition of Lyapunov numbers would be given by replacing f by the first derivative around this point, $Df(x_0)$, and x_0 by the origin. Setting $J_n = Df^n(x_0)$, it follows that these m -orthogonal axes, r_1^n, \dots, r_m^n , are the positive square roots corresponding to the eigenvalues of $J_n J_n^T$. From these statements the definition for the m -dimensional case follows.

Definition 2.3.8 (Lyapunov number and exponent for m -dimensional case) *Let f be a smooth map on \mathbb{R}^m and $J_n = Df^n(x_0)$. Define r_k^n with $k = 1, 2, \dots, m$ to be the length of the k th longest orthogonal axis of the ellipsoid $\{Df^n(x_0)(\hat{x}) \mid \hat{x} \in \mathbb{S}^m\}$.*

1. The k th Lyapunov number is then given by

$$\ell_k(x_0) = \lim_{n \rightarrow \infty} (r_k^n)^{\frac{1}{n}}.$$

for the cases that the limit exists.

2. The k th Lyapunov exponent is then given by

$$h_k(x_0) = \log \ell_k(x_0)$$

for the cases that the limit exists.

Proposition 2.3.2 (Area contraction or expansion) *Let f be a smooth map on \mathbb{R}^m with Lyapunov numbers $\{\ell_1, \dots, \ell_m\}$, then the average area contraction or expansion is given by*

$$A = |\ell_1| \cdot \dots \cdot |\ell_m|.$$

The proof follows directly from definition 2.3.8.

Having defined Lyapunov exponents and numbers for the general case we now immediately come to the definition of chaotic orbits for the m -dimensional case.

Definition 2.3.9 (Chaotic orbit, m -dimensional case) *Let $f : \mathbb{R}^m \rightarrow \mathbb{R}^m$ and let $\{x_0, x_1, \dots\}$ be a bounded orbit of f . This orbit is called chaotic if*

1. the orbit $\{x_0, x_1, \dots\}$ is not asymptotically periodic.
2. $\ell_1(x_0) > 1$.

Remarks:

- Yorke adds another condition to definition 2.3.9: no Lyapunov number is exactly one. If this definition is used it excludes all cases which show ‘quasiperiodicity’. For example consider the map

$$f(r, \theta) = (r^2, \theta + 2\pi q)$$

with q an irrational number and (r, θ) polar coordinates. The points inside the unit circle will converge to the origin. The points outside the unit circle are unbounded. The points on the unit circle ($r = 1$) rotate an angle $2\pi q$, furthermore the unit circle is invariant under f . The points on $r = 1$ have Lyapunov numbers equal to 2 and 1. By choice of q the orbits are not asymptotically periodic and since one Lyapunov number is greater than one, they will show sensitive dependence. The motion of these orbits is quite predictable, hence one could substantiate that this is not unpredictable enough for a chaotic orbit. This predictability will in most cases lead to an invariant shape which is not a fractal.

- Condition 2 in definition 2.3.9 is equivalent to $h_1(x_0) > 0$.

Numerical calculation of Lyapunov numbers and exponents

For a lot of interesting maps there is no direct method to determine Lyapunov numbers and exponents, hence we are forced to use numerical algorithms. One-dimensional maps such as the Baker transformation are an exception to this rule.

Assume that we have at least one Lyapunov number greater than one and at least one Lyapunov number smaller than one. The Lyapunov numbers are given by the $2n$ roots of the eigenvalues of $J_n J_n^T$; let us call these eigenvalues λ_i . By the assumption we have that there exists one λ_i greater than one, call this λ_1 , and one smaller than one λ_m . As we increase the n in $J_n J_n^T$, the difference between λ_1 and λ_m will increase. This will lead to bad approximations due to numerical error.

An indirect approach works better. We make use of a method based on Gram-Schmidt orthonormalization which will generate all Lyapunov numbers and exponents simultaneously. We have given a quick overview how this works in Appendix C; for a more detailed overview of this method we refer to [11].

Categorizing dynamical systems by Lyapunov numbers

Let us first look at a fixed point, x_0 , of $f : \mathbb{R}^m \rightarrow \mathbb{R}^m$. Let us call the eigenvalues of $Df(x_0)$ $\lambda_1, \dots, \lambda_m$; these eigenvalues give a description of the stability around the fixed point. The Lyapunov numbers for the fixed point will then be given by $|\lambda_1|, \dots, |\lambda_m|$ since we are dealing with a fixed point. Hence the Lyapunov numbers corresponds to the magnitude of the eigenvalues. We obtain now a correspondence between Lyapunov numbers and eigenvalues. For example when all the eigenvalues are in absolute value smaller than one, we are dealing with an asymptotically stable fixed point. An asymptotically stable fixed point implies that solutions are attracted and indeed the interpretation of Lyapunov numbers tells us that contraction takes place. A similar argument can be given for unstable fixed points.

We can extend these results to a k -periodic orbit. Thus for $f : \mathbb{R}^m \rightarrow \mathbb{R}^m$ with a k -periodic orbit x with Lyapunov numbers $\{\ell_1, \dots, \ell_m\}$, we have that

- for $\ell_i < 1$ with $i = 1, \dots, m$ corresponds to an asymptotically stable orbit.
- for $\ell_i > 1$ with $i = 1, \dots, m$ corresponds to an unstable orbit.

We also have the case when one or more Lyapunov numbers are equal to one. For the case when one of the Lyapunov numbers is equal to one and the others less than one, the orbit will correspond to a limit cycle, since a Lyapunov number equal to one implies that in one direction no contraction or

expansion takes place. For a more extensive treatment on the cases where more than one Lyapunov number is equal to one we refer to [11].

We are left with the case $\ell_i \leq 1$ with $i = 1, \dots, k$ and $\ell_i > 1$ $i = k + 1, \dots, m$. The average area contraction is given by multiplying all Lyapunov numbers. A chaotic orbit must be bounded hence

$$|\ell_1| \cdot \dots \cdot |\ell_m| < 1. \quad (2.6)$$

This is directly related to the area contracting property of (chaotic) attractors.

Thus for non-periodic orbits which satisfy 2.6 and have one Lyapunov number greater than zero we have a chaotic orbit corresponding to a chaotic attractor.

Note that when we have two fixed saddle points with area contracting this doesn't have to mean that we are dealing with a chaotic attractor, and indeed with Lyapunov exponents we can verify this, as the following example will illustrate.

Example: attracting orbit for a Lozi map with two fixed saddle points

Take the Lozi map with parameters $a = 1.3$ and $b = 0.8$. The fixed points are given by

$$p_1 = \left(\frac{1}{1.5}, \frac{0.8}{1.5} \right), \quad p_2 = \left(-\frac{1}{1.1}, -\frac{0.8}{1.1} \right).$$

By straightforward computation one concludes that these are fixed saddle points. Numerically computing the orbit of $(-1, 1.1)$ yields figure 2.23.

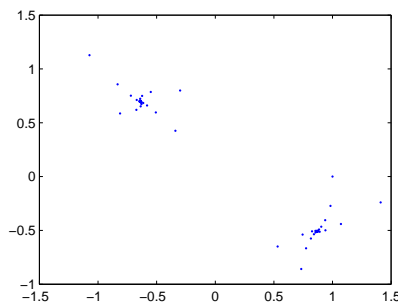


Figure 2.23: The Lozi mapping for the parameters $a = 1.3$ and $b = 0.8$ and initial value $(-1, 1.1)$.

Indeed fixed points don't tell everything about a system, for one observes that the orbit converges to a period-two orbit, which doesn't show any sign of a chaotic attractor. We also verify this by numerically computing the Lyapunov numbers:

$$\ell_1 = 0.896, \quad \ell_2 = 0.893.$$

Remark: One must note here that we are looking at Lyapunov numbers and exponents of a single orbit. When we are dealing with a chaotic attractor, we assume that a single orbit is representative for the complete attractor. In other words we assume that the orbit gets arbitrarily close to any point on the chaotic attractor.

2.3.3 Lyapunov dimension

The boxcounting and correlation dimension require a lot of numerical power, especially if we move to higher dimensions. There is a relation between the Lyapunov exponent and the boxcounting dimension of an attractor. It is based on numerical experiments done by L. Kaplan and J. A. Yorke around 1978 [23]. Although an actual proof has not been given, except for some special cases, it gives a good approximation of the boxcounting dimension. The dimension definition that acknowledges this relation is called the Lyapunov dimension.

Definition 2.3.10 (Lyapunov dimension) Let $f : \mathbb{R}^m \rightarrow \mathbb{R}^m$. Consider an orbit corresponding to an initial value x_0 with Lyapunov exponents $h_m \leq \dots \leq h_1$, now let p denote the largest integer such that

$$\sum_{i=1}^p h_i \geq 0.$$

Define the Lyapunov dimension D_ℓ of x_0 by

$$D_\ell = \begin{cases} 0 & \text{if no such } p \text{ exists} \\ p + \frac{1}{|h_{p+1}|} \sum_{i=1}^p h_i & \text{if } p < m \\ m & \text{if } p = m \end{cases}$$

Lyapunov dimension approximates the fractal dimension

Let us give a short heuristic argument why the Lyapunov dimension gives a good approximation of the fractal dimension. We will only treat the case for \mathbb{R}^2 , but a similar argument can be given for \mathbb{R}^3 or higher dimensions [1].

Take a small square with length s . Apply the transformation f to this with corresponding Lyapunov exponents h_1, h_2 , as is done in figure 2.24.

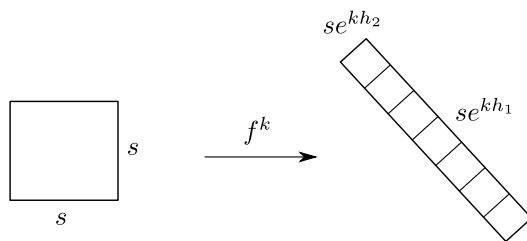


Figure 2.24: The transformation f^k applied to a square with sides of length s . As one observes it will be elongated in one direction by a factor corresponding to the greatest Lyapunov exponent given by $e^{k h_2}$. In the other direction it will be contracted by a factor given by $e^{k h_1}$.

We first assume that $h_2 \leq 0 \leq h_1$ and $h_1 + h_2 < 0$, or in other words: in one direction we stretch, which is represented by h_1 , and in the other we shrink, h_2 . So the transformed square will turn into a rectangle with sides $s e^{h_1}$ and $s e^{h_2}$. After k iterations the square will have sides $s e^{k h_1}$ and $s e^{k h_2}$. The area is given by $s^2 e^{k(h_1 + h_2)}$, as indicated in figure 2.24, which for increasing k will converge to 0. Furthermore the length in one direction will keep on increasing and in the other direction will keep decreasing. It will become a line and assuming that the orbit is bounded it will fold back again. So we expect that the dimension is given by 1 plus a certain fractional amount.

Now let us subdivide the k -iterated rectangle with squares of length $\epsilon = se^{kh_2}$. The amount of squares needed to cover the rectangle is given by $e^{k(h_1)}/e^{kh_2}$. Now by using the definition of fractal dimension we get

$$\begin{aligned} \lim_{\epsilon \rightarrow 0} \frac{\log N(\epsilon)}{\log \epsilon} &\approx \lim_{k \rightarrow \infty} \frac{\log N(s)e^{k(h_1-h_2)}}{\log se^{kh_2}} = \lim_{k \rightarrow \infty} \frac{\log(N(s)) + k(h_1 - h_2)}{\log(s) + kh_2} \\ &= \frac{k(h_1 - h_2)}{kh_2} = 1 - \frac{h_1}{h_2} = 1 + \frac{h_1}{|h_2|}. \end{aligned}$$

Thus we may conclude that this corresponds to definition 2.3.10 in \mathbb{R}^2 .

We are still left with two cases: $h_1 < 0, h_2 \leq 0$, for which the Lyapunov dimension is zero, and $h_1 + h_2 \geq 0$, for which the Lyapunov dimension is two. In the first case we have a map which contracts in two directions, under iterating this will lead to a single point which has boxcounting dimension zero. The second case follows from the fact that if two Lyapunov exponents are greater than zero, then under iterations the set expands until it covers complete \mathbb{R}^2 , thus it has boxcounting dimension two.

2.3.4 Lyapunov bifurcation diagrams for the Hénon mapping and Lozi mapping

We shall now present Lyapunov bifurcation diagrams which give a description of the Hénon mapping and Lozi mapping in the parameter plane. However we will first look at two specific cases: the Hénon and Lozi attractor.

For all these cases we calculate the Lyapunov exponents for a single orbit, the orbit corresponding to $(0, 0)$.

Lyapunov exponents and dimensions for the Hénon and Lozi attractor

The Lyapunov numbers and dimension for the Hénon attractor ($a = 1.4$ and $b = 0.3$) yield

$$\ell_1 = 1.517, \quad \ell_2 = 0.1978, \quad D_\ell = 1.257.$$

We would like to give an interpretation of these values. We have one expanding direction corresponding to ℓ_1 and one contracting direction corresponding to ℓ_2 . Since $\ell_1 + \ell_2 < 1$ and $\ell_1 > 1 > \ell_2$ we are dealing with a chaotic attractor. Furthermore we can check our numerical results by calculating the average area contraction. We know that the Hénon transform contracts area by a factor 0.3 per iterate (see proposition 2.1.1), thus $\ell_1 \cdot \ell_2 = 0.3$ as follows from proposition 2.3.2. The approximated values indeed yield

$$\ell_1 \cdot \ell_2 \approx 0.3.$$

The Lyapunov dimension 1.257 corresponds closely to the boxcounting dimension 1.28.

The Lyapunov numbers and dimension for the Lozi attractor ($a = 1.7$ and $b = 0.5$) yield

$$\ell_1 = 1.469, \quad \ell_2 = 0.3403, \quad D_\ell = 1.357.$$

Once again we have that $\ell_1 + \ell_2 < 1$ and $\ell_1 > 1 > \ell_2$ thus we are dealing with a chaotic attractor. We also have

$$\ell_1 \cdot \ell_2 \approx 0.5.$$

Observe that the Lyapunov dimension of the Lozi attractor is higher than the dimension of the Hénon attractor, this is a consequence of the contraction of the Lozi attractor ($b = 0.5$), which is less than the contraction of the Hénon attractor ($b = 0.3$).

Hénon mapping

We now investigate the stability of the orbits for the Hénon mapping in the parameter plane. The result including two magnifications is displayed in figure 2.25.

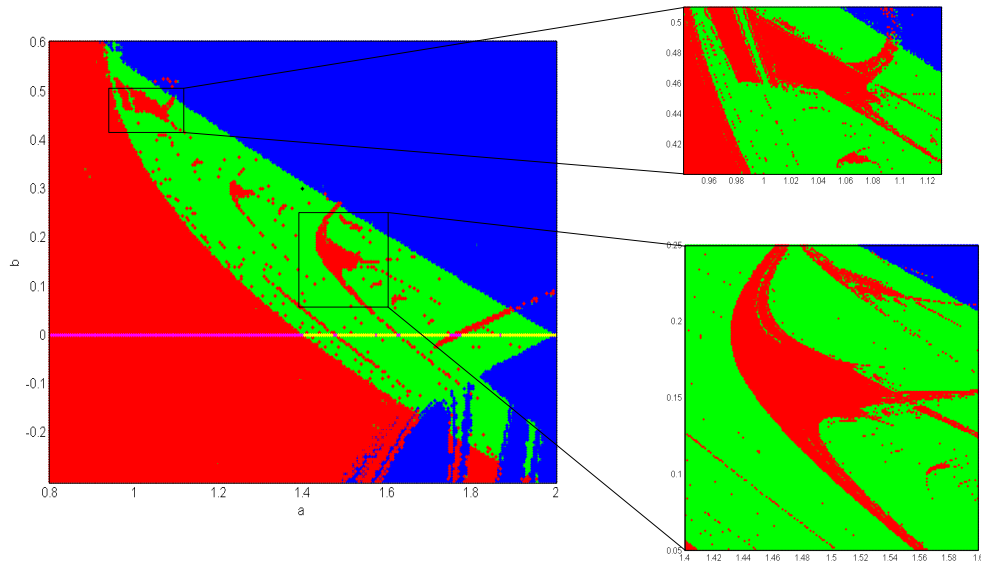


Figure 2.25: Stability of the Hénon map in the parameter plane by making use of Lyapunov exponents. With the black dot we have indicated the position of the Hénon attractor.

Lyapunov numbers	interpretation	colour
$\ell_1, \ell_2 < 1$	asymptotically stable equilibrium point(s)	red
$\ell_1 > 1, \ell_2 < 1$ with $ \ell_1 \cdot \ell_2 < 1$	chaotic attractor	green
$\ell_1, \ell_2 > 1$	unstable equilibrium point(s)	blue
$\ell_1 < 1, \ell_2 = 1$	asymptotically stable limit cycle (one dim.)	magenta
$\ell_1 > 1, \ell_2 = 1$	unstable limit cycle (one dim.)	yellow

Let us make some observations from figure 2.25.

- One observes immediately the complexity of the bifurcation diagram. This complexity is continued in the magnifications.
- The green area, which contains Hénon-like attractors, is several times intersected by the stable and the unstable plane, and also contains several holes (or islands) which correspond to the stable plane. One also has parameters corresponding to chaotic attractors surrounded by the stable plane. These don't correspond to numerical errors, as one can verify with figure 2.26.

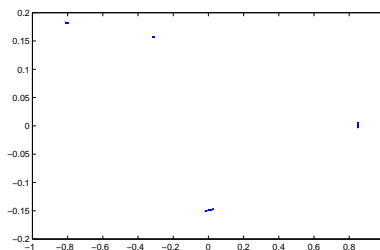


Figure 2.26: Hénon attractor for the parameter $a = 1.815$ and $b = 0.185$, which is completely surrounded in the parameter plane by the unstable plane.

We have not found the exact reason why this occurs. One might suggest that there exists a very small trapping region for the unstable plane, perhaps the orbit $(0, 0)$ ‘accidentally’ enters this region.

- A point of interest is the behaviour around the line $b = 0$, the Hénon map is then given by a single equation $(x_{n+1}, y_{n+1}) = (1 - ax_n^2, 0)$, hence the Hénon map reduces to an one-dimensional equation. The equation $x_{n+1} = 1 - ax_n^2$ is equivalent to the logistic mapping which we treated briefly in chapter 1. Recall that the logistic mapping is given by

$$q_{n+1} = \mu q_n(1 - q_n), \quad \mu \in (0, 4]$$

Taking $a = \mu(\mu - 2)/4$ in the one-dimensional Hénon map we obtain equivalence with the logistic mapping. The logistic mapping will begin to show sensitive dependence on initial values if $\mu \in [3.6, 4]$, see [23], thus we have that for $a \in [1.44, 2]$ the mapping $x_{n+1} = 1 - ax_n^2$ will begin to show sensitive dependence on initial values. These values correspond to figure 2.25, since the Lyapunov numbers are greater than one. We observe that this chaotic behaviour at the line $b = 0$ is continued in a neighbourhood of the chaotic segments, this numerically verifies the result of Benedicks and Carlson [6] which states that there exists a segment on the line $b = 0$ with an open neighbourhood in which chaotic behaviour of the logistic mapping is continued into the Hénon mapping.

- One also observes that the asymptotically stable lines which intersect $b = 0$ for $a \in [1.44, 1.7]$ seem to be parallel to each other in a neighbourhood of $b = 0$. This statement might perhaps be useful for future proofs on chaotic attractors for the Hénon map.

Let us now investigate the Lyapunov dimensions in the parameter plane of the Hénon map.

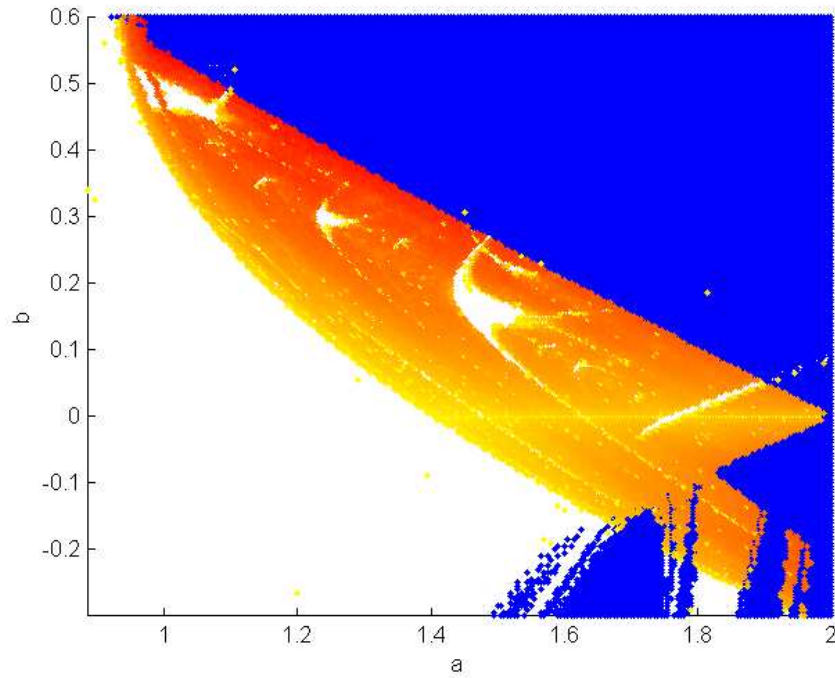


Figure 2.27: Lyapunov dimensions of the Hénon map in the parameter plane.

Lyapunov dimensions	interpretation	colour
$D_\ell = 0$	set of points	white
$D_\ell = 1$	a curve	yellow
$1 < D_\ell < 1.32$	fractal	yellow to red ¹
$D_\ell = 2$	covers complete \mathbb{R}^2	blue

¹The higher the dimension the more red.

Let us make some observations from figure 2.27.

- Taking b constant and increasing a in the chaotic plane we observe that the Lyapunov dimension increases, although it is a few times interrupted by the asymptotically stable plane. The parameter a corresponds to the folding in the Hénon map. As a is increased parabolae segments which appear on magnifications in the Hénon map will fold closer to each other leading to a higher Lyapunov dimension, see figure 2.28.

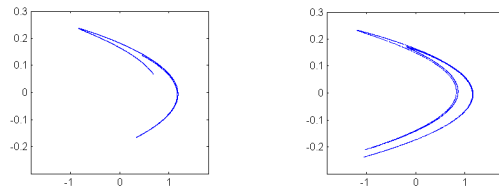


Figure 2.28: Left: Hénon-like attractor for the parameters $a = 1.3$ and $b = 0.2$. Right: Hénon-like attractor for the parameters $a = 1.6$ and $b = 0.2$. Observe that for $a = 1.6$ the attractor is more ‘tightly’ folded and hence has a higher Lyapunov dimension.

- Taking a constant and decreasing $|b|$ in the chaotic plane we observe that the Lyapunov dimension decreases, although it is a few times interrupted by the asymptotically stable plane. The parameter b corresponds to the contraction in y -direction of the Hénon map. Decreasing $|b|$ leads to an increase in contraction in the y -direction and consequently the attractor will begin to resemble a line, leading to a lower a Lyapunov dimension, see figure 2.29.

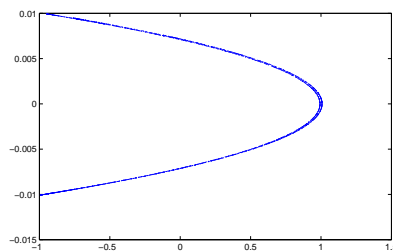


Figure 2.29: $\mathcal{H}_{1.965, -0.01}$: observe the strong contraction which takes place.

Lozi mapping

We now investigate the stability of the orbits for the Hénon mapping in the parameter plane. The result is displayed in figure 2.30.

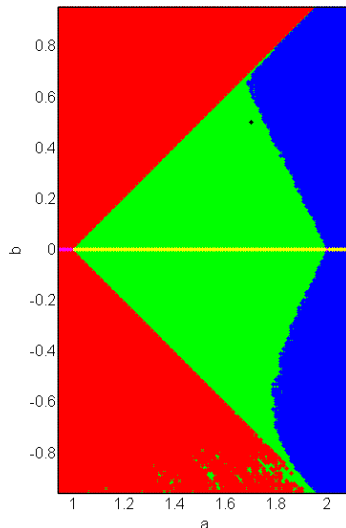


Figure 2.30: Stability of the Lozi map in the parameter plane by making use of Lyapunov exponents, with the black dot we have indicated the position of the Lozi attractor.

Lyapunov numbers	interpretation	colour
$\ell_1, \ell_2 < 1$	asymptotically stable equilibrium point(s)	red
$\ell_1 > 1, \ell_2 < 1$ with $ \ell_1 \cdot \ell_2 < 1$	chaotic attractor	green
$\ell_1, \ell_2 > 1$	unstable equilibrium point(s)	blue
$\ell_1 < 1, \ell_2 = 1$	asymptotically stable limit cycle (one dim.)	magenta
$\ell_1 > 1, \ell_2 = 1$	unstable limit cycle (one dim.)	yellow

Let us make some observations from figure 2.30.

- Observe how the position of the Lozi attractor in the parameter plane is similar to the Hénon attractor in figure 2.25; they are both located close to the rim of the unstable parameter plane.
- One observes that there is almost a symmetry by reflection in the a -axis. However we have green bits corresponding to chaotic attractors at the bottom of the lower half of the parameter plane which are not symmetric under reflection in the a -axis. To check if our algorithm works correctly let us numerically verify this. Figure 2.31 corresponds to such a non-symmetric point corresponding to a chaotic attractor, we have taken parameters $a = 1.55$ and $b = -0.9$.

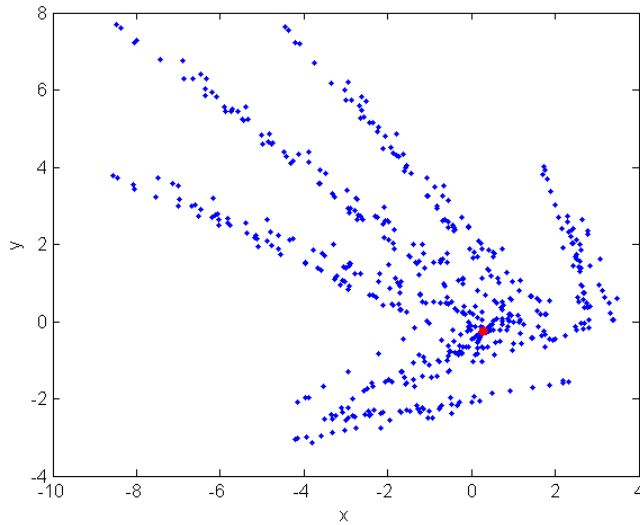


Figure 2.31: Orbit corresponding to the Lozi map for the parameters $a = 1.55$ and $b = -0.9$. These parameters correspond to the values for which the numerical algorithm tells that a chaotic attractor occurs. This numerical results yields that the orbit slowly converges to the red dot indicated in the figure.

The orbit in figure 2.31 converges very slowly to the red dot. So why does this occur? One can prove that these unsymmetrical green bits in the parameter plane have attracting fixed points with complex eigenvalues [3]. Complex attracting eigenvalues lead to spiralling solution curves which will converge much slower than those without spiralling, hence one would need significantly more iterations to see that the Lyapunov numbers become less than one.

We may now safely assume that the stability of the Lozi mapping is symmetric in the a -axis. Let us investigate if this symmetry also holds for the Lyapunov dimension.

- The symmetric behaviour by reflection in the a -axis is also continued into a small part in the parameter plane of the Hénon mapping; more specifically in chaotic plane with $a \in [1.97, 2]$. The a is big and the b is small meaning that the parabolae segments of the Hénon-like attractors get folded closely to each other such that they begin to resemble smoothed Lozi-like attractors; an example is given in figure 2.32.

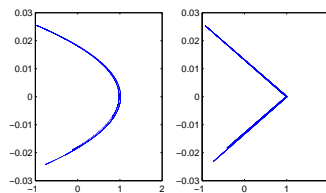


Figure 2.32: Left: $\mathcal{H}_{1.9,0,0.025}$. Right: $\mathcal{L}_{1.9,0,0.025}$. Observe how the Hénon-like attractor is similar to a smoothed Lozi-like attractor.

Why this behaviour isn't continued in the rest of the parameter plane of the Hénon map we will treat in further publication.

Lyapunov dimensions of the Lozi map in the parameter plane yields figure 2.33.

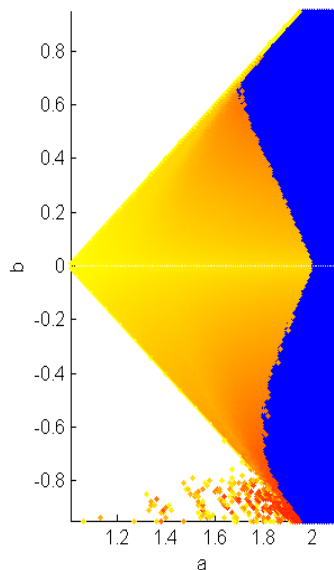


Figure 2.33: Lyapunov dimensions of the Lozi map in the parameter plane.

Lyapunov dimensions	interpretation	colour
$D_\ell = 0$	set of points	white
$D_\ell = 1$	a curve	yellow
$1 < D_\ell < 1.79$	fractal	yellow to red ²
$D_\ell = 2$	covers complete \mathbb{R}^2	blue

Let us make some observations from figure 2.33.

- Taking b constant and increasing a in the chaotic place we observe that the Lyapunov dimension increases as was also the case with the Hénon map in the parameter plane. The reason why this occurs is the same as with the Hénon mapping
- Taking a constant and decreasing $|b|$ in the chaotic place we observe that the Lyapunov dimension decreases as was also the case with the Hénon map in the parameter plane. The reason why this occurs is also the same as with the Hénon mapping.
- The symmetry under reflection in the a -axis still holds for the Lyapunov dimension up to a numerical error. We might now go as far as stating that there exists a conjugacy between the maps $L_{a,b}(x,y)$ and $L_{a,-b}(x,y)$. The problem is that we can prove that the behaviour of the fixed points is non-symmetric under reflection in the a -axis [3]. Thus we present the following conjecture.

Conjecture 2.3.1 (Symmetry in the parameter plane of the Lozi mapping) *There exists a conjugacy between $L_{a,b}(x,y)$ and $L_{a,-b}(\tilde{x},\tilde{y})$ where $x,y \in U$, $\tilde{x},\tilde{y} \in V$ where U,V are non-empty subsets of \mathbb{R}^2 .*

We will prove this conjecture in further publication.

²the higher the dimension the 'redder'

2.4 Multiple attractors with fractal basin boundaries

We have now only investigated the behaviour of a single attractor for the Hénon and Lozi map, it is possible that two attractors occur for a single Hénon or Lozi map. Take for example the map $H_{1.08,0.3}$. In figure 2.34 the orbits corresponding to $(0, 0)$ (in red) and $(0.5, 0.5)$ (in blue) are displayed.

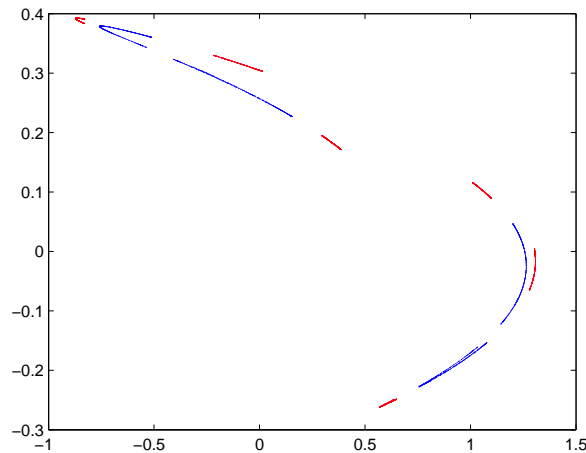


Figure 2.34: Two attractors for the map $H_{1.08,0.3}$: the attractors corresponding to the initial state $(0, 0)$ (red) and $(0.5, 0.5)$ (blue).

We can investigate this a bit more by slightly increasing the a and checking if we still have two attractors. The numerical results are presented in figure 2.35.

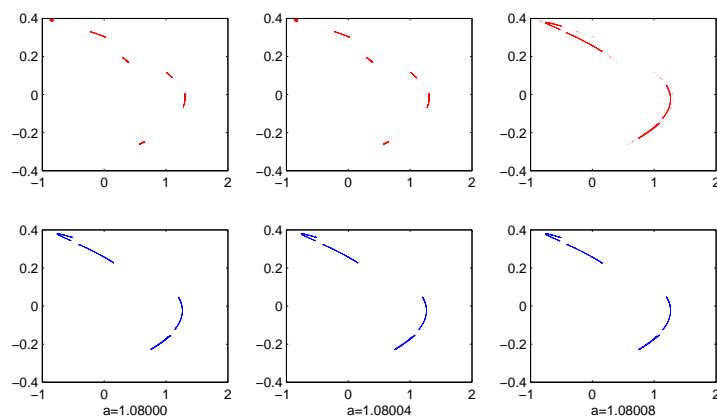


Figure 2.35: The behaviour of the attractors as we increase the parameter a . Observe that at $a = 1.08008$ the red attractor is lost since the blue and red attractor look almost equal.

We observe that the orbit corresponding to the red attractor begins to tend to the blue attractor if we slightly perturb a . To understand this phenomenon we numerically generate the basins of attraction, see figure 2.36.

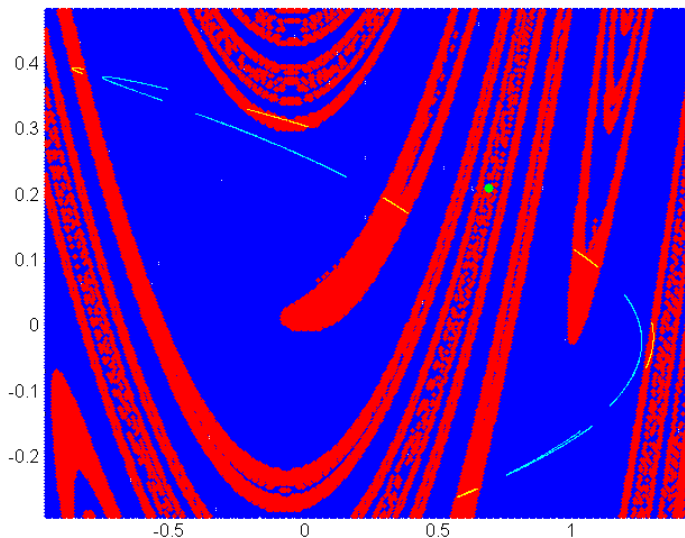


Figure 2.36: Basins of attraction for the attractors corresponding to $\mathcal{H}_{1.08,0.3}$. The yellow attractor corresponds to the orbit of $(0, 0)$ and has a red basin of attraction. The cyan attractor corresponds to the orbit of $(0.5, 0.5)$ and has a blue basin of attraction. Furthermore we have indicated the fixed saddle point with a green dot. Observe that this fixed point acts as a separator between the two basins of attraction.

One observes that the boundary of the basins of attraction, called basin boundary, gets more complicated in the region of the fixed saddle point. This fixed point acts as a separator between the two basins of attraction. For if we increase the parameter a , one of the attractors gets access to an area around the fixed point, which would mean that the fixed point is contained in two trapping regions; consequently the attractor corresponding to $(0.5, 0.5)$ disappears. This phenomenon is called interior crises at the boundary. For more on systems where crises occurs we refer to [20].

The complicated basin boundary in figure 2.36 will conserve complexity if magnified, hence we may assume that it is a fractal. We will see that fractal basin boundaries make systems unpredictable. This unpredictable behaviour occurs only near the basin boundary. For initial points that are not near the basin boundary we can safely predict to which attractor the orbit converges. However, as initial points get nearer to the basin boundary, it will get more and more difficult to predict to which attractor the orbit will converge, due to the fact that we can only specify the initial points up to a certain precision. This phenomenon is called uncertainty and plays an important role in the rest of this section

2.4.1 The uncertainty exponent

Take two basins of attraction A_1 and A_2 . An initial point, $x_0 \in A_1$ is called unsafe if there exists a $\tilde{x} \in B_s(x_0)$, where s is the machine-precision, with $\tilde{x} \in A_2$. Define $\mathcal{A}(s)$ the area or volume which is formed by the set of all unsafe initial points. Observe that the greater $\mathcal{A}(s)$ the more unsafe initial points there are and consequently the system behaves more uncertain.

First consider the case when the basin boundary of A_1 and A_2 is a non-fractal. Suppose we have a smooth curve as basin boundary, then $\mathcal{A}(s)$ is given by a strip of $2s$ around the curve, see figure 2.37. If we were to improve the precision by a factor 2, the amount of points in the unsafe region would decrease by a factor $1/2$.

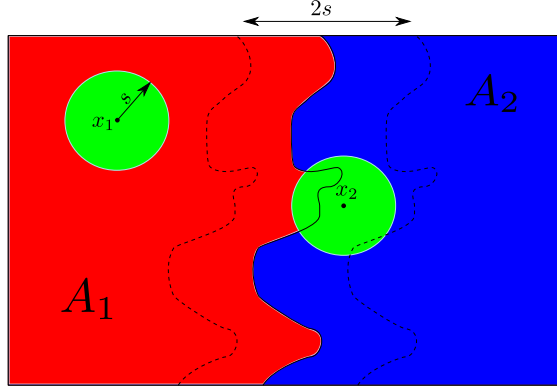


Figure 2.37: Curve as basin boundary. Here A_1 and A_2 are two basins of attraction. The area between the dotted lines, $\mathcal{A}(s)$, corresponds to the unsafe region hence the point x_1 is safe and the point x_2 is unsafe.

This scaling law is more complicated if we have a fractal as basin boundary. Recall the boxcounting dimension, definition 2.3.1; we can approximate $\mathcal{A}(s)$ for a fractal basin boundary F corresponding to basins of attraction, $A_i \subset \mathbb{R}^m$, by calculating $\tilde{N}(F; s)$ times the area or volume of the m -dimensional cubes. Using the approximation

$$\tilde{N}(F; \epsilon) \approx C \cdot \epsilon^{-D_B(F)},$$

we obtain that

$$\mathcal{A}(s) \approx \tilde{N}(F; s) \cdot s^d \propto s^{(m-D_B(F))}.$$

Formalizing the previous statements we define the uncertainty exponent.

Definition 2.4.1 (Uncertainty exponent) Take basins of attraction $A_i \subset \mathbb{R}^m$ and a basin boundary F , which can be determined up to a precision s . The uncertainty exponent of F is given by

$$\alpha := m - D_B(F).$$

A fractal basin boundary with a high dimension will have a small α which implies a big $\mathcal{A}(s)$, ergo very uncertain system. Concluding: fractal basin boundaries with high dimensions make uncertain systems.

The Hénon mapping is just a theoretical model which contains characteristic behaviour like uncertainty. However, we see the behaviour from these theoretical models also back in physical experiments. We now treat such an experiment which lends itself very well in the calculation of the uncertainty exponent.

2.4.2 The pendulum and three magnets

Suppose we have a pendulum attached to a ceiling with at its end a metal ball hanging in the center of three equally strong, equally spaced and equally sized magnets. When we release the pendulum from a position we observe it will converge to one of the magnets. By checking which point converges to a specific magnet we can generate the basins of attraction and consequently the basin boundary.

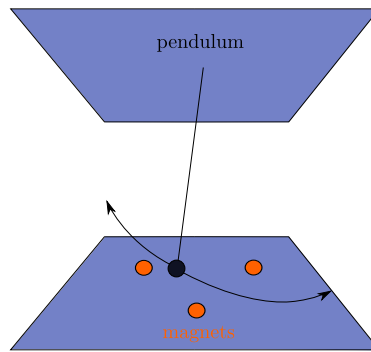


Figure 2.38: The pendulum with a metal ball at its end swinging in between the magnets.

First we make some assumptions on the system:

- The pendulum length is long compared to the distance between magnets. Hence we may assume that the distance from the metal ball to the plane in which the magnets are located stays constant by approximation. This will imply that all the dynamics will be preserved by just making a projection from the xyz -plane onto the xy -plane.
- The magnets correspond to point attractors in the plane.
- The magnets are strong enough such that all points, other than the point of rest in the center of the three magnets, will converge to a magnet.

The point of rest is located at $(0, 0, 0)$. We place the three magnets at the points $(x_i, y_i, 0)$. These magnets are placed at a distance d from the metal ball in the z -plane as suggested in figure 2.39.

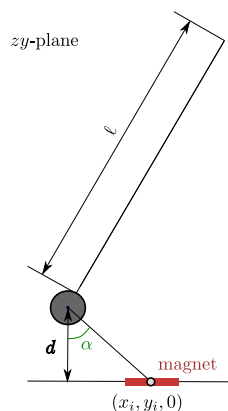


Figure 2.39: Representation of the pendulum in zy -plane.

The second law of Coulomb states that the force of the magnet on the pendulum is inversely proportional to the square of the distance between the two objects. Thus it will be proportional to

$$\frac{1}{(x_i - x)^2 + (y_i - y)^2 + d^2}.$$

The magnets are restricted to the xy -plane hence we will still need multiply the force by the cosine of the angle α as is shown on figure 2.39. After some transformations we obtain that the force of a magnet on the pendulum is proportional to

$$\left(\sqrt{(x_i - x)^2 + (y_i - y)^2 + d^2}\right)^{-1/3} \cdot (x, y)^T$$

[23]. Furthermore we have a gravitational force acting on the pendulum, corresponding to $C \cdot (x, y)^T$, where $C = g/\ell$ with g the gravitational constant and ℓ the length of the pendulum. We also have a frictional force corresponding to $R \cdot (x', y')^T$, where R is the friction constant. We will set the mass of the metal ball equal to one. Using Newton's second law we obtain the four-dimensional system given by

$$\begin{aligned} x'' + Rx' - \sum_{i=1}^3 \frac{x_i - x}{(\sqrt{(x_i - x)^2 + (y_i - y)^2 + d^2})^3} + Cx &= 0 \\ y'' + Ry' - \sum_{i=1}^3 \frac{y_i - y}{(\sqrt{(x_i - x)^2 + (y_i - y)^2 + d^2})^3} + Cy &= 0. \end{aligned} \quad (2.7)$$

We take $(x_1, y_1) = (1, 0)$, $(x_2, y_2) = (-1/2, \sqrt{3}/2)$ and $(x_3, y_3) = (-1/2, \sqrt{3}/2)$.

Equation 2.8 are a set of two ordinary differential equations, which requires a specification of the initial position and velocity. In the numerical experiment that we will be performing we release the magnet from rest (velocity is zero) and then vary the initial position.

We have solved the set of equations 2.8 numerically. Some numerical examples as we release the pendulum from different initial positions are given in figure 2.40.

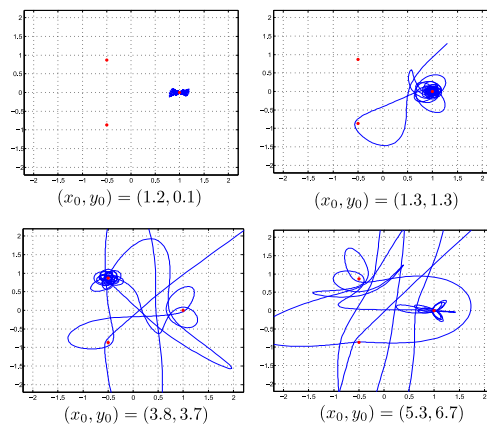


Figure 2.40: The movement of the pendulum (as a projection on \mathbb{R}^2) when released from increasing distance from the magnets. Observe that when the pendulum gets near to one of the magnets the orbit completely changes, which leads to unpredictable behaviour.

We observe that as the pendulum gets near to one of the magnets the orbit changes completely, this leads to unpredictable behaviour.

One can also see the uncertainty present in this system, for if we take two initial values close to each other the pendulum can converge to a different magnet, see figure 2.41.

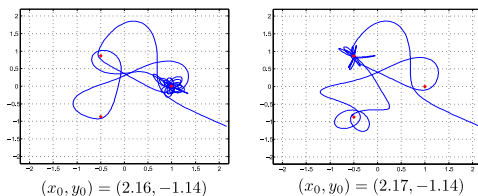


Figure 2.41: Uncertainty in the pendulum: if we release the pendulum at two initial points near to each other the pendulum converges to a different magnet.

We come now to the main experiment: generating the basins of attraction. We release the magnet from rest at an initial position and then indicate with a colour to which magnet it converges. We restrict ourselves to the square region $[-3, 3] \times [-3, 3]$ for 360,000 equidistant initial positions. Furthermore, we will vary R to check what the influence of the friction constant is, the constant corresponding to the gravitational constant will be kept constant ($C = 0.5$). Figure 2.42 displays our numerical result.

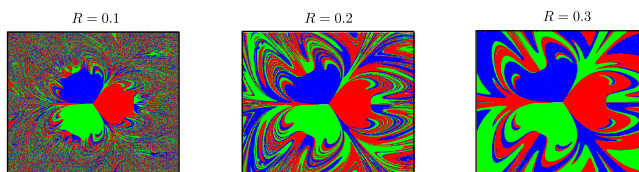


Figure 2.42: Basins of the attraction of the magnets: red $A(1, 0)$, blue $A(-1/2, \sqrt{3}/2)$, green $A(-1/2, -\sqrt{3}/2)$. For decreasing R (decreasing friction).

Observe from 2.42 that as two basins are about to meet that a third basin appears in between them. Upon magnification we would even observe that this property is continued, see figure 2.43 Hence the basin boundary is a fractal.



Figure 2.43: Magnification of the basin of attraction of $R = 0.2$: as two basins of attraction meet, a third basin will appear in between them, this leads to a fractal basin boundary.

With the basins of attraction, we can find the fractal basin boundaries and the corresponding uncer-

tainty exponents. The results are presented in figure 2.44.

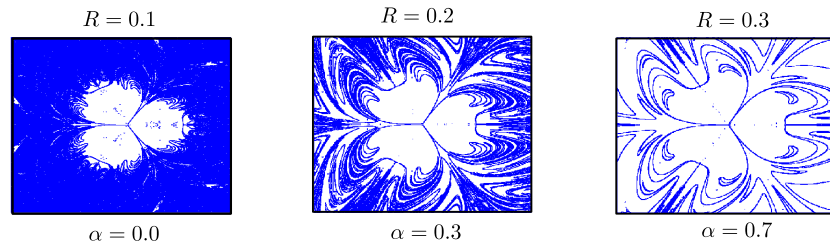


Figure 2.44: The corresponding basin boundaries of the basins of attraction. The system becomes more predictable for increasing R , since the uncertainty exponent increases.

We conclude that as the friction increases, the uncertainty exponent decreases and consequently the system behaves more predictable.

Remarks:

- The numerical calculation of the basins of attraction requires a lot of computation time for a reasonable fine grid of initial positions. One can speed the process slightly up by using the fact that the system is symmetric under a rotation of $2\pi/3$, but since the domain is square shaped we need to calculate a bigger region; rotating the points also requires some time. Consequently we can approximately halve the computation time by using symmetry arguments.
- We have restricted ourselves in varying only the values of R and not C , since the generation of the numerical results took quite a while due to limited numerical resources. Results for varying C can be found in [23].
- Numerically finding the basin boundaries (as is displayed in figure 2.44) is done in the following way: we take a small square around each point in figure 2.42 and then check if the colour changes, if it does we colour the square, and if not we leave the square blank.

Chapter 3

Julia Sets and Mandelbrot set

We continue our investigation of fractal basin boundaries not in \mathbb{R}^2 but in \mathbb{C} . However we still speak of a two-dimensional space since $\mathbb{R}^2 \cong \mathbb{C}$. We will be discussing the basin boundaries generated by rational complex functions. A function $f : \mathbb{C} \rightarrow \mathbb{C}$ is called a rational function if $f(z) = p(z)/q(z)$, where $p(z)$ and $q(z)$ are complex polynomials and if $f(z)$ is of degree greater than one, where the degree is defined as $\deg(f) = \max\{\deg(p(z)), \deg(q(z))\}$, assuming that $p(z)$ and $q(z)$ have no common roots. The basin boundaries corresponding to $f(z)$ are called Julia sets and we will see that in most cases these basin boundaries are fractals.

First we discuss the complex Newton method for complex polynomials which is used to approximate the complex roots. We ask ourselves the question if the complex Newton method always converges to a root except for a set of measure zero, as is the case for the real Newton method. The basin boundaries corresponding to the Newton method are Julia sets. We then continue with an exploration of Julia sets in general. At the end of this section we restrict ourselves to the dynamics corresponding to the Julia sets belonging to $z \mapsto z^2 + c$ with $c \in \mathbb{C}$. Then we divide the Julia sets into two sets: connected sets and Cantor sets. We can then investigate the behaviour of connected sets in the parameter plane, the Mandelbrot set. At the end we find that there exists a local similarity between the Julia sets corresponding to the map $z \mapsto z^2 + c$ and the Mandelbrot set.

3.1 Newton method

If we have a polynomial $f : \mathbb{R} \rightarrow \mathbb{R}$ with roots, we can find these roots by using the (real) Newton method. The Newton method is given by the recursive equation

$$x_n = N_f(x_{n-1}) = x_{n-1} - \frac{f'(x_{n-1})}{f(x_{n-1})}.$$

We shall be referring to N_f as the Newton operator.

As most students would know who have followed a calculus course this will converge to a root r of f , if we choose the initial point x_0 near r and if $N_f(x_n)$ is defined for all $n \geq 0$, but for specific points in a set of zero measure it will blow up or generate periodic behaviour [4].

The function f is defined in \mathbb{R} , so how would this work for a complex polynomial $f : \mathbb{C} \rightarrow \mathbb{C}$? Will we then still see that the initial points which don't converge to a root form a set of measure zero?

3.1.1 Newton method for $z^2 - 1$

The problem of how the Newton method would behave for complex polynomials was stated as early as in 1870 by E. Schröder and also by A. Cayley in 1879 [21]. We start on a historical note and investigate the special case $z^2 - 1$ which was first posed by E. Schröder.

Lemma 3.1.1 *Let $p(z) = z^2 - 1$ and N_p be the associated Newton method, then the basin of attraction for the points $+1$ and -1 is given by*

$$A(+1) = \{z \in \mathbb{C} \mid \operatorname{Re}(z) > 0\}$$

$$A(-1) = \{z \in \mathbb{C} \mid \operatorname{Re}(z) < 0\}$$

The basin boundary denoted by J is given by $J = \mathbb{C} \setminus A(-1) \cup A(+1) = i\mathbb{R}$.

Proof. The proof makes use of transforming the polynomial to a new function such that the basins of attraction become trivial. To this end we will use the Möbius transformation given by

$$T(u) = \frac{u-1}{u+1},$$

with its inverse

$$T^{-1}(u) = \frac{u+1}{u-1}.$$

The Newton operator is then given by

$$N_p(z) = \frac{z^2 + 1}{2z}.$$

Now by making use of the given transformation we find a function to which p is conjugate:

$$T \circ N_p \circ T^{-1}(u) = u^2.$$

Now the choice for the Möbius transformation becomes clear. For T maps 1 to zero, the first point of attraction of u^2 and it maps -1 to infinity the second point of attraction of u^2 i.e.

$$T(A(+1)) = \{u \in \mathbb{C} \mid |u| < 1\},$$

$$T(A(-1)) = \{u \in \mathbb{C} \mid |u| > 1\}$$

and

$$T(i\mathbb{R}) = \{u \in \mathbb{C} \mid |u| = 1\} = \mathbb{S}.$$

Applying T^{-1} will complete the proof of the lemma. \square

We can extend this lemma to a more general case. One can prove in exactly the same way that $p(z) = z^2 - c^2$ has basins of attraction $A(+c)$ and $A(-c)$ with basin boundary $i\mathbb{R}$. We have that $p(z)$ is conjugate to $q(z) = az^2 + zb^2 + d$ by a map $C(z) = az + b$. This brings us to the following theorem.

Theorem 3.1.1 (Basins of attraction of a polynomial of degree 2) *For a polynomial with two roots, z_1, z_2 , the basins of attraction, $A(z_1)$ and $A(z_2)$, are half-planes divided by the line, $J = \mathbb{C} \setminus A(z_1) \cup A(z_2)$, which intersects the line segment z_1 to z_2 perpendicularly in the middle.*

We have now shown that the Newton method always converges to a root for a polynomial of degree 2, except for points on the basin boundary, which form a set of zero measure.

3.1.2 Newton method for $z^3 - 1$

We could now add a degree to $z^2 - 1$ and investigate $p(z) = z^3 - 1$. This is a much more complicated case than $z^2 - 1$. Although A. Cayley himself announced that he would present a paper on this polynomial, it actually never appeared. About fifty years later G. Julia and P. Fatou found an explanation for the difficulties that arise [21].

We know that the given polynomial has 3 roots: 1 , $e^{\frac{2}{3}\pi i}$ and $e^{-\frac{2}{3}\pi i}$. The Newton operator is given by

$$N_p(z) = \frac{2z^3 + 1}{3z^2}.$$

The problem now is how to divide \mathbb{C} over the basins of attraction, $A(1)$, $A(e^{\frac{2}{3}\pi i})$, $A(e^{-\frac{2}{3}\pi i})$ and a remaining set J . On basis of lemma 3.1.1 we might expect that \mathbb{C} is divided into three equal parts that are separated by three lines which meet up in the origin; this idea is wrong as the numerical result in figure 3.1 indicates.

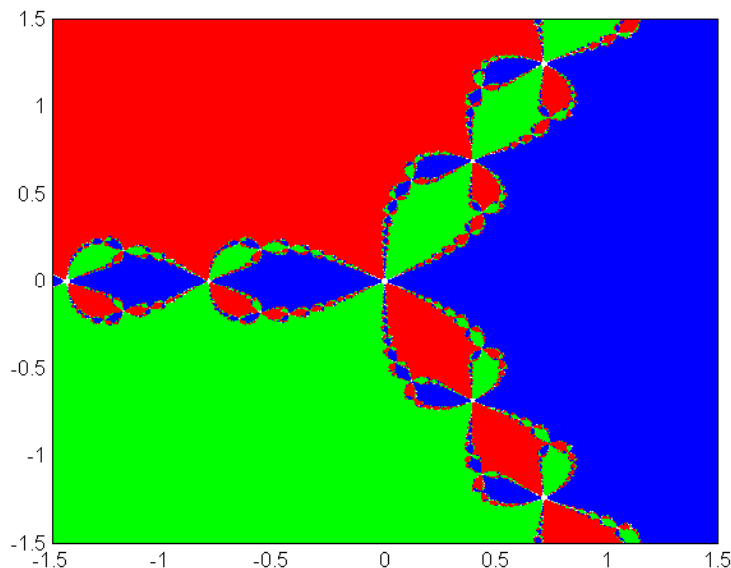


Figure 3.1: Basins of attraction of the Newton method for $z^3 - 1$: blue $A(1)$, red $A(e^{\frac{2}{3}\pi i})$ and green $A(e^{-\frac{2}{3}\pi i})$.

This plot of the basins of attraction provides us with a view on the infinite complexity of the basin boundary. We are once again dealing with a fractal basin boundary.

One observes that under a rotation D of $\frac{2}{3}\pi$ one has that $N_p(z) = D \circ N_p \circ D^{-1}(z)$. Furthermore one has that ∞ is a repelling fixed point ($N_p(\infty) = \infty$, $N'_p(\infty) > 1$) and $N_p(0) = \infty$. One sees that all boundary points are three-corner points i.e. every point on the basin boundary lies on the boundary of all three basins of attraction.

Theorem 3.1.2 (Three-corner point) *Every point on the basin boundary, J , corresponding to the Newton method of $z^3 - 1$, is a three-corner point.*

Proof. We are going to use the fact that 0 is a three corner point. Then we will show that there exists a map connecting an open ball around zero to any point on the basin boundary.

We will call the basin boundary J . Let $x \in J$ and U be an arbitrarily small neighbourhood of x . Assume now that the following holds

$$\{z | N_p^k(z) = 0 \quad k = 0, 1, 2, \dots\} \text{ is dense in } J.$$

We will present this statement formally with proof in corollary 3.2.2.

Then we have that there is a $y \in U \cap R$ such that $N_p^k(y) = 0$ for a k . $N'(y) \neq 0$ for all $y \in \mathbb{C} \setminus \{+1, e^{\frac{2}{3}\pi i}, e^{-\frac{2}{3}\pi i}\}$ thus it is invertible in a small neighbourhood of y ; we will call this neighbourhood V . Thus we have that there exists an open ball $B_\epsilon(0)$ and a $k \in \mathbb{N}$ such that $N_p^k : V \rightarrow B_\epsilon(0)$

is bijective. Now take a look at the interval $I_\epsilon = (0, \epsilon) \subset \mathbb{R}$ inside $B_\epsilon(0)$; with some elementary calculus we can prove that $I_\epsilon \subset A(1)$. Furthermore, due to the symmetry relation we pointed out, we get $D(I_\epsilon) \subset A(e^{\frac{2}{3}\pi i})$ and also $D(D(I_\epsilon)) \subset A(e^{-\frac{2}{3}\pi i})$, thus zero is a three-corner point. Due to the bijectivity we get that U must as well contain points from three different basins. Since we have chosen U arbitrarily, this will imply that all points are three-corner points. \square

The numerical result $z^3 - 1$ in figure 3.1 gives good grounds for the hypothesis that all points converge to a root except for a set of measure zero. Similarly to $z^2 - 1$ we can ask ourselves if $z^3 - 1$ extends to the more general case, $q(z) = az^3 + bz^2 + dz + e$ and consequently that all complex polynomials of degree 3 converge to a root except for a set of measure zero. This is not true in general, there exists complex polynomials such that the Newton method doesn't converge to a root for a set of full measure. Take for example the polynomial $p(z) = z^3 + (-0.71 + 1.62i)z - 0.31 + 1.62i$. This polynomial has three roots which are approximately 1, $0.3835 - 0.9168i$ and $-1.3835 + 0.9169i$. In figure 3.2 we numerically generated the corresponding basins of attraction.

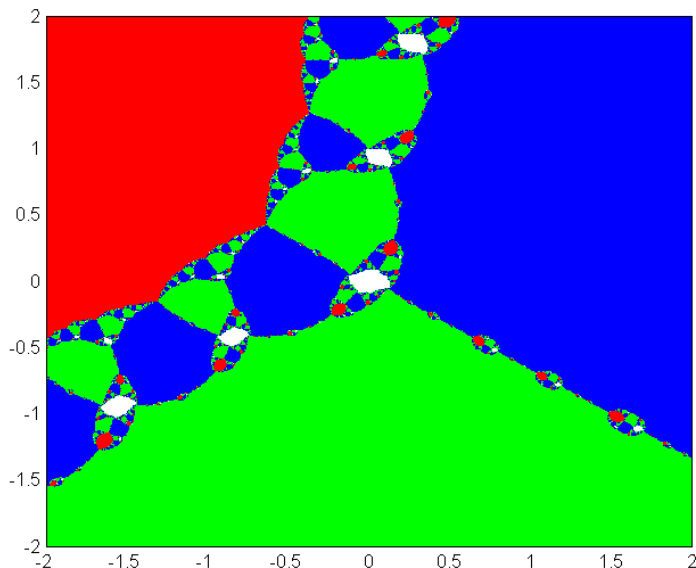


Figure 3.2: Basins of attraction for the Newton method of $z^3 + (-0.71 + 1.62i)z - 0.31 + 1.62i$: blue $A(1)$, red $A(0.3835 - 0.9168i)$ and green $A(-1.3835 + 0.9169i)$. The white area (with interior) corresponds to points which don't converge to a root. The interior of the white area converges to an attractive period two orbit.

Since the white area in figure 3.2, which corresponds to points which don't converge to any root, has full measure, this specific polynomial yields a counter example.

A more extensive numerical investigation of Newton methods of degree 3 and their basins of attraction can be found in [31, 12].

3.2 Julia sets

First concerning notation. We denote the Riemann sphere by $\hat{\mathbb{C}} = \mathbb{C} \cup \{\infty\}$; a short introduction to the Riemann sphere can be found in Appendix D. The open unit circle shall be denoted as \mathbb{D} .

We will now turn to a variety of sets to which the basin boundaries of the Newton method earlier treated also belong: Julia sets.

Definition 3.2.1 (Julia sets in $\hat{\mathbb{C}}$) *Let $f : \hat{\mathbb{C}} \rightarrow \hat{\mathbb{C}}$ be a rational function of degree greater than one, then the domain for which the every subsequence of the set $\{f^n\}$ with $n \in \mathbb{Z}_+$ diverges locally uniformly and converges locally uniformly (i.e. normality domain) is called the Fatou set, F_f . The Julia set, J_f , is given by $\hat{\mathbb{C}} \setminus F_f$.*

We will assume that f is a complex rational function of degree greater than one unless noted differently. This is done since most of the treated statements can't be extended to complex rational functions of degree one.

Remark: Definition 3.2.1 resembles closely the classical definition given by Fatou. Technically one defines the Julia set on a Riemann surface which is a connected complex manifold of complex dimension one. The Riemann sphere is an example of a Riemann surface, for a more extensive treatment of Riemann surfaces we refer to [26]. Since we will only be dealing with $\hat{\mathbb{C}}$ we have restricted the definition of Julia set to the Riemann sphere.

Some basic properties which follow almost directly from 3.2.1 are

- $J_f \neq \emptyset$.
- J_f is compact.
- $f(J_f) = f^{-1}(J_f) = J_f$, i.e. J_f is completely invariant.

The proofs of these statements are not too difficult; they can be found in most literature about Julia sets we refer to [5, 26].

An example of a Julia set is the one generated by $z \mapsto z^2$. We then have that $|z| < 1$ will converge uniformly to zero and $|z| > 1$ will diverge uniformly, thus the corresponding Julia set, J_{z^2} , is the boundary of the unit circle also written as $\partial\mathbb{D}$.

The definition 3.2.1 doesn't really give an idea how to graphically compute Julia sets. For Julia sets corresponding to complex polynomials we have the following equivalent definition:

Equivalent Definition 3.2.1 (Julia sets for complex polynomials) *Let $f : \hat{\mathbb{C}} \rightarrow \hat{\mathbb{C}}$ be a complex polynomial. The filled Julia set corresponding to f is then given by*

$$K_f = \{z \in \mathbb{C} \mid \lim_{n \rightarrow \infty} f^n(z) \text{ is bounded}\}.$$

The Julia set of f is then given by $J_f = \partial K_f$.

The proof that these definitions are equivalent for a complex polynomial f can be found in [26].

From the equivalent definition 3.2.1 we can straightforwardly numerically compute Julia sets. In figure 3.3 we have given some examples.

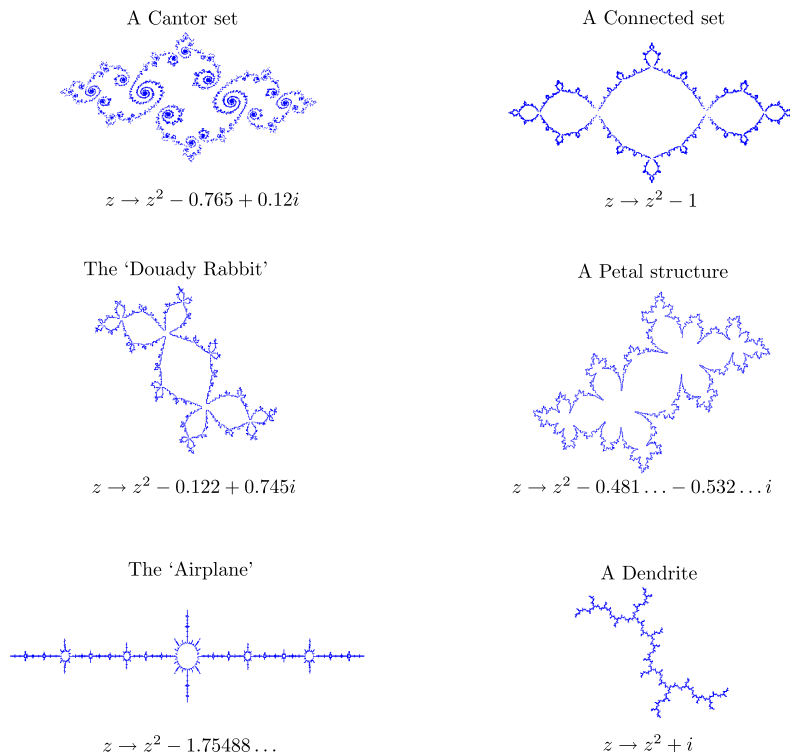


Figure 3.3: Some examples of Julia sets for the mapping $z \mapsto z^2 + c$ with $c \in \mathbb{C}$.

We will prove that Julia sets corresponding to complex polynomials can be divided into two groups (see theorem 3.2.6) : connected sets and Cantor sets (, i.e. sets with infinite connected components of Lebesgue measure zero). This result extends to any complex rational function in the sense that a Julia set is either connected or has uncountably many connected components [26]. These connected sets can be subdivided into several cases: $\text{Int}(K_f)$ can be non-empty or empty, the latter case is called a dendrite; they can have petals which are located at their fixed points and there are also some exceptional cases such as the 'Douady Rabbit' and the 'Airplane', see figure 3.3. Also observe that in general Julia sets are not smooth as was the case with J_{z^2} .

In figure 3.3 we have restricted ourselves to the quadratic case. One can obtain a more diverse family when one investigates polynomials of higher degree or the non-polynomial case, we refer to [26].

3.2.1 Characterization of periodic points for Julia sets

Let us first recall the definition of complex analytic or holomorphic.

Definition 3.2.2 (Complex analytic or holomorphic) For $V \subset \mathbb{C}$ we call a mapping $f : V \rightarrow \mathbb{C}$ complex analytic or holomorphic if the first derivative

$$z \mapsto f'(z) \quad f'(z) = \lim_{h \rightarrow 0} \frac{f(z+h) - f(z)}{h}$$

is defined and continuous from V to \mathbb{C} .

To characterize the stability of periodic n -orbits we need to compute the corresponding n th derivative. Thus we have the following definition.

Definition 3.2.3 (The eigenvalue of a periodic point) For a complex analytic map $f : \mathbb{C} \rightarrow \mathbb{C}$ the eigenvalue or multiplier corresponding to a periodic n -orbit of z_0 is given by

$$\lambda := (f^n(z))'|_{z=z_0}.$$

We can rewrite the above expression by applying the chain rule to the n -orbit $\{z_0, z_1, \dots, z_{n-1}\}$ and obtain the following alternative method to calculate the eigenvalue.

$$\lambda = f'(z_0) \cdot f'(z_1) \cdot \dots \cdot f'(z_{n-1}) = (f^n)'(z_j) \quad \forall j = 0, 1, \dots, n-1$$

We can divide the periodic points into four groups.

Definition 3.2.4 (Characterization of periodic points) A periodic point z_0 is called

- attractive if and only if $|\lambda| < 1$. With geometric attractive if and only if $0 < |\lambda| < 1$ and superattractive if and only if $|\lambda| = 0$.
- indifferent if and only if $|\lambda| = 1$.
- repelling if and only if $|\lambda| > 1$.

In the special case that we have a rational polynomial f with $f(\infty) = \infty$, then the eigenvalue is not given by the corresponding derivative. One even has that the eigenvalue of ∞ is superattractive (for $\deg(f) \geq 2$). Hence the following proposition.

Proposition 3.2.1 For f a complex polynomial with a fixed point at infinity, the eigenvalue at infinity is given by

$$\lambda = \lim_{z \rightarrow \infty} \frac{1}{f'(z)}.$$

Furthermore this fixed point is superattractive if and only if $\lim_{z \rightarrow \infty} f'(z) = \infty$.

Proof. The trick of the proof is to move the fixed point at infinity to zero by a conjugacy. Take $z(\zeta) = 1/\zeta$, then we have that

$$z \circ f \circ z^{-1}(\zeta) = \frac{1}{f(\frac{1}{\zeta})}.$$

Now we can use the series expansion

$$\frac{1}{f(\frac{1}{\zeta})} = a_0\zeta + a_1\zeta^2 + \dots$$

for some ζ in a neighbourhood of zero. It follows from the transform that $a_0 = \lambda$. By taking the derivative on both sides we obtain that $\lambda = 1/f'(1/\zeta)$ for $\zeta \rightarrow 0$. It follows that this fixed point is superattractive if and only if $\lim_{z \rightarrow \infty} f'(z) = \infty$. \square

With the previous statements we can give a description of how the attractive and repelling orbits are divided over the Julia and Fatou set.

Proposition 3.2.2 (Basins of attraction and repelling points) The entire basin of attraction A of any attracting orbit is contained in the Fatou set. However every repelling orbit is contained in the Julia set.

Proof. Let us first consider only fixed points $z_0 = f(z_0)$ with eigenvalue λ , the cases for other periods follow from this case. If $|\lambda| > 1$ (repelling) then points cannot converge near z_0 for the corresponding derivative of $f^n(z_0)$ is given by λ^n , which for $n \rightarrow \infty$ will diverge from z_0 . Hence $z_0 \in J$.

If $|\lambda| < 1$ (attracting) then we know by the mean value theorem that there exists a c with $\lambda < c < 1$ such that

$$|f(z) - z_0| \leq c|z - z_0|$$

applies for a z sufficiently close to z_0 . Thus we have that points in a neighbourhood of z_0 converge uniformly to z_0 , hence z_0 is contained in the Fatou set. This extends to any compact subset of a basin of attraction A .

All of this will also apply to m -periodic orbits because these correspond to fixed points under f^m . \square

The indifferent case still remains; how these are divided over the Julia set and Fatou set is in general more difficult. For an extensive treatment see [26]. However there is one particularly important case which we like to treat: parabolic points.

Definition 3.2.5 (Parabolic points) *The eigenvalue of an indifferent periodic point with $z_0 = f^n(z_0)$ is called parabolic if the eigenvalue, λ , satisfies the condition that there exists a q such that $\lambda^q = 1$ and f^n isn't equal to the identity map.*

We now have the following property for Julia sets.

Proposition 3.2.3 (Parabolic point) *Every parabolic point belongs to the Julia set.*

Sketch of proof The idea is to write f^n as a power series; in doing so we will find that the corresponding derivative of f^{nk} for $k \rightarrow \infty$ will diverge, implying that points near the parabolic point cannot converge uniformly and thus are contained in the Julia set. For a full proof we refer to [26]. \square

The eigenvalue of a parabolic point can also be written as $\lambda = e^{2\pi ip/q}$ with the fraction $p/q \in \mathbb{Q}$ in its lowest terms. Thus parabolic points are also called rationally indifferent periodic points.

When one numerically generates Julia sets corresponding to parabolic fixed points, one observes that several petals are connected to the fixed point, see figure 3.4.

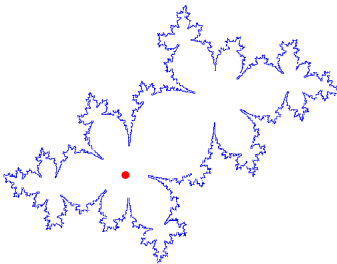


Figure 3.4: Julia set $z \mapsto z^2 - 0.481\dots - 0.532\dots i$ with a parabolic fixed point indicated with the red dot. Observe that the ‘petals’ are attached to this fixed point.

The fact that this phenomenon occurs around all parabolic periodic points can be proven, we refer to the Parabolic Flower theorem which can be found in [26].

The question arises what happens when $\lambda = e^{2\pi\alpha i}$ with $\alpha \notin \mathbb{Q}$. We then have the Siegel disk case or a Julia set with an irrationally indifferent periodic point. The behaviour around such points is rather difficult. We shall not investigate these and refer to [26]. Nonetheless we present the reader with a numerical example, see figure 3.5.

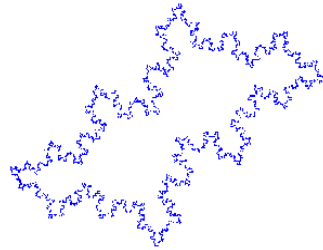


Figure 3.5: Siegel disk case Julia set for the mapping $z \mapsto z^2 + \lambda z$ with $\lambda = e^{2\pi i\alpha}$, $\alpha = (\sqrt{5} - 1)/2$.

For a more extensive numerical discussion we refer to [31] and for a theoretical discussion to [26].

Remark: Julia sets corresponding to indifferent periodic points are notoriously difficult to generate [31]. From our generated figures we see that especially figure 3.4 doesn't give a satisfactory result since the 'petals' which are attached to the parabolic fixed point should only be attached to the fixed point and not to each other as figure 3.4 implies.

3.2.2 Transitivity

We come now to a theorem from which a lot of properties for the Julia set will follow.

Theorem 3.2.1 (Transitivity) *Let z_0 be an arbitrary point of the Julia set $J_f \subset \hat{\mathbb{C}}$. Let V be an arbitrary neighbourhood of z_0 ; we then have that $U = \bigcup_{n=0}^{\infty} f^n(V)$ contains the entire Julia set as well as $\hat{\mathbb{C}}$, except for at most two points in $\hat{\mathbb{C}}$.*

A full proof would require an extensive treatment of complex analysis; therefore we will give only a short sketch of the proof, a full proof can be found in [26].

Sketch of proof. Assume that $\hat{\mathbb{C}} \setminus U$ can contain at most two points, this follows from Montel's theorem [26]. We have that $f(U) \subset U$, thus for $z_0 \in \hat{\mathbb{C}} \setminus U$ we have that the preimages must also be contained inside $\hat{\mathbb{C}} \setminus U$. Suppose now that $z_0 \in J_f$. By construction it follows that z_0 is in a periodic orbit which gets bijectively mapped under f onto itself,

$$z_0 \mapsto z_1 \mapsto \dots \mapsto z_m.$$

Since this happens bijectively we will have that every z_j is a multiple root since $\deg(f) \geq 2$. Hence it follows that z_j will be a critical point, i.e. superattractive point. Since superattractive points aren't contained in J_f this completes the proof. \square

We now have the following corollaries:

Corollary 3.2.1 (Julia set with interior) *If the Julia set has an interior point then it equals the the complete Riemann sphere, $\hat{\mathbb{C}}$.*

Proof. Take $z_0 \in \text{Int}(J_f)$ and V an open neighbourhood around z_0 we then have that the union under forward images $U \subset J_f$ has $\bar{U} = \hat{\mathbb{C}}$ and thus, since the Julia set is closed we obtain that the Julia set is equal to the entire Riemann sphere. \square

Corollary 3.2.2 (Iterated preimage are dense) *For $z_0 \in J_f$, the set of all iterated preimages*

$$\{z \in \mathbb{C} \mid f^k(z) = z_0, k = 0, 1, 2, \dots\}$$

is dense in J .

Proof. This follows directly from 3.2.1. \square

Corollary 3.2.3 (Julia set is connected or disconnected) *For any rational f we have that the Julia set is connected or contains infinitely many connected components i.e conformally isomorphic to the Cantor set.*

We will prove a stronger version of this corollary later for Julia sets generated by complex polynomials, see theorem 3.2.6. A proof of corollary 3.2.3 can be found in [26].

3.2.3 Digression into topology: formalizing IFS

In chapter 2 we have already come across the concept of IFS, iterated function system. An IFS is a metric space together with a set of contracting transformations with which we can recursively construct a fractal. We will now formalize this concept.

We first introduce the space on which IFS performs transformations: the fractal space.

Definition 3.2.6 (Definition of the fractal space) *Let (X, d) be a complete metric space. The fractal space, $F(X)$, is defined to be the space whose points are the compact subsets of X , other than the empty set.*

Definition 3.2.7 (Metric space definitions on $F(X)$) *Let (X, d) be a complete metric space, $x \in X$ and $A, B \in F(X)$.*

1. Define the distance from the the point x to the set B by

$$d(x, B) = \min\{d(x, y) : y \in B\}.$$

2. Define the distance between the sets A, B by

$$d(A, B) = \max\{d(x, B) : x \in A\}.$$

3. **(Hausdorff distance)** *The Hausdorff distance between the points $A, B \in F(X)$ is given by*

$$h(A, B) = \max\{d(A, B), d(B, A)\}.$$

We denote the Hausdorff distance on a metric d by $h(d)$.

Remarks:

- Observe that if we have a $x, y \in F(X)$ then $x \cup y \in F(X)$, however $x \cap y$ doesn't have to be in $F(X)$. As the figure 3.6 illustrates.

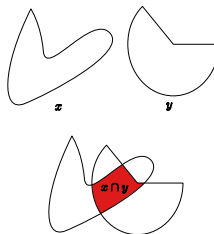


Figure 3.6: One can view x and y as points in $F(X)$, then $x \cap y$ won't necessarily be contained in $F(X)$.

- It won't necessarily hold that $d(A, B) = d(B, A)$. Hence $d(A, B)$ doesn't define a metric in $F(X)$.
- $h(d)$ is a metric on the space $F(X)$. The proof can be found in [5].

Before defining IFS we need one more definition.

Definition 3.2.8 (Contractivity factor) *A given transformation $f : X \rightarrow X$ on a metric space (X, d) is called contracting if there exists a constant s with $0 \leq s \leq 1$ such that*

$$d(f(x), f(y)) \leq s \cdot d(x, y) \quad \forall x, y \in X.$$

We will refer to this 's' as the contractivity factor of f .

Definition 3.2.9 (Definition IFS) *An (hyperbolic) iterated function system (IFS) consists out of a complete metric space (X, d) and a finite set of contraction mappings $w_n : X \rightarrow X$ each with a contractivity factor s_n , for $n = 1, 2, \dots, N$. The IFS will then be denoted by $\{X : w_n, n = 1, 2, \dots, N\}$. The contractivity of the system will then be defined as $s = \max\{s_n : n = 1, 2, \dots, N\}$.*

We come now to a theorem which will give us a method to construct Julia sets with IFS.

Theorem 3.2.2 (Computation of invariant set with IFS) *Let (Y, d) be a metric space. Take a non-empty $X \subset Y$ to be compact. Let $f : X \rightarrow Y$ be a continuous function such that $f(X) \supset X$. (1) Then a transformation $W : F(X) \rightarrow F(X)$ is defined by*

$$W(A) = f^{-1}(A) \quad \forall A \in F(X).$$

(2) W possesses a fixed point $A \in F(X)$, given by

$$A = \bigcap_{n=0}^{\infty} f^{-n}(X) = \lim_{n \rightarrow \infty} W^n(X).$$

If the additional condition holds that $f(U)$ is an open subset of the metric space $(f(X), d)$, whenever $U \subset X$ is an open set of the metric space (X, d) . Then (3) W is a continuous transformation from the metric space $(F(X), h(d))$ onto itself. (4) If f has the domain the whole of Y and in addition to $f(X) \supset X$, also holds that $f^{-1}(X) \subset X$, then (1) (2) (3) hold.

Proof (1) We start with proving that $W : F(X) \rightarrow F(X)$. Thus we need to prove that for a $B \in F(X)$ that $f^{-1}(B) \neq \emptyset$ and that $f^{-1}(B)$ is compact. From the given property that $f(X) \supset X$ we have that $f^{-1}(B) \neq \emptyset$. By continuity of f we have that $f^{-1}(B)$ is closed in the metric (X, d) . Using $f(B) \supset X$ and the fact that X is compact we obtain $f^{-1}(B)$ compact. With this we have proven (1).

(2) Since f has domain X , it follows that $X \supset f^{-1}(X)$. Applying f^{-1} multiple times on both sides we obtain

$$X \supset f^{-1}(X) \supset f^{-2}(X) \supset \dots \supset f^{-n}(X) \supset \dots$$

Thus $f^{-n}(X)$ is a Cauchy sequence in $F(X)$, so it converges to a limit $A = \bigcap_{n=0}^{\infty} f^{-n}(X) = \lim_{n \rightarrow \infty} W^n(X)$.

The prove that A is a fixed point is still left, but this is trivial. We need to show that

$$f^{-1} \left(\bigcap_{n=0}^{\infty} A_n \right) = \bigcap_{n=0}^{\infty} A_n \text{ with } A_n = f^{-n}(X), n \in \mathbb{Z}_+.$$

It holds that for any sets D_1 and D_2 that

$$f^{-1}(D_1 \cap D_2) = f^{-1}(D_1) \cap f^{-1}(D_2),$$

thus

$$f^{-1} \left(\bigcap_{n=0}^{\infty} A_n \right) = \bigcap_{n=0}^{\infty} A_{n+1} = \bigcap_{n=1}^{\infty} A_n = \bigcap_{n=0}^{\infty} A_n ,$$

because f^{-1} contracts A_n .

(3) From the fact that $f(U)$ is an open subset of the metric space $(f(X), d)$, whenever $U \subset X$ is an open set of the metric space (X, d) . It follows that f^{-1} is continuous in the given metrics. We need to prove that given any ϵ there exists a δ such that

$$h(A, B) < \delta \Rightarrow h(f^{-1}(A), f^{-1}(B)) < \epsilon, \quad \forall A, B \in F(X).$$

There exists $x \in A, y \in B$ such that $h(A, B) = d(x, y)$. Similar we have $\tilde{x} \in f^{-1}(A), \tilde{y} \in f^{-1}(B)$ such that $h(f^{-1}(A), f^{-1}(B)) = d(f^{-1}(\tilde{x}), f^{-1}(\tilde{y}))$ (since f^{-1} is continuous). From the property $f^{-1}(X) \subset X$ we get that $h(f^{-1}(A), f^{-1}(B)) = d(\tilde{x}, \tilde{y}) < d(x, y) = h(A, B) < \epsilon$.

(4) Observe if (4) is satisfied (1)(2) immediately follow. Only statement (3) remains. It follows from (4) that f^{-1} must be continuous, we can now proceed in the same way as we did in (3). \square

We would like to establish a connection between IFS and Julia sets. It seems plausible that we can create an IFS with a Julia set as a attracting set. We will specifically investigate the Julia sets, J_c , for $z^2 + c$ with $c \in \mathbb{C}$. IFS is attracting and the Julia set is repelling, so the inverse transform of the iterator might lead to the desired IFS. The inverse can be solved by

$$z = w^2 + c \iff w_1 = \sqrt{z + c}, \quad w_2 = -\sqrt{z + c}.$$

We order these equations for the solutions and write for $f^{-1}(z) = \{w_1(z), w_2(z)\}$. The IFS will then be given by $\{\hat{\mathbb{C}}; w_i, i = 1, 2\}$. The system however doesn't attract the Julia sets in complete $\hat{\mathbb{C}}$, furthermore we have that $\bigcup_{i=1}^2 w_i(\hat{\mathbb{C}}) = \hat{\mathbb{C}}$. The reason why this happens is that all attracting orbits of f turn into repelling orbits for f^{-1} . Look for example what happens at the point at infinity. So we actually want to remove all attracting points of f from $\hat{\mathbb{C}}$. One could say that we remove the 'rotten pieces' of the Riemann sphere. Using 3.2.2 we can prove the following proposition.

Proposition 3.2.4 (IFS for Julia sets corresponding to $z^2 + c$) *Suppose that the map $f_c : \hat{\mathbb{C}} \rightarrow \hat{\mathbb{C}}$ with $f_c(z) = z^2 + c$ and $c \in \mathbb{C}$, has an attractive cycle $\{z_0, z_1, \dots, z_n\} \subset \mathbb{C}$. Define $X = \hat{\mathbb{C}} \setminus (B_\epsilon(z_0) \cup B_\epsilon(z_1) \cup \dots \cup B_\epsilon(z_n) \cup B_\epsilon(\infty))$, with $\epsilon > 0$. Define the IFS by $\{X; w_1(z) = \sqrt{z^2 + c}, w_2(z) = -\sqrt{z^2 + c}\}$. Then $W : F(X) \rightarrow F(X)$ is given by*

$$W(B) = w_1(B) \cup w_2(B) \quad \forall B \in F(X).$$

Furthermore W is continuous with respect to the Hausdorff metric.

W then possesses a unique fixed point:

$$\lim_{n \rightarrow \infty} W^n(B) = J_c.$$

Sketch of proof. By making use of theorem 3.2.2 we can prove that the given $W : F(X) \rightarrow F(X)$ is continuous and that it possesses a fixed point. f is indeed analytic on $\hat{\mathbb{C}}$. f maps open sets unto open sets. Thanks to the construction of X we also have that $f(X) \supset X$ (for small enough ϵ) and finally we also have that $f^{-1}(X) \subset X$. The only problem is to prove that the fixed point $\lim_{n \rightarrow \infty} W^n(X) = J_c$. Let us give a sketch of how this is done. Suppose that $\lim_{n \rightarrow \infty} W^n(X) \neq J_c$ then there exists a uniformly converging orbit or a diverging orbit for f . This cannot be the case since the point at infinity and all attractive cycles were removed. The full proof of this last part can found in [9] lemma 6.3. \square

In a similar manner to proposition 3.2.4 one can show that there exists an IFS for the Newton method

corresponding to $z^3 - 1$; we then remove open balls around the roots of $z^3 - 1$, we leave the details to the reader [5]. Proposition 3.2.4 can even be generalized to every complex polynomial in $\hat{\mathbb{C}}$. For a sketch of the proof we refer to [5].

3.2.4 Computer graphical generation of Julia sets

Numerically generated Julia sets are in many cases crucial to understand the dynamics. We would like to calculate Julia sets as efficient and accurate as possible. There are a number of ways to do this. For simplicity we just investigate J_f generated by $f_c(z) := z^2 + c$ with $c \in \mathbb{C}$; hence we write $J_f = J_c$ and $K_f = K_c$.

Direct method

The direct method straightforwardly uses the definition of the filled Julia set (definition 3.2.1). We create a program that checks if the n th iterate exceeds a certain big number. We would like to make this ‘big’ number as small as possible. This will lead us to the following proposition.

Proposition 3.2.5 *Take $z, c \in \mathbb{C}$ with $|c| \leq |z|$ and $2 < |z|$, then it follows that $z \notin K_c$*

One can prove proposition 3.2.5 by using elementary calculus, for a proof see [23].

Applying this proposition, we can numerically generate a given K_c more efficiently. One still needs to check if a point lies on the boundary of K_c to generate J_c . The direct method costs a lot of computer time and is not so efficient since just a small percentage of the points checked will finally belong to J_c .

IIM and MIIM

Proposition 3.2.4 states that by backward iterating we can generate a Julia set. However the theorem requires that we remove all attractive cycles. The attractor at infinity won’t give a problem, but possible attracting points in $\mathbb{C} \setminus J_c$ might give a problem. From corollary 3.2.2 we have that

$$\text{for } z \in J_c, \{z \in \mathbb{C} \mid f_c^k(z) = z_0, k = 0, 1, 2, \dots\} \text{ is dense in } J_c.$$

Proposition 3.2.4 will then guarantee that points near to J_c will also converge to J_c or in other words: backwards iterating is stable. Thus by just finding a point on the basin boundary one can generate the corresponding Julia set, this method is called inverse iteration method, IIM.

In figure 3.7 we display the result of J_{-1} by backwards iterating a $z_0 \in J_{-1}$ ten times.

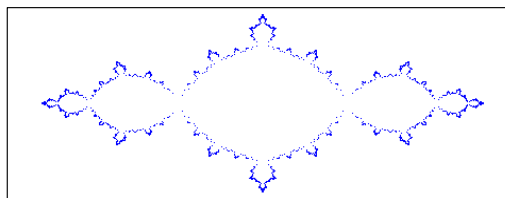


Figure 3.7: IIM after ten iterations for J_{-1} . Observe that iterates tend to the end points of the Julia set.

As theorem 3.2.2 suggests, IIM works recursively. The inverse splits itself at each iteration into two branches. One sees that the iterates tend to the end points of the Julia sets, this leads to an unsatisfactory result with a lot of useless data points. To counter this problem, we put a square lattice

with mesh size ϵ over the calculated data points, we then remove h points if we can find more than k points inside a single square. This method is called modified inverse iteration method, MIIM. It leads to good approximations of Julia sets in acceptable calculation time. In figure 3.8 we have numerically generated J_{-1} with IIM and MIIM with an almost equal amount of data-points; one immediately sees how well MIIM works.

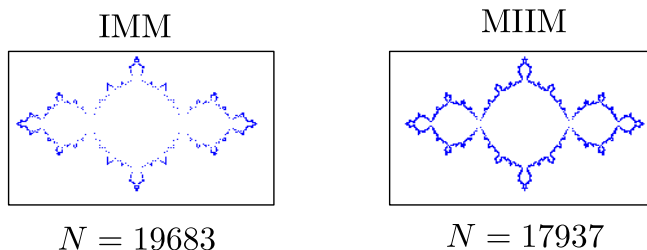


Figure 3.8: IIM versus MIIM: Observe how much better MIIM approximates J_{-1} in comparison to IIM.

Remarks: Julia sets containing parabolic fixed points or Julia set which are isomorphic to Cantor sets are notoriously difficult to generate with MIIM. There are methods to counter the occurred problems, we won't be treating these and refer to [31].

3.2.5 Dynamics of Julia sets: equipotential curves and field lines

$\mathbb{C} \setminus K_f$ can be subdivided in such a way that it will reveal the dynamics of J_f . This method was developed by A. Douady and J. H. Hubbard and makes use of an analogy to electrodynamics. We will only be treating the maths behind this method, for a physical interpretation we refer to [23]

In this section we assume that f is a complex polynomial of degree greater or equal to two. For all the examples we only consider the polynomial $f_c(z) := z^2 + c$ with $c \in \mathbb{C}$. Furthermore we define $J_{f_c} := J_c$, $K_{f_c} := K_c$ and $F_{f_c} := F_c$.

Dynamics of z^2

Douady and Hubbard developed a conjugacy between z^2 and $z^2 + c$. In doing so we can relate the dynamics of J_0 to J_c . We will start with the dynamics of J_0 .

Suppose we have a hole in the floor with radius $r = 1$ and let water flow up from the hole. The water will be spread equally in all directions. The amount of water that flows from this hole per second corresponds to the charge, Q . We can formalize this by using the complex potential, which is an analytic function given by $\chi(z) = \mathcal{F}(z) + i\mathcal{G}(z)$, where $\text{Re}(\chi(z)) = \mathcal{F}(z)$ and $\text{Im}(\chi(z)) = \mathcal{G}(z)$. $\mathcal{F}(z)$ is called the potential function and $\mathcal{G}(z)$ is called the stream function. An *equipotential curve* is given by $\mathcal{F} = \text{constant}$ and corresponds to a curve which acts as a separator between the wet and dry floor at a future time. A *field line* is given by $\mathcal{G} = \text{cst}$ and corresponds to the path which a water particle travels. For this problem the complex potential is given by

$$\chi = \frac{Q}{2\pi} \log z = \frac{Q}{2\pi} (\log r + i\theta) \Rightarrow \mathcal{F} = \frac{Q}{2\pi} \log r, \quad \mathcal{G} = \frac{Q}{2\pi} \theta \quad \text{with } r > 1. \quad (3.1)$$

We will assume that $Q = 2\pi$.

From equation 3.1 we conclude that the equipotential curves are given by circles with $r > 1$ and that the field lines are lines with constant angles, see figure 3.9.

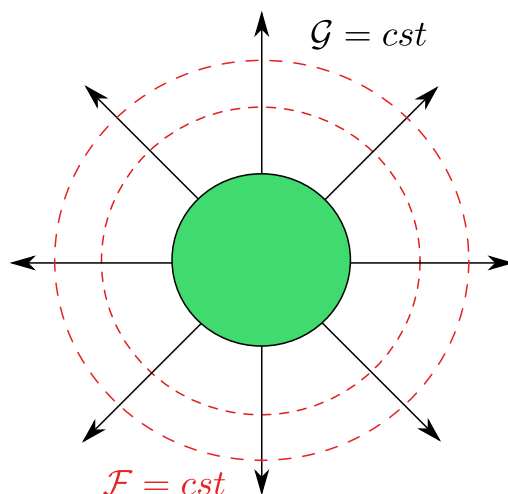


Figure 3.9: A source, the green circle, with corresponding equipotential curves $\mathcal{F} = cst$ and field lines $\mathcal{G} = cst$.

Let us couple this to $J_0 = \partial\mathbb{D}$: place the source in J_0 and draw equipotential curves and field lines as given in the above statements. The iterator corresponding to J_0 , $z \mapsto z^2$, can also be applied to the equipotential curves and field lines. A single iteration applied to an equipotential curve will square the radius, since

$$f_0 : re^{\theta i} \mapsto r^2 e^{2\theta i} \quad \text{with } 0 \leq \theta < 2\pi \text{ and } r = cst.$$

A single iteration applied to a field lines will double the angle, since

$$f_0 : re^{\theta i} \mapsto r^2 e^{2\theta i} \quad \text{with } 1 < r < \infty \text{ and } \theta = cst.$$

The source will stay unchanged under iteration of f_0 , since $K_0 = \overline{\mathbb{D}}$.

To reveal some of the dynamics of the field lines consider writing an angle θ of a field line as $\theta = \alpha \cdot 2\pi$ with $0 \leq \alpha < 1$. Then the angle doubling of f_0 is equivalent $B : \alpha \mapsto 2\alpha \pmod{1}$. One might have noticed that this is the Baker transformation treated in section 2.3.2. Recall that by rewriting the orbits using binary expansion we obtained a shift mechanism for the Baker transformation. The Baker transformation also has the property that rational angles will eventually show periodic behaviour [23]. For example the angle $1/3$, with binary expansion $0.1010101\dots$ has a period-two orbit:

$$0.1010101\dots \mapsto 0.0101010\dots \mapsto 0.1010101\dots \mapsto \dots$$

All these properties of the Baker transformation will extend to the field lines of J_0 and thus the angle doubling of the field lines will also show sensitive dependence on initial values. Since we can extend the field lines to J_0 , we conclude that the properties of the field line extend to J_0 .

A lot of the dynamics of J_0 is made visible by using field lines. One could use the dynamics of field lines to prove that the iterated preimages are dense in J_0 , which originally follows from corollary 3.2.2; this is done in the example below.

Example: preimages are dense in J_0

We will prove by making use of the dynamics of field lines that $\forall z_0 \in J_0$, $\{z \in \mathbb{C} \mid f_0^k(z) = z_0, k = 0, 1, 2, \dots\}$ is dense in J_0 .

Take $\alpha = 0.a_0a_1a_2\dots$ with $a_i \in \{0, 1\}$. We have that $B : 0.a_0a_1a_2\dots \rightarrow 0.a_1a_2a_3\dots$. There is a one-to-one correspondence between the boundary of J_0 and the field lines. We need to prove that the

backward iterated orbit for the angle, $d = 0.d_0d_1d_2\dots$, of a given field line is dense in the interval $[0, 1)$. The backwards orbit of the field line d is given by $C = \{c \in [0, 1) \mid B^k(c) = d \text{ } k = 0, 1, 2, \dots\}$. Take an $a \in [0, 1)$, with $a = 0.a_0a_1a_2\dots$. Then there exist a $c \in C$ with $c = 0.a_0a_1a_2\dots a_ma_d0d_1d_2\dots$ where m is smaller than the length of a , thus we can get arbitrarily close to any point in $[0, 1)$.

Böttcher-theorem

We have seen that by using equipotential curves and field lines we can come to understand the dynamics of z^2 . We will now find a conjugacy between z^2 and $z^2 + c$ such that we can extend the field lines as well as the equipotentials curves to $z^2 + c$ and which will lead to the dynamics of J_c . This conjugacy follows from the Böttcher-theorem, which we will be treating next, but will not be defined in complete $\mathbb{C} \setminus K_c$. However for certain cases we will be able to extend this map to complete $\mathbb{C} \setminus K_c$.

The Böttcher-theorem gives us a conjugacy around a superattractive fixed point. We will first prove the statement for a complex polynomial $f(z) = z^k + a_{k+1}z^{k+1} + \dots$ with $k \geq 2$, which has a superattractive fixed point at $z = 0$.

Theorem 3.2.3 (Böttcher) *Take a complex analytic polynomial $f : \mathbb{C} \rightarrow \mathbb{C}$ given by $f(z) = z^k + a_{k+1}z^{k+1} + \dots$ with $k \geq 2$. Then there exists a holomorphic map $\hat{\phi} : \mathbb{D}_r \rightarrow \mathbb{D}$ with $\hat{\phi}(0), \hat{\phi}'(0) = 1$ such that $\hat{\phi} \circ f(z) = (z^k \circ \hat{\phi}(z))$ holds near the origin. Furthermore we can give an explicit form for $\hat{\phi}$*

$$\hat{\phi}(z) = \lim_{n \rightarrow \infty} (f^n(z))^{\frac{1}{k^n}}.$$

Where $\hat{\phi}$ is referred to as the Böttcher map.

Proof. For r sufficiently small we can assume that

- f is complex analytic in \mathbb{D}_r .
- $\text{Cl}(f(\mathbb{D}_r)) \subset \mathbb{D}_r$.
- $\forall z \in \mathbb{D}_r, \lim_{n \rightarrow \infty} f^n(z) \rightarrow 0$.
- 0 is the only critical point of f in \mathbb{D}_r .
- $f(z) \neq 0$ if $z \in \mathbb{D}_r \setminus \{0\}$.

Since we have that $f : \mathbb{D}_r \rightarrow \mathbb{D}_r$ is a map of degree at least k , the function given by $f(z)^{\frac{1}{k}}$ will also be complex analytic. Observe that this function is unique up to a k th root of one.

Define a sequence of maps $\hat{\phi}_n : \mathbb{D}_r \rightarrow \mathbb{C}$ with $n = 1, 2, \dots$ given by

$$\hat{\phi}_n(z) = (f^n(z))^{\frac{1}{k^n}} \text{ with } \hat{\phi}_0(z) = z.$$

Note that $\hat{\phi}'_n(0) = 1$.

Let us first assume that $\hat{\phi}_n$ converges uniformly and define $\hat{\phi} = \lim_{n \rightarrow \infty} \hat{\phi}_n$. Then by definition of the $\hat{\phi}_n$ we have the following property:

$$\hat{\phi} \circ f(z) = \lim_{n \rightarrow \infty} (f^n(f(z)))^{\frac{1}{k^n}} = (\hat{\phi}(z))^k.$$

Thus we have verified that this $\hat{\phi}$ satisfies the desired condition. However we will still need to prove that for $n \rightarrow \infty$ the given $\hat{\phi}_n$ converges uniformly in \mathbb{D} .

Let us define $H : \mathbb{D}_r \rightarrow \mathbb{C}$ as

$$H(z) = \frac{\hat{\phi}_1(z)}{z}, \quad H(0) = 1.$$

$H(z)$ is analytic and $H(z) \neq 0$. Rewriting $\hat{\phi}_1(z) = zH(z)$ we have that

$$\begin{aligned} \frac{\hat{\phi}_{i+1}(z)}{\hat{\phi}_i(z)} &= \frac{(f^{i+1}(z))^{\frac{1}{k^{i+1}}}}{(f^i(z))^{\frac{1}{k^i}}} = \left(\frac{f(f^i(z))^{\frac{1}{k}}}{f^i(z)} \right)^{\frac{1}{k^i}} \\ &= \left(\frac{\hat{\phi}_1(f^i(z))}{f^i(z)} \right)^{\frac{1}{k^i}} = (H(f^i(z)))^{\frac{1}{k^i}}. \end{aligned}$$

Applying this principle multiple times we obtain

$$\phi_{n+1} = z \prod_{i=0}^n \frac{\phi_{i+1}(z)}{\phi_i(z)} = z \prod_{i=0}^n (H(f^i(z)))^{\frac{1}{k^i}}.$$

Finally we obtain

$$\log \left(\prod_{i=0}^n \frac{\hat{\phi}_{i+1}(z)}{\hat{\phi}_i(z)} \right) = \log \left(\frac{\hat{\phi}_{n+1}(z)}{z} \right) = \sum_{i=0}^n \frac{1}{k^i} \log((H(f^i(z))))). \quad (3.2)$$

Since $\text{Cl}(f(\mathbb{D}_r)) \subset \mathbb{D}_r$, it follows that $f^i(z) \in \mathbb{D}_r$ for $z \in \mathbb{D}_r$, $i = 1, 2, \dots$ thus equation 3.2 is uniformly bounded. Hence the convergence of $\hat{\phi}_n$ is uniform on \mathbb{D}_r . \square

The Böttcher-theorem has an important relation to all complex polynomials with a superattractive fixed point (and degree greater than two), since by a transformation we can move the superattractive fixed point to zero, i.e. for a $f : \mathbb{C} \rightarrow \mathbb{C}$ we can find a bijective map $\hat{z} : S \rightarrow \mathbb{D}_r$ with $S \subset \mathbb{C}$, such that for a superattractive fixed point p we have that $\hat{z}(p) = 0$. Recall that all polynomials have a superattractive fixed point since infinity is a superattractive fixed point. Define the transform $z(\zeta) = 1/\zeta$, and the function $F = z \circ f \circ z^{-1}$, where f is any monic complex polynomial. We have that

$$F(\zeta) = \frac{1}{f(1/\zeta)}.$$

Then it follows that $F(\zeta)$ has a superattractive fixed point at $\zeta = 0$. Thus the corresponding Böttcher map for a $|\zeta|$ chosen 'small enough' will be given by

$$\hat{\phi}(\zeta) = \lim_{n \rightarrow \infty} (F^n(\zeta))^{\frac{1}{k^n}} \in \mathbb{D}.$$

Note that since f is monic $\hat{\phi}'(0) = 1$.

In many cases it is more convenient to use the Böttcher map corresponding to the reciprocal given by

$$\phi(z) = \frac{1}{\hat{\phi}(1/z)} = \lim_{n \rightarrow \infty} (f^n(z))^{\frac{1}{k^n}} \in \mathbb{C} \setminus \overline{\mathbb{D}}.$$

Thus we have a superattractive fixed point at infinity. Henceforth refer to the map ϕ corresponding to $\mathbb{C} \setminus \overline{\mathbb{D}}$ as the Böttcher map.

Corollary 3.2.4 *The Böttcher-theorem extends to any complex analytic polynomial $f : \hat{\mathbb{C}} \rightarrow \hat{\mathbb{C}}$.*

Remark: What happens if several superattractive fixed points occur? For the case $n = 2$ it is rather convenient that there can exist at most two superattractive fixed points: at infinity and at $z = 0$. The second will always be contained inside the $\text{Int}(F_c)$ if the Julia set is connected (this will be proved in theorem 3.2). This actually leads to the dynamics of the filled Julia set. We will not investigate the dynamics of K_c but refer to [26]. However in the cases that $n > 2$ one indeed obtains as one would expect that the conjugation $z \mapsto z^n$ holds in every superattractive fixed point.

Extending the Böttcher map

We would like to extend this local mapping to a complex analytic mapping $\phi : \mathbb{C} \setminus K \rightarrow \mathbb{C} \setminus \overline{\mathbb{D}}$. This is not always possible since we are dealing with an expression of the form:

$$z \mapsto (\phi(f^n(z)))^{\frac{1}{n}}.$$

This may give problems since a given n th-root of a complex function is not always uniquely defined. For example, if two or more points get mapped onto the superattractive fixed point at infinity or in the case we are dealing with disconnected sets. However in the absolute sense ϕ will always be uniquely defined.

Corollary 3.2.5 (Extension of $|\phi|$) *If $f : \hat{\mathbb{C}} \rightarrow \hat{\mathbb{C}}$ has a superattracting fixed point p , then the continuous function $|\phi| : \mathbb{C} \setminus K_f \rightarrow [1, \infty)$ as defined in theorem 3.2.3 will satisfy the identity $|\phi(f(z))| = |\phi(z)|^n$. We will have that $|\phi(z)|$ is (real) analytic, perhaps with the exception at the preimages of the point p , where it takes the values zero.*

The proof follows immediately from theorem 3.2.3 [26]. \square

Before we can continue we will need a definition from complex analysis.

Definition 3.2.10 (Conformal isomorphism or Biholomorphism) *A conformal isomorphism or biholomorphism f is a mapping $f : U \rightarrow V$ with $U, V \subset \hat{\mathbb{C}}$, which is a complex analytic (or holomorphic) bijective function, with an inverse which is also complex analytic.*

Under certain circumstances we can even extend ϕ^{-1} to the complete $\mathbb{C} \setminus K_f$.

Theorem 3.2.4 (Critical points in the basin) *In the case that there are no critical points contained inside $\mathbb{C} \setminus K_f$, then we have that ϕ^{-1} extends to a conformal isomorphism*

$$\phi^{-1} : \mathbb{C} \setminus \overline{\mathbb{D}} \rightarrow \mathbb{C} \setminus K_f.$$

In the cases that at least one critical point is contained in $\mathbb{C} \setminus K_f$ we have that there exists a smallest number $r > 1$ such that ϕ^{-1} near infinity extends to a conformal isomorphism

$$\phi^{-1} : \mathbb{C} \setminus \overline{\mathbb{D}}_r \rightarrow U \subset \mathbb{C} \setminus K_f$$

where U is an open neighbourhood of infinity. Moreover we have that ∂U is a compact subset which contains at least one critical point of f .

We will omit the proof and refer to [26] in which a proof can be found for the complement spaces; the proof of the theorem above is equivalent.

Remark: Observe that theorem 3.2.4 implies that if the critical orbit is bounded $\mathbb{C} \setminus K_f$ will be pathwise connected. Furthermore one can prove that for any complex polynomial f $\mathbb{C} \setminus K_f$ is pathwise connected, the proof for the family of polynomials generated by f_c can be found in Appendix E.

Summarizing the result for f_c , we have that f_c has a superattractive fixed point at infinity which according to the Böttcher-theorem means, that at infinity there exists a conjugation $(\phi_c \circ f_c \circ \phi_c^{-1})(z) = z^2$, where ϕ_c is the Böttcher-map of f_c . Furthermore we can extend the Böttcher map to the complete $\mathbb{C} \setminus K_c$ if $\mathbb{C} \setminus K_c$ contains no critical points. Thus for the case K_c we can just check if the orbit corresponding to zero is bounded.

We will now use the Böttcher-theorem to find the equipotential curves and field lines. Let us take a classical approach and first define:

Definition 3.2.11 (Green's function of K_f) *The Green's function of K_f is a continuous map $G : \mathbb{C} \rightarrow \mathbb{R}$ defined by*

$$G(z) = \begin{cases} \log |\phi(z)| > 0 & \text{for } z \in \mathbb{C} \setminus K_f, \\ 0 & \text{for } z \in K_f \end{cases}$$

Observe the identity for a polynomial f with $\deg(f) = k$

$$G(f(z)) = kG(z).$$

We now specifically investigate K_c . Hence define the Green function of K_c by G_c . The Green function is closely related to the equipotential curves. For the z^2 case we had that the equipotential curve corresponding to a constant $a \in [1, \infty)$ is given by $\{r \mid \log r = a\}$. Similarly we can define for $z^2 + c$ the equipotential curve corresponding to $a \in [1, \infty)$ by $G_c^{-1}(a) = \{z \mid G_c(z) = a\}$, furthermore these are uniquely defined. Similar we have that a field line of K_c for an $\alpha \in [0, 2\pi)$ is given by $\{z \mid \arg(\phi_c(z)) = \alpha\}$; field lines don't have to be uniquely defined (see theorem 3.2.4). We also don't have the guarantee that field lines will extend to the boundary of K_c for all c 's. It has however been proven that field lines with rational angles will land on connected Julia sets.

Theorem 3.2.5 *For a connected Julia sets all rational field lines will land.*

For a proof we refer to [26].

Numerical generation of equipotential curves and field lines

Using the Böttcher-map as given in theorem 3.2.3 for the calculation of the equipotential curves and field lines will quite often result in round-off errors since we need to calculate expressions of the form

$$\lim_{n \rightarrow \infty} \frac{1}{2^n} \log |f_c^n(z)|, \quad \lim_{n \rightarrow \infty} \frac{1}{2^n} \arg(f_c^n(z)).$$

However, by rewriting we obtain

$$f_c^n(z) = z \cdot \prod_{k=1}^n \frac{f_c^k(z)}{f_c^{k-1}(z)}$$

and using that $f_c^n(z) = (f_c^{n-1}(z))^2 + c$ we get a rapidly converging series for the equipotential curves given by

$$\begin{aligned} G_c^{-1}(a) &= \{z \mid \log |\phi_c(z)| = a\} \\ &= \{z \mid \lim_{n \rightarrow \infty} \log |z| + \sum_{i=0}^n \frac{1}{2^i} \log \left| 1 + \frac{c}{f_c^{i-1}(z)} \right| = a\}. \end{aligned}$$

For the field lines we have

$$\{z \mid \arg(\phi_c(z)) = \alpha\} = \{z \mid \lim_{n \rightarrow \infty} \arg(z) + \sum_{i=0}^n \frac{1}{2^i} \arg \left(1 + \frac{c}{f_c^{i-1}(z)} \right) = \alpha\}.$$

When we give a numerical generation of equipotential curves and field lines it will be quite hard to just draw the equipotential curve or field line for a single constant. There exist methods which can do this, we refer to [23]. We will be using a simpler method: we divide \mathbb{C} into sectors where we will give the corresponding equipotential curves, field lines the same colour if their constant, a , α , respectively is in a certain interval.

By numerical computation one obtains figure 3.10 for K_{-1} .

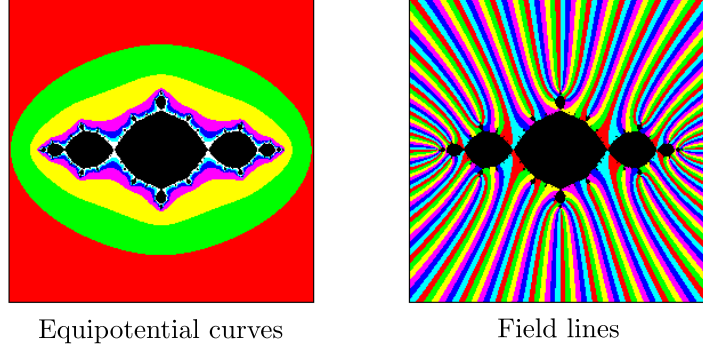


Figure 3.10: Equipotential curves and field lines for K_{-1} .

We make two important observations: equipotential curves encircle the connected Julia set and field lines seem to extend to the boundary of the filled Julia set.

The visualizations of field lines and equipotential curves in figure 3.10 are not so clear. However, there is a representation of equipotential curves and field lines which fuses both together in one plot, such that we get a better understanding of the dynamics of Julia sets.

Binary decomposition

Binary decomposition of $\mathbb{C} \setminus K$ decomposes the $\mathbb{C} \setminus K$ into parts and assigns binary labels to each part. We will only be treating the case for $\mathbb{C} \setminus K_c$.

We first investigate $\mathbb{C} \setminus K_0$. We subdivide $\mathbb{C} \setminus K_0$ with respect to the equipotential curves:

$$L_0^k = \{z \in \mathbb{C} | 2^{k-1} < G_0(z) \leq 2^k\}.$$

We call these sets the k th-level set. By dividing the level sets again with respect to the argument we can describe the field lines. Starting decomposing at L_0^k with an arbitrarily chosen k , we consider rewriting the argument in binary expansion. First define $R_0(z) := \arg(\phi_0(z))/(2\pi)$. We write the binary expansion of $R_0(z)$ as $(R_0(z))_2$. Now subdivide the L_0^k into two sets

$$\begin{aligned} L_0^k(0) &= \{z \in L_0^k | 0 < (R_0(z))_2 < 0.1\}, \\ L_0^k(1) &= \{z \in L_0^k | 0.1 < (R_0(z))_2 < 1\}. \end{aligned}$$

These are the stage-1 cells of the level set L_0^k , with an associated label 0 and 1, respectively. Now we define the stage-2 cells, $L_0^k(00), L_0^k(01), L_0^k(10), L_0^k(11)$ which are given by

$$\begin{aligned} L_0^k(00) &= \{z \in L_0^k | 0 < (R_0(z))_2 < 0.01\}, \\ L_0^k(01) &= \{z \in L_0^k | 0.01 < (R_0(z))_2 < 0.10\}, \\ L_0^k(10) &= \{z \in L_0^k | 0.10 < (R_0(z))_2 < 0.11\}, \\ L_0^k(11) &= \{z \in L_0^k | 0.11 < (R_0(z))_2 < 1\}. \end{aligned}$$

These are called stage-2 cells of the level set L_0^k , with an associated label, 00, 01, 10, 11, respectively. By construction we have that $L_0^k(00) \cup L_0^k(01) = L_0^k(0)$ and $L_0^k(10) \cup L_0^k(11) = L_0^k(1)$. Continuing dividing each cell into two parts we can define eight stage-3 cells which divide L_0^k into equal parts. Extending the previous statements to stage- n cells:

$$L_0^k(a_n a_{n-1} \dots a_0) = \{z \in L_0^k | 0.a_n a_{n-1} \dots a_0 < (R_0(z))_2 < 0.a_n a_{n-1} \dots a_0 + (1/2^n)_2\},$$

with the property

$$L_0^k(a_n a_{n-1} \dots a_0) = L_0^k(a_n a_{n-1} \dots a_0 0) \cup L_0^k(a_n a_{n-1} \dots a_0 1).$$

We can now decompose $\mathbb{C} \setminus K_0$, we do this by colouring the stage- n cells of each level set in alternating colour, see figure 3.11.

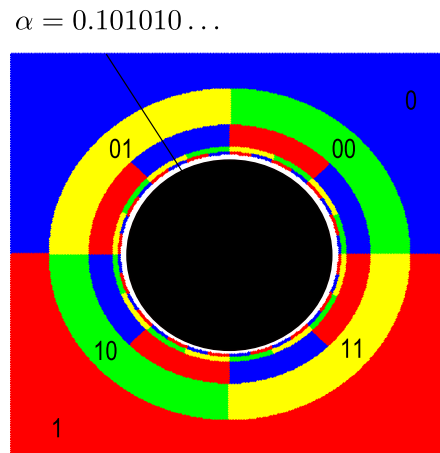


Figure 3.11: Binary decomposition of $\mathbb{C} \setminus K_0$. Here green and blue correspond to 0 and yellow and red correspond to 1.

In figure 3.11 we have coloured each stage- n cell with a 0 at the end of their label green and blue, and each stage- n cell with a 1 at the end of their label yellow and red. The field lines can now literally be read off from the binary decomposition. Just write the $R_0(z) = cst$ in binary expansion and draw a line through the labels corresponding to the binary expansion. In the picture above we have drawn the field line corresponding to $R_0(z) = 1/3$ which can be written in binary expansion as $0.1010101\dots$

Generalizing the concept to every c we obtain that

$$L_c^k = \{z \in \mathbb{C} | 2^{k-1} < G_c(z) \leq 2^k\}.$$

The stage- n cells are then given by

$$L_c^k(a_n a_{n-1} \dots a_0) = \{z \in L_c^k | 0.a_n a_{n-1} \dots a_0 < (\arg(R_c(z)))_2 < 0.a_n a_{n-1} \dots a_0 + (1/2^n)_2\},$$

with the property that

$$L_c^k(a_n a_{n-1} \dots a_0) = L_c^k(a_n a_{n-1} \dots a_0 0) \cup L_c^k(a_n a_{n-1} \dots a_0 1).$$

From now on when writing the angle of a rational field we just give the value of $R_0(z)$ instead of writing the angle in terms of radials.

3.2.6 Dynamics of two Julia sets investigated

We now explore the dynamics of two connected Julia sets by making use of equipotential curves and field lines: a Julia set with a repelling fixed point and a Julia set with a parabolic fixed point. For both Julia sets it has been checked that the Böttcher map can be extended to complete $\mathbb{C} \setminus K_c$, i.e. the critical orbit is bounded.

Example: J_{-1} , repelling fixed point

The corresponding mapping of J_{-1} is given by $z \rightarrow z^2 - 1$. This specific Julia set is symmetric under reflection in the imaginary and real axis. This symmetry in the imaginary axis follows from the fact that $|f_{-1}^n(\bar{z})| = |f_{-1}^n(z)|$. Hence if the complex conjugate converges or diverges uniformly, the z will also converge or diverge uniformly. Similarly one can prove symmetry under reflection in the real axis. The mapping has two fixed points given by

$$z_1 = \frac{1 + \sqrt{5}}{2} \quad \text{and} \quad z_2 = \frac{1 - \sqrt{5}}{2}.$$

Since $|1 \pm \sqrt{5}| > 1$ both points are repelling and thus $z_1, z_2 \in J_{-1}$. Theorem 18.11 in [26] states that repelling and parabolic periodic points are landing points, thus we can extend a field line to z_1 and z_2 . Using this result we must have that the field lines under angle doubling, $\alpha \rightarrow 2\alpha \pmod{1}$, must still land at the fixed points. One has that $\alpha_1 = 0$ satisfies this condition, since it is mapped onto itself. However there will only exist one such point. Since we have nowhere excluded the possibility that two or more field lines can land at the same fixed point, we may hypothesize that two field lines land at the second fixed point. The angles corresponding to $\alpha_{21} = \frac{1}{3}$ and $\alpha_{22} = \frac{2}{3}$ satisfy this condition. Let us verify the result numerically by a binary decomposition of $\mathbb{C} \setminus K_{-1}$.

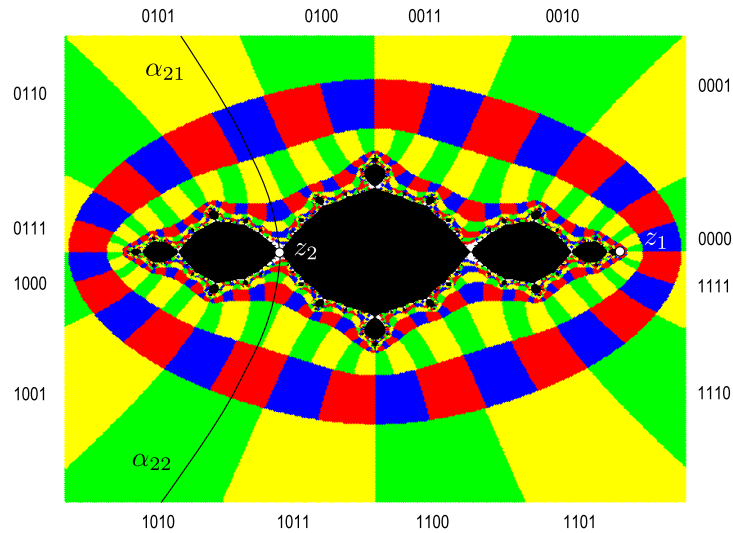


Figure 3.12: Binary decomposition of J_{-1} with fixed point z_1 and z_2 . We have also drawn the corresponding field lines to z_2 which are $\alpha_{21} = \frac{1}{3}$ and $\alpha_{22} = \frac{2}{3}$. Here green and blue correspond to 0 and yellow and red correspond to 1.

We see that $\alpha_1 = 0$ ends at z_1 . The binary expansions for $\alpha_{21} = 0.010101010\dots$ and $\alpha_{22} = 0.101010\dots$, indeed the corresponding field lines land at the fixed point z_2 .

Example: $J_{-0.4818\dots-0.5317\dots i}$, **parabolic fixed point**

The corresponding mapping is given by $z \rightarrow z^2 - 0.4818\dots - 0.5317\dots i$. This Julia set is only symmetric by reflection in the line $\text{Re}(z) = \text{Im}(z)$ as are all maps of the form $z \mapsto z^2 + c$. This mapping has two fixed points given by

$$z_1 \approx 1.4045 + 0.2939i \quad \text{and} \quad z_2 \approx -0.4045 - 0.2939i.$$

Furthermore z_2 corresponds to a parabolic fixed point with rational angle given by $4/5$. There is a relation between the rational angle of the parabolic fixed point and the corresponding field lines. To see this let us generate the binary decomposition of the Julia set.

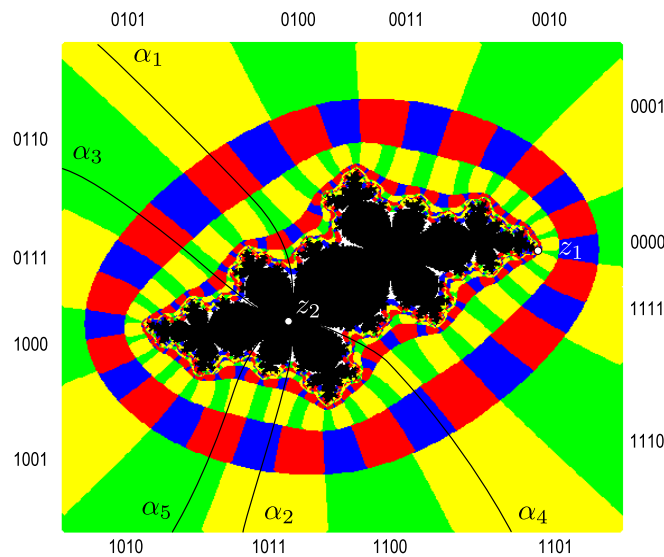


Figure 3.13: Binary decomposition of $J_{-0.4818\dots-0.5317\dots i}$, with fixed point z_1 and parabolic fixed point z_2 . Observe that five field lines corresponding to $\{\alpha_1, \alpha_2, \alpha_3, \alpha_4, \alpha_5\}$ meet at the parabolic fixed point z_2 .

For Julia sets containing parabolic periodic orbits it is quite hard to generate satisfactory graphical results. The petals that we see near to the fixed point z_2 are only connected to the point z_2 and not to each other as the figure might suggest. This also corresponds with the earlier results since we proved that parabolic periodic orbits must be contained in the Julia set. Thus the field lines are located in between these petals and eventually hit the parabolic fixed point.

We observe that five field lines are connected to the parabolic fixed point at z_2 , moreover these form a periodic five orbit, $\{\alpha_1, \alpha_2, \alpha_3, \alpha_4, \alpha_5\}$, under angle doubling. We verify this by reading the binary expansion $\alpha_1 = 0.0101101\dots$ from figure 3.13 and checking that this corresponds to the field lines $\{\alpha_1, \alpha_2, \alpha_3, \alpha_4, \alpha_5\}$. The orbit of α_1 is given by

$$0.0101101\dots \mapsto 0.1011010\dots \mapsto 0.0110101\dots \mapsto 0.110101\dots \mapsto 0.101011\dots \mapsto 0.0101101\dots$$

So how is this related to the rational angle of the fixed point? Well the rational angle is given by $4/5$; observe that the denominator is equal to the period of the orbit of the field lines of the parabolic fixed point. One could perhaps call this a coincidence, but one can indeed prove this statement. This is closely related to the amount of petals which are attached to the parabolic fixed point, for we observe that this number is equal to the number of field lines [26].

Remark: Note that we have not drawn the stage-1, 2, 3 cells in figure 3.12 and 3.13. The lower the stage of a cell the less indication we have of the direction of the field lines. Furthermore as we get closer to the boundary the colour coding will get unclearer. This will mean that we can approximately only use the first four stages, to determine the direction of the field line. If we would start with a stage-1, 2, 3 the stages are too low to give an indication where the field lines goes. By starting already at stage-4 cells we can overcome this problem.

3.2.7 Julia sets: Connected sets and Cantor sets

This section will be devoted to the following theorem with proof.

Theorem 3.2.6 (Connected J_f , $K_f \iff$ Bounded critical orbit) *Take f a complex polynomial with $\deg(f) \geq 2$. If the filled Julia set contains all the finite critical points of f , then both K_f and J_f are connected.*

If however one critical point belongs to $\mathbb{C} \setminus K_f$, then we will have that K_f and J_f exist out of infinitely many connected components, i.e a Cantor set.

This theorem states that J_f can be divided into connected and Cantor sets and gives us a method to check to which family it belongs. Theorem 3.2.4 will play an important role in the proof of theorem 3.2.6, presented below.

Proof. Let us first assume that there are no other critical points other than ∞ in $\mathbb{C} \setminus K_f \rightarrow \mathbb{C}$. Then according to 3.2.4 we must have that there exists a conformal isomorphism $\phi : \mathbb{C} \setminus K_f \rightarrow \mathbb{C} \setminus \overline{\mathbb{D}}$. Now we are going to approximate the Julia set by mapping annuli under ϕ^{-1} . Let us define the annulus by

$$\mathbb{A}_{1+\epsilon} = \{z \in \mathbb{C}; 1 < |z| < 1 + \epsilon\}.$$

By definition of ϕ^{-1} we will have that it maps connected sets onto connected sets, hence $\phi^{-1}(A_{1+\epsilon})$ is connected. We will have that the closure, $\overline{\phi^{-1}(A_{1+\epsilon})}$ is compact and contains J_f . Hence

$$J = \bigcap_{\epsilon > 0} \overline{\phi^{-1}(A_{1+\epsilon})}$$

which is also connected. It follows that K_f is also connected since $\partial K_f = J_f$.

Now suppose that there is at least one critical point inside $\mathbb{C} \setminus K_f$. We then have that there exists an $r > 1$ such that

$$\phi^{-1} : \mathbb{C} \setminus \mathbb{D}_r \rightarrow U \subset \mathbb{C} \setminus K_f.$$

We prove that \overline{U} divides the plane into two (or more) pieces which contain the Julia set. Furthermore we can divide these two pieces infinitely many times in such a way that in each piece a part of the Julia set will be contained and such that in the union of all these pieces the complete Julia set will be contained.

Let c be the critical point, according 3.2.4 we have that it lies on ∂U . The critical value corresponding to the critical point is given by $v = f(c)$. We have that $v \in U$, and the corresponding point on the unit disk lies $|\phi(v)| > r^2 > r$ removed from the origin. Then we have a corresponding field line to the point v under ϕ on the unit disk, let us call this field line R . We will call the field line corresponding to v in $\mathbb{C} \setminus K_f$ R' .

We now have that $f^{-1}(R') \cap U$ consists out of at least 2 components since $\deg(f) \geq 2$. These components correspond to two components in $\mathbb{C} \setminus \mathbb{D}_r$ which we call R_1 and R_2 ; these are in the field lines of z^d , with $d = \deg(f)$. The corresponding field lines in $\mathbb{C} \setminus K_f$ will then be called R'_1 and R'_2 . We will have that each of these field lines will end at a z which is a solution of $f(z) = v$. Since c is a critical point, at least two field lines must intersect c implying that $R'_1 \cup R'_2 \subset \overline{U}$ will cut the plane into two connected parts V_1 and V_2 , as represented in figure 3.14.

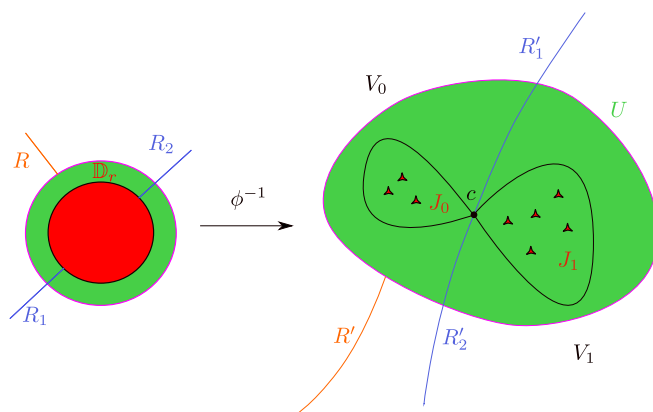


Figure 3.14: Here we have represented the preimages and corresponding images under the mapping $\phi^{-1} : \mathbb{C} \setminus \mathbb{D}_r \rightarrow U \subset K_f$ in the same colour. The field lines R_1 and R_2 are the preimages of R under z^d , with $d = \deg(f)$. The images under ϕ^{-1} of R_1 and R_2 which are R'_1 and R'_2 will divide \mathbb{C} into two parts V_0 and V_1 . In doing so they will also divide the Julia set into two parts: J_0 and J_1 .

Now since $f^{-1}(R') = R'_1 \cup R'_2$ we have that $f(V_0)$ and $f(V_1)$ must contain all the points in $\hat{\mathbb{C}}$ with the possible exception of R' . It can be proven in a straightforward way that $f(V_0)$ and $f(V_1)$ are open sets such that if $\tilde{z} \notin V_j$ with $j = 1, 2$ then $f(\tilde{z}) \in R'$ [26]. Since $\mathbb{C} \setminus R'$ is connected we have the following

$$f(V_j) \supset \mathbb{C} \setminus R' \supset K \quad j = 1, 2$$

Let us divide J into two disjoint sets, by defining $J_j = J \cap V_j$ for $j = 1, 2$. It holds that $f(J_j) = J$. Furthermore we have that $J_0 \cap J_1 = \emptyset$. We can now continue to split each of these sets into smaller sets by $J_{j_0} = J_j \cap f^{-1}(J_0)$ and $J_{j_1} = J_j \cap f^{-1}(J_1)$. These sets are non-empty since $f(J_{j_0}) = f(J_j \cap f^{-1}(J_0)) = J \cap J_0 = J_0$. Generalizing this gives $f(J_{ij}) = J_j$. Continuing this splitting inductively we have 2^{p+1} disjoint components

$$J_{j_0 \dots j_p} = J_{j_0} \cap f^{-1}(J_{j_1}) \cap \dots \cap f^{-p}(J_{j_p}),$$

with $f(J_{j_0 \dots j_p}) = J_{j_1 \dots j_p}$. Similarly for an infinite binary sequence we obtain $J_{j_0 j_1 \dots}$ which is the intersection of the nested sequence

$$J_{j_0} \supset J_{j_0 j_1} \supset \dots$$

Each of these elements is non-empty and compact, and we have that the union of all these infinite disjoint sets will be equal to J_f . Hence J_f is conformally isomorphic to a Cantor set, from which it immediately follows the K_f is also conformally isomorphic to a Cantor set. \square

For the cases $z^2 + c$ theorem 3.2.6 implies that we can just check if the orbit at $z_0 = 0$ is bounded. We have that

- if $0 \in K_c$, the set K_c is connected.
- if $0 \notin K_c$, the set K_c is conformally isomorphic to a Cantor set.

3.3 Mandelbrot set

The Mandelbrot set arose from the idea to create a certain ordering in the Julia sets. As we have already seen, we can divide the Julia sets into two families: connected sets and Cantor sets. This will

lead us to the definition of the Mandelbrot set.

Definition 3.3.1 (Mandelbrot set of J_c) *The Mandelbrot set corresponding to J_c is given by*

$$M = \{c \in \hat{\mathbb{C}} \mid J_c \text{ is connected}\}.$$

When referring to the Mandelbrot set we will always be referring to the Mandelbrot set of J_c .

It can be pretty difficult to directly check if a J_c is connected, however we have already seen in theorem 3.2.6 that a Julia set is connected if and only if the critical orbit is bounded. This leads us to the following equivalent definition of the Mandelbrot set.

Equivalent Definition 3.3.1 *The Mandelbrot set is given by*

$$M = \{c \in \hat{\mathbb{C}} \mid 0 \mapsto c \mapsto c^2 + c \mapsto \dots \text{ is bounded}\}.$$

From the investigation of the Julia sets we have seen that the critical orbit corresponding to $|c| > 2$ must diverge to infinity (see proposition 3.2.5). Using this property together with equivalent definition 3.3.1 one can numerically compute the Mandelbrot set, see figure 3.15.

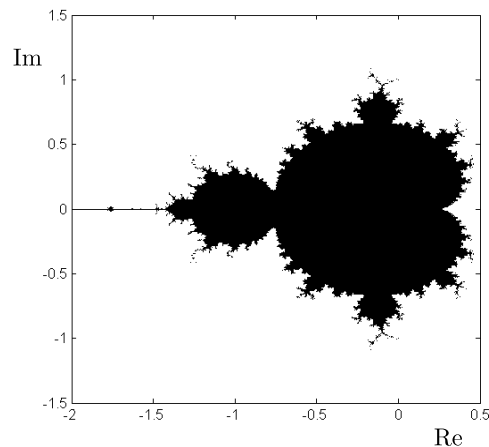


Figure 3.15: The Mandelbrot set for the family J_c

Remark: The Mandelbrot sets can be defined for any rational function as the set corresponding to the parameter space of the connected sets, see [5]. We have restricted ourselves to J_c .

3.3.1 Numerical investigation of ∂M

The Mandelbrot set is in a total different class as Julia sets. The Mandelbrot set has a non-empty interior which is bordered by an intricate boundary with infinitely many different shapes. For starters we have magnified some parts of ∂M , see figure 3.16.

A striking feature of the Mandelbrot set is that small buds are lined up to a big heart shaped region, also called the main cardioid. Furthermore as we zoom in on these smaller buds we see even smaller buds appearing.

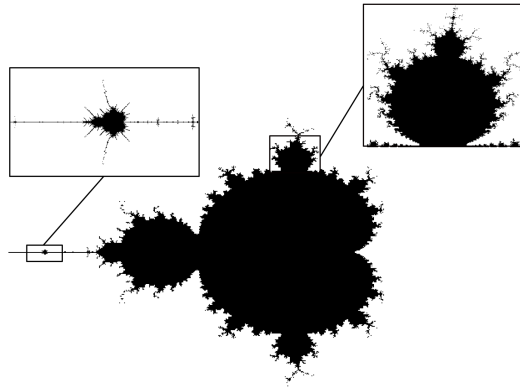


Figure 3.16: The Mandelbrot set with two enlargements. Right a bud and left a baby Mandelbrot.

Another interesting feature are the smaller Mandelbrot like sets which appear under magnification, see figure 3.16. This property is seen at a lot of points along the boundary of the Mandelbrot set, another example is displayed in figure 3.17.

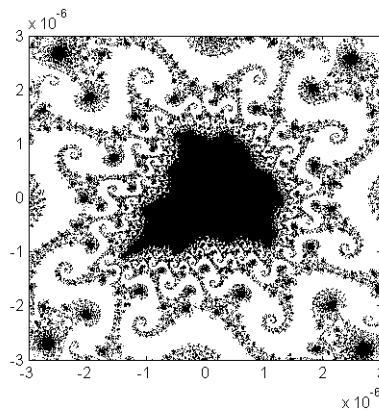


Figure 3.17: Enlargement of the Mandelbrot set at $c = -0.7454285 + 0.1130089i$.

All these features make the boundary so complex that ∂M has boxcounting dimension equal to 2.

There exists many points on the boundary of the Mandelbrot set which under magnification lead to stunning pictures, however we will end our discussion here and refer to the reader for more figures to [31].

3.3.2 External dynamics

Of course it isn't sufficient to just investigate the dynamics by zooming on the boundary of the Mandelbrot, hence we shall once again use equipotential curves and field lines to understand the dynamics. The equations corresponding to the field lines and equipotential curves will now be defined slightly differently, for a point in \mathbb{C} won't correspond to an initial value of an orbit, as was the case with J_c ; with the Mandelbrot set we have that each orbit will start at the same initial point, at $z_0 = 0$, and the parameter c , which corresponds to a point in the parameter plane, will change for the map $z \rightarrow z^2 + c$.

Conformal isomorphism for $\mathbb{C} \setminus M$

We want a conformal isomorphism $\psi : \mathbb{C} \setminus M \rightarrow \mathbb{C} \setminus \overline{\mathbb{D}}$. Since $\mathbb{C} \setminus M$ corresponds to the disconnected Julia sets we have a conformal isomorphism $\phi_c : \mathbb{C} \setminus K_c \rightarrow \mathbb{C} \setminus \overline{\mathbb{D}}_r$ for a $r > 1$. If we could extend the ϕ up to c we could define a conjugacy $\phi_c(c)$ which would define a conformal isomorphism for $\mathbb{C} \setminus M$, thus $\psi(c) := \phi_c(c)$.

Theorem 3.3.1 (Existence conformal isomorphism $\psi(c)$) *There exists a conformal isomorphism given by $\psi(c) := \phi_c(c)$ such that*

$$\psi : \mathbb{C} \setminus M \rightarrow \mathbb{C} \setminus \overline{\mathbb{D}}.$$

This proof was given by Douady and Hubbard. A complete proof is rather complicated and long, hence we provide the reader with an outline below and refer for a full proof to [7].

Outline proof. We have by Böttcher's theorem for $c \in \mathbb{C} \setminus M$ the mapping $c \mapsto \phi_c(c) := \psi(c)$ is well-defined. Douady and Hubbard proved that ψ is analytic, proper (the inverse of any compact set is compact) and of degree one. Moreover, if one has a sequence (c_n) which converges to the boundary of M , $c \in \partial M$, then we have that for $n \rightarrow \infty$ that $|\psi(c_n)| = |\phi_{c_n}(c_n)| \rightarrow 1$, i.e. the boundary of M gets mapped onto the unit circle. The injectivity of ϕ will then follow from the fact that it is proper and thus we have that ψ is conformally isomorphic.

Apart from giving us a method to calculate the equipotential curves and field lines, this theorem has a famous corollary:

Corollary 3.3.1 *The Mandelbrot set is connected.*

Proof. Using theorem 3.3.1, we now have that the complement, $\mathbb{C} \setminus M$, is connected i.e. M is connected.

Let us now briefly interrupt the discussion on equipotential curves and field lines to discuss an conjecture which is closely connected to corollary 3.3.1.

Locally connected

It still is an open conjecture whether ψ^{-1} has a continuous extension to the boundary of the unit disk. This would imply that the following open conjecture also holds.

Conjecture 3.3.1 (MLC) *The Mandelbrot set is locally connected.*

Locally connectedness of M means that for every $z \in U \cap M$ with $U \subset \mathbb{C}$ is open, $\exists V \subset U$ with $z \in V$ such that $V \cap M$ is connected. The difficulty is that one cannot use the properties of K_c , since some of the connected K_c are not locally connected. An interesting consequence if one could prove this conjecture is that the interior of M consists out of all f_c with an attracting orbit [15]. Furthermore, one would also have that all field lines could be extended to ∂M . Douady and Hubbard showed that only the rational field lines can be extended to the boundary [35]. As we have mentioned earlier with Julia

sets, the behaviour of irrational field lines is very complicated; the same applies for the Mandelbrot set.

However it is known that Julia sets which belong to periodic points for which $z \mapsto z^2 + c$ has a Cremer point, i.e. a periodic point which belongs to J_c but which is neither repelling nor parabolic [26], are not locally connected and thus have irrational field lines which do not hit the boundary. This result may be a bit hard to comprehend, since rational field lines do hit the boundary. Therefore we will take a brief look at an example created by Carathéodry where a field line doesn't hit the boundary.

Double comb of Carathéodry

The double comb of Carathéodry is displayed in figure 3.18.

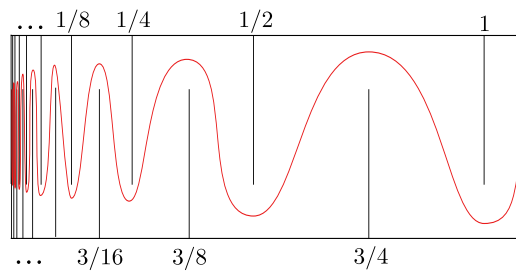


Figure 3.18: The above line segments are placed on $1/2^n$ and the segments below are placed on $3/2^n$ for $n \in \mathbb{Z}_+$. The black comb structures represents the Julia set and the red line is the corresponding field line, which is supposed to land at the left end of the comb. However, due to the increase of line segments it will never hit the end of the comb.

The above line segments are placed on $1/2^n$ and the segments below are placed on $3/2^n$ for $n \in \mathbb{Z}_+$. Now draw a field line through this comb, such that it doesn't touch the teeth of the comb. As we reach close to the left boundary it will need to oscillate quicker and quicker to evade the teeth of the comb. Due to the fact that there are infinitely many teeth of the comb as we reach the left boundary the field line can never reach the left side of the comb.

Numerical generation of equipotential curves and field lines

By making use of the mapping in theorem 3.3.1 we can define a Green's function for the Mandelbrot set.

Definition 3.3.2 (Green's function for M) *The Green function of M is a continuous map $G : \mathbb{C} \rightarrow \mathbb{R}$ defined by*

$$G(z) = \begin{cases} \log |\psi(z)| > 0 & \text{for } z \in \mathbb{C} \setminus M, \\ 0 & \text{for } z \in M \end{cases}$$

Similar to the Julia sets we can make the equations for equipotential curves explicit:

$$\begin{aligned} G^{-1}(a) &= \{c \mid \log |\psi(c)| = a\} \\ &= \{c \mid \lim_{n \rightarrow \infty} \log |c| + \sum_{i=0}^n \frac{1}{2^i} \log \left| 1 + \frac{c}{f_c^{i-1}(c)} \right| = a\} \quad \text{with } a \in [1, \infty). \end{aligned}$$

For the field lines we obtain

$$\{c \mid \arg(\psi(c)) = \alpha\} = \{c \mid \lim_{n \rightarrow \infty} \arg(c) + \sum_{i=0}^n \frac{1}{2^i} \arg \left(1 + \frac{c}{f_c^{i-1}(c)} \right) = \alpha\} \quad \text{with } \alpha \in [0, 2\pi).$$

Once again when writing the angle of a rational field we will just state the angle divided by 2π . Using binary decomposition we visualize the external dynamics in figure 3.19 .

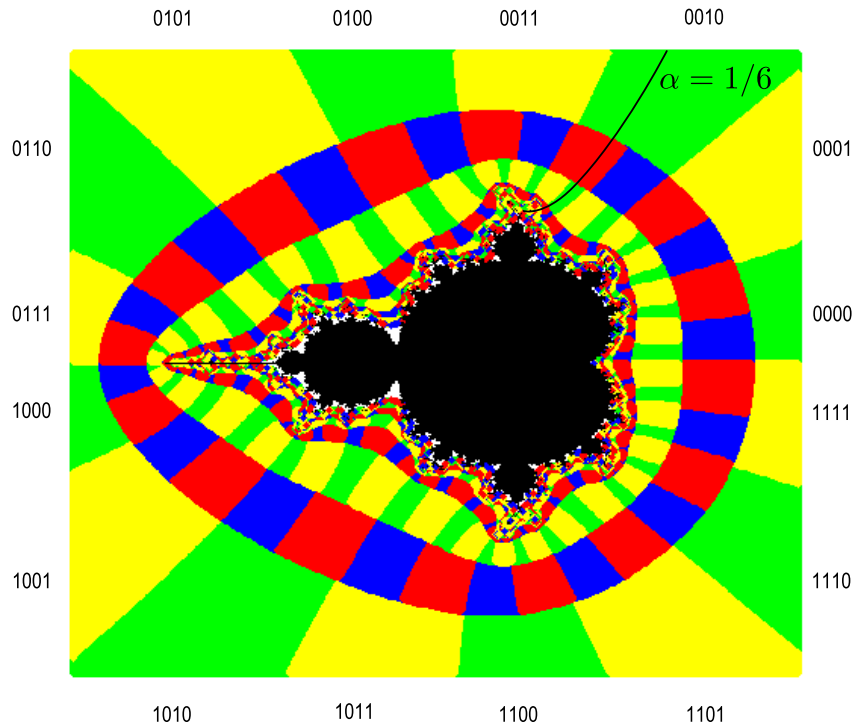


Figure 3.19: Binary decomposition of the Mandelbrot set, we have indicated here the field line at $\alpha = 1/6$. This field line will land at $c = i$. Furthermore the eventually period is at the critical point i is equal to that of the period of α under angle doubling.

One can make some interesting observations if we check where the field lines will land. Let us first investigate angles with even denominator, for example take $\alpha = 1/6$. The corresponding orbit of α in binary expansion is given by

$$0.0010101 \dots \mapsto 0.01010 \dots \mapsto 0.10101 \dots \mapsto 0.01010 \dots \mapsto \dots$$

Thus it eventually tends to a periodic two-cycle. The corresponding field line hits the Mandelbrot set at $c = i$. Let us now take a look at the behaviour of the corresponding critical orbit, i.e. $z_k = z_{k-1}^2 + c$ with $z_0 = i$, which is given by

$$i \mapsto -1 + i \mapsto -i \mapsto -1 + i \mapsto \dots$$

The orbit of the field line and the critical orbit correspond to each other. Furthermore one can obtain the following rule if an orbit becomes periodic after ℓ iterations and the period is equal to m or divides m : the field line will correspond to $\alpha = n/(2^\ell(2^m - 1))$, with $n \in \mathbb{Z}_+$.

As we noted earlier the Mandelbrot set exists out of a number of buds which are connected to the heart-shaped big bud, the main cardioid. Now let us take a look at the corresponding field lines which ‘cut’ these buds off from the main cardioid. For the biggest bud which is connected left to the cardioid one obtains the angles $1/3$ and $2/3$, see figure 3.20. The slightly smaller buds located on the top and bottom of the main cardioid correspond to the angles $1/7$ and $2/7$. One can continue this, and one will indeed obtain an interesting correspondence; namely the two angles corresponding to the field lines which cut of the bud from the main cardioid satisfy $\alpha = n/(2^m - 1)$, where $n, m \in \mathbb{Z}_+$. We can describe these buds much better by investigating the internal dynamics.

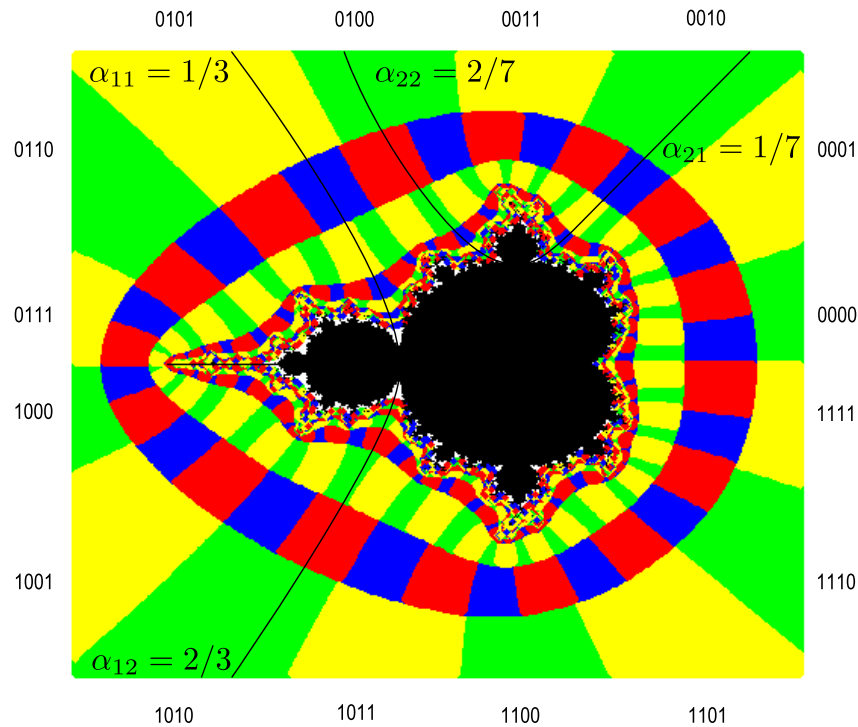


Figure 3.20: Binary decomposition of the Mandelbrot set. Observe that the field lines $\alpha_{11} = 1/3$ and $\alpha_{12} = 2/3$ ‘cut’ the big left bud off from the main cardioid. Similarly we have $\alpha_{21} = 1/7$ and $\alpha_{22} = 2/7$ corresponding to the slightly smaller bud located at the upper part of the cardioid. Note also that these field lines correspond to the relation $\alpha = n/(2^m - 1)$, where $n, m \in \mathbb{Z}_+$.

3.3.3 Internal dynamics

Instead of investigating the external dynamics ($\mathbb{C} \setminus M$) we now investigate the dynamics inside the Mandelbrot set (M), i.e. the internal dynamics.

Attractive components

A particularly interesting part of the Mandelbrot set is given by the set

$$M' = \{c \in \mathbb{C} \mid f_c \text{ has an attractive period}\} \text{ with } M' \subset M.$$

It turns out that the set M' is open and contains infinitely many connected sets [31]. We can divide these sets in accordance to their attractive periods, since we have the property that f_c can contain at most one attractive cycle in K_c for every c ; this follows from theorem 8.6 in [26].

For starters, let us take a look at M'_1 which corresponds to all stable fixed points with period one. We then must have that $\lambda = 2z_0$ under the condition that $\lambda \leq 1$. Furthermore for a fixed point it applies that $z = z^2 + c$, thus

$$M'_1 = \{c \in \mathbb{C} \mid c = \frac{\lambda}{2} \left(1 - \frac{\lambda}{2}\right) \text{ for } \lambda \leq 1\}.$$

The graph is plotted in figure 3.21, furthermore we observe that M'_1 corresponds to the main cardioid of the Mandelbrot set.

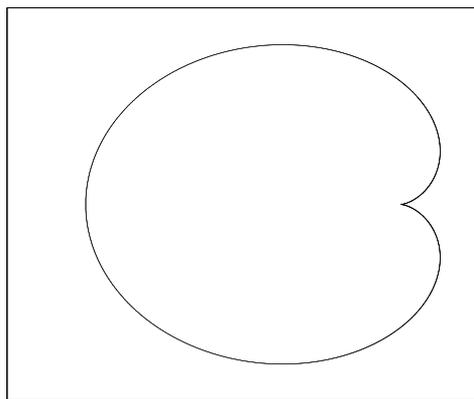


Figure 3.21: Boundary of the main cardioid, numerically generated by making use of the relation $M'_1 = \{c \in \mathbb{C} \mid c = \frac{\lambda}{2}(1 - \frac{\lambda}{2}) \text{ for } \lambda \leq 1\}$.

Centers of attractive components

By a similar method we can find M'_2 corresponding to the attractive periodic two orbits. However Douady and Hubbard showed that for each component, M'_j of M' , there exists a conformal isomorphism $\rho_{M'_j} : M'_j \rightarrow \mathbb{D}$. Where $\rho_{M'_j}(c)$ represents the eigenvalue corresponding to an attractive cycle of $c \in M'_j$. Due to this isomorphism we have that each M'_j has a point $c_{M'_j}$ which is mapped onto zero, hence each M'_j contains a superattractive orbit. We refer to $c_{M'_j}$ as the center of M'_j thus we have that for an attractive n -orbit $\{z_1, \dots, z_n\}$ that

$$\rho_w(c) = 2^n \prod_{i=1}^n z_i.$$

Thus if a single of these z_i 's is equal to zero we will have found the centre $c_{M'_j}$. So they correspond to the zeroes of the n th iterates, i.e. $(f_c^n)'(0) = 0$. This equation has degree 2^{n-1} , thus we may conclude that we can have up to 2^{n-1} disks for a n th period attracting set. Solving $(f_c^n)'(0) = 0$ we find that these disks correspond to the buds located on the Mandelbrot set. Hence these buds correspond to the attractive components of the Mandelbrot set. We have labelled a number of attractive components in figure 3.22.

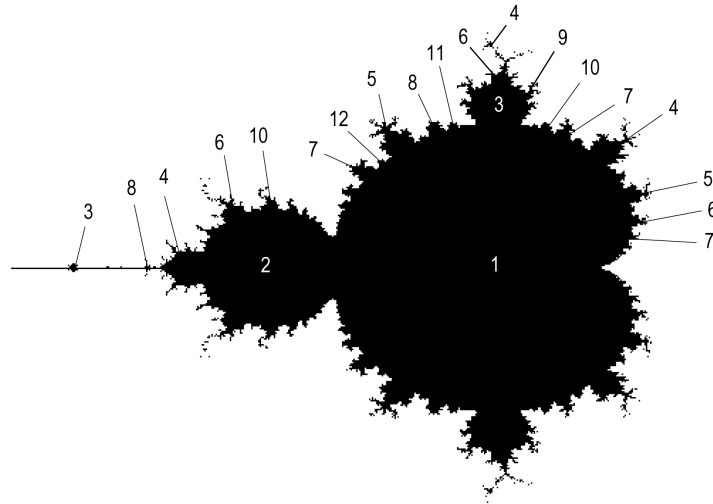


Figure 3.22: We have indicated the attractive periodic orbits of J_c which correspond to the buds of the Mandelbrot set.

Extending attractive components to $\partial M'_j$

The earlier shown mapping can even be extended up to the boundaries of \mathbb{D} and M'_j . We have that if $c \in \partial M'_j$ with $\rho_{M'_j}(c) = e^{2\pi i\beta}$, then it is said that c is a point with internal angle β . The point at which the M'_j buds from a different bud is called a root. It is called a primitive component if it is not budding from another one, then the point represents the cusp of the main cardioid. Roots and primitive components correspond to an indifferent eigenvalue with internal angle $\beta = 0$. Furthermore we have that for rational internal angles with $|\beta| = p/q$ with $p \neq 0$, that at $c \in \partial M'_j$ attractive components sprout from M'_j , these are also called satellite components of M'_j . Let us make it more credible that these points correspond to rational internal angles by an example.

Example: roots of primitive components

In figure 3.23 we have drawn the J_c with $c \in \mathbb{R}$ and their attractive and (rational) indifferent periodic points. This figure corresponds to part of the intersection of the Mandelbrot set with the real line. They are ordered in descending c value, and thus represent what happens when we move from the cardioid to the left bud. As one can see the single attractive point moves to the left, and about halfway a part splits off from the Julia set. We now have that the point to which the $\text{Int}(K_c)$ are attracted lies on the boundary, hence this must be a parabolic orbit, which consequently has a rational internal angle. As we proved earlier, these can be contained in Julia sets. If we decrease c this indifferent point then splits into an attractive period two orbit and thus the period-two bud is born.

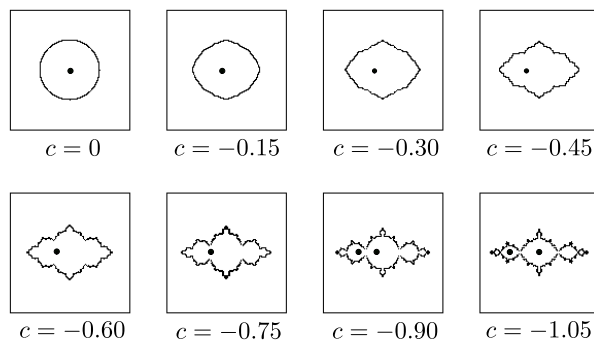


Figure 3.23: J_c with $c \in \mathbb{R}$ ordered in descending c value. The black dots correspond to the point to which the orbits converge inside the interior of K_f . We observe that the single attractive point moves to the left and about halfway a petal appears at the point of attraction of the Julia set. We now have that the periodic point must lie on the boundary. An attractive point cannot suddenly turn into a repelling point, hence this must be parabolic point.

An interesting feature of these satellite components is that they have q -times the attractive period of the internal angle p/q from the disk M_j^i . Let us for example look once again to the main cardioid. For $p/q = 1/2$ we obtain the bud which corresponds to the period-two orbit (see figure 3.22) and indeed $1 \cdot 2 = 2$. For $p/q = \pm 1/3$ we obtain the period-three orbit (see figure 3.22) located at $c = (-1 \pm 3\sqrt{3}i)/8$ and indeed $1 \cdot 3 = 3$

We won't cover the dynamics of irrational angles, but let us just say that the behaviour corresponds closely to Julia sets with Siegel disks. For an extensive overview of the dynamics we refer to [31].

3.3.4 Asymptotic similarity

Let us now move on from $\partial M'_j$ to ∂M . We will be specifically looking at the behaviour around Misiurewicz points.

Definition 3.3.3 (Misiurewicz point) We call $c \in M$ a Misiurewicz point if 0 is eventually periodic for f_c but not periodic.

An example of a Misiurewicz point is $c = i$, since the orbit is given by

$$i \mapsto -1 + i \mapsto -i \mapsto -1 + i \mapsto \dots,$$

If one would numerically generate J_i and magnify part of the Mandelbrot set at $c = i$, one would obtain that these images look almost similar, see figure 3.24. Furthermore a similarity can be found between Julia sets and the Mandelbrot set in a neighbourhood of Misiurewicz points.

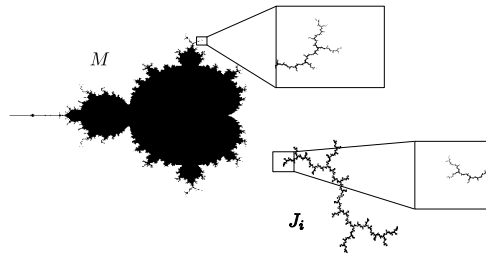


Figure 3.24: Observe that the magnification of M at i looks a lot like the magnification of part of the Julia set J_i .

We first define some general definitions concerning similarity. Then we investigate the similarity of Julia sets and at the end of this section we investigate the similarity between the Mandelbrot set and Julia sets.

For most of the similarity properties we just take part of a closed set, or more specifically a closed disk of a closed set.

Definition 3.3.4 (Closed disk of a closed set) For $r > 0$, and for a closed set $A \subset \mathbb{C}$, we define the closed disk of A by

$$A_r = (A \cap \overline{\mathbb{D}}_r \cup \partial \mathbb{D}_r).$$

Some of the similarity definitions will be defined with respect to the Hausdorff-Chabauty metric.

Definition 3.3.5 (Hausdorff-Chabauty distance in \mathbb{D}_r) Take $A, B \subset \mathbb{C}$, then the Hausdorff-Chabauty distance inside \mathbb{D}_r between A and B is given by

$$d_r(A, B) = \max\{d(A_r, B_r), d(B_r, A_r)\}$$

Let us now divide similarity into three different cases.

Definition 3.3.6 (Similarity) Assume in these three cases that $\rho = |\rho|e^{i\theta}$, $|\rho| > 1$, $0 \leq \theta \leq 2\pi$ and that $A, B \subset \mathbb{C}$.

1. **ρ -self-similar.** The closed set B is called ρ -self-similar around a point x if $\exists r > 0$ such that

$$(\rho\tau_{-x}(B))_r = \tau_{-x}(B)_r$$

where τ_{-x} represents a translation of x to the origin, i.e. $\tau_{-x} : z \mapsto z - x$.

2. **Asymptotically ρ -self-similar.** The set A is called asymptotically ρ -self-similar about a point $x \in A$ if $\exists r > 0$ such that

$$\lim_{n \rightarrow \infty} h((\rho^n \tau_{-x} A)_r, B_r) = 0.$$

The set B will be referred to as the limit set A at x .

3. **Asymptotically similar.** We will call two closed sets A, B asymptotically similar around x if $\exists r > 0$ such that

$$\lim_{t \in \mathbb{C}, t \rightarrow \infty} d_r(t\tau_{-x}A, t\tau_{-x}B) = 0.$$

Remarks:

- The adding of $\partial\mathbb{D}_r$ to the $A \cap \overline{\mathbb{D}_r}$ in definition 3.3.4 is for technical reasons. It is needed for some lemmas concerning the upper and lower bounding of metric spaces by A_r . We refer to lemma 2.1 [34] of Tan Lei's work for an example.
- Definition 3.3.5 differs slightly from the Hausdorff distance as defined in definition 3.2.7 since this metric is only defined locally.
- Definitions (1)(2)(3) in definition 3.3.6 are local properties in the sense that if they hold for some $r > 0$, then they also hold for an $y \in B_\epsilon(x)$ with $\epsilon < r$. Furthermore note that (3) applies $\forall r$ because $t \rightarrow \infty$.

Let us now take a short look at what the definitions 3.3.6 informally mean.

1. If a set B is ρ -self-similar it means that under a scaling of ρ and a rotation of θ we get the untransformed B in \mathbb{D}_r back (inside the closed unit circle).
2. *Asymptotically ρ -self-similar* can be interpreted as magnifying an open area around a point x infinitely many times under ρ and concluding that the set around x stays unchanged if we apply ρ again.
3. One can understand *asymptotic similarity* of two sets by magnifying an area around x and then concluding that the obtained sets are locally similar.

Let us give some examples. We won't formally prove that the given examples correspond to the similarity definitions, since in most case this is rather technical.

Examples: similarity for conventional geometric objects

- Some self-similar examples are the unit circle, \mathbb{D} , a line, a square etc. A spiral is also a self similar object. We will take a look at the spiral in the complex plane given by $\mathcal{S}(c) = \{e^{cx} \mid x \in \mathbb{R}\}$ for $|e^{cx}| > 1$. For if we start at a point on the real line x_1 on the spiral and then make a single turn such that we land back on the axis, let us call this point x_2 , then the shape of the object won't have changed, thus implying that the ρ is given by $e^{(c+2\pi i)}$, which is of course equivalent to stating that ρ is e^c .
- An example of two asymptotically similar sets is a continuous differentiable curve and its tangent.

Example: self-similarity of the Triadic Cantor set

A lot of fractals have a self-similar structure; an example of such a fractal is the earlier treated Triadic Cantor set, C , in section 2.3.1. The Triadic Cantor set is self-similar at every rational point and not at any irrational point $x \in C$. For a point $x \in C$ we have that the base three expansion is given by $x = 0.a_1a_2a_3\dots$ with $a_i \in \{0, 2\}$, see Appendix B for a proof. We have that x is a rational number if and only if its base three expansion is eventually periodic. This means that there exists n, p such that $a_n = a_{n+p}$ for each $n \geq p$. The smallest p is equal to the eventual period of the base-three expansion of x . Since multiplying x by three corresponds to a left shift, we may conclude that C is 3^p -self-similar about $x \in C$ if and only if x is a rational point in C .

Let us now state Tan Lei's theorem concerning self-similarity of invariant closed sets.

Theorem 3.3.2 (Self-similarity of an invariant closed set A) *Let f be a rational map in \mathbb{C} and A a closed set completely invariant under f . Assume that $z_0 \in \mathbb{C}$ is an eventually repelling periodic point for f , i.e. $f^p(f^\ell(z_0)) = f^\ell(z_0)$ with $p \geq 1$ and $\ell \geq 0$. Then A is ρ -asymptotically self-similar about z_0 , where ρ is given by the eigenvalue of the eventually periodic orbit i.e. $(f^p)'(f^\ell(z_0))$. We then have that there exists a conformal mapping $\varphi : \bar{U} \rightarrow V$ where U is an open neighbourhood of z_0 , such that the limit model of A at z_0 is given by*

$$\frac{1}{\varphi'(z_0)}\varphi(A \cap \bar{U}).$$

Furthermore, if z_0 is periodic then we can choose the mapping φ in such a way that it satisfies $\varphi'(z_0) = 0$.

In the case that z_0 is eventually repulsive periodic and satisfies $(f^\ell)'(z_0) \neq 0$, the corresponding limit models of A at z_0 and $f^\ell(z_0)$ are equal up to multiplication by a constant given by $f^\ell(z_0)$.

We have postponed the proof of the periodic case to Appendix F. A full proof can be found in [34].

We are especially interested in the consequences of theorem 3.3.2 for Misiurewicz points. Hence the following corollary.

Corollary 3.3.2 *Assume that c is a Misiurewicz point. Let $\ell, p \in \mathbb{Z}_+$ be chosen as small as possible such that*

$$f_c^p(f_c^\ell(c)) = f_c^\ell(c).$$

Define $\alpha = f_c^\ell(c)$ and $\rho = (f_c^p)'(\alpha)$, then $|\rho| > 1$ and $(f_c^\ell)'(c) \neq 0$. We have that $\tau_{-c}(J_c)$ is asymptotically ρ -self-similar and furthermore that the limit models of $\tau_{-c}(J_c)$ and $\tau_{-\alpha}(J_c)$ are the same up to a multiplication by α . Then there is a complex analytic map φ defined in a neighbourhood of α with $\varphi(\alpha) = 0$, $\varphi'(\alpha) = 1$, such that

$$\varphi \circ f_c^p \circ \varphi^{-1}(z) = \rho z.$$

Furthermore we have that there exists an $r > 0$, a neighbourhood V of α and a neighbourhood U of c , such that $f_c^\ell(\bar{U}) = \bar{V}$ and such that

$$\lim_{n \rightarrow \infty} d_r \left(\rho^n(\tau_{-c}J_c), \frac{1}{f_c^\ell(c)}\varphi(J_c \cap \bar{V}) \right) = \lim_{n \rightarrow \infty} d_r \left(\rho^n(\tau_{-c}J_c), \frac{1}{f_c^\ell(c)}\varphi(f_c^\ell(J_c \cap \bar{U})) \right) = 0.$$

The last statement follows directly from the periodic case of theorem 3.3.2 since $\alpha = f_c^\ell(c)$ and hence p -periodic. The proof of this corollary can be found in [34].

Thus we obtain that J_c is asymptotically ρ -similar about c to $\varphi(J_c \cap \bar{V})$ under multiplication of $1/f_c^\ell(c)$, where $\varphi(J_c \cap \bar{V})$ is the limit model of the asymptotically ρ -similar J_c in a neighbourhood of α . Loosely speaking corollary 3.3.2 states that under infinite times scaling and rotating by ρ in a small enough

neighbourhood of the Misiurewicz point, we will see the same shape back again. With most Julia sets one can numerically verify that after applying ρ a number of times, the image in a small neighbourhood of the Misiurewicz point will almost stay unchanged [34].

To illustrate how one can apply this corollary we present a well known example.

Misiurewicz point for J_i

Let us once again look at J_i with the Misiurewicz point $c = i$ and corresponding orbit

$$i \mapsto -1 + i \mapsto -i \mapsto -1 + i \mapsto \dots$$

The orbit of $c = i$ is eventually periodic; we have that $\ell = 1, p = 2$ and the eventually periodic point corresponds to $f_c^1(c) = i - 1$. Thus $\rho = (f_c^2)'(f_c^1(c)) = 4 + 4i = 4\sqrt{2}e^{\pi i/4}$. We verify numerically that scaling and rotating with ρ will leave the image unchanged, see figure 3.25.

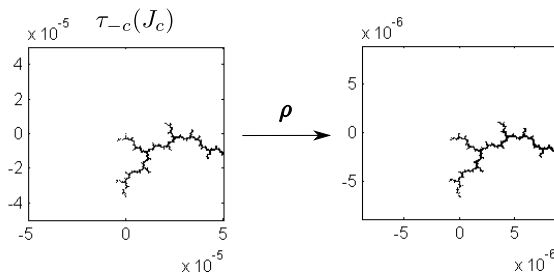


Figure 3.25: If we apply a scaling and rotation by ρ to the left image we get the same image back. Thus this numerical result verifies the similarity around Misiurewicz points.

Let us investigate this process from a different perspective. We have similarity by a rotation of $\pi/4$ and a scaling $4\sqrt{2}$. Thus magnifying by a factor $4\sqrt{2}$ will make the image differ by a rotation of $\pi/4$ from the original image. If we magnify by the factor $4\sqrt{2}$ eight times we will get the original image back. This is similar to the self similarity of a spiral. Since if we make full turn with a spiral we get the original object back. Thus we would expect that the Julia set in a neighbourhood of the Misiurewicz point should look like a spiral. However we only see a dendrite shape which looks nothing like a spiral. Nonetheless let us look at a spiral with corresponding rotation and scaling, see figure 3.26.

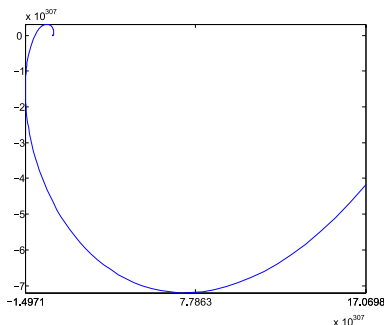


Figure 3.26: A spiral $\{se^{\alpha ix} | x \in \mathbb{R}\}$ with $\alpha = \pi/4$ and $s = 4\sqrt{2}$. Observe by looking at the axis, how long it will take before we would have made a full turn.

We see what the problem is: the stretching dominates the rotation. For a full turn the ρ gets raised to the eighth power, we get $\rho^8 = 2^{20}$, which is rather big. However we can still see the properties of the

spiral by magnification. For if we magnify the dendrite shape at i of J_i eight times (without rotation) the image stays unchanged, as is numerically verified in figure 3.27 .

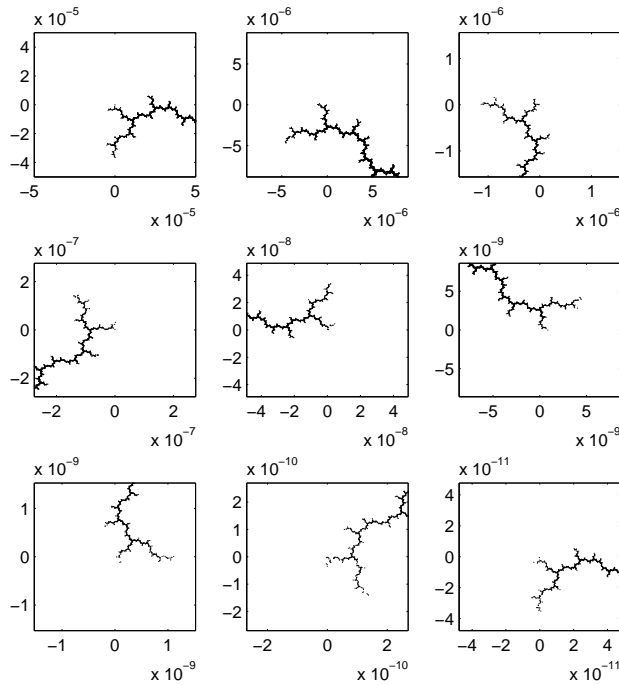


Figure 3.27: The spiral revealed in the dendrite: Observe that as we apply the transformation ρ eight times we get the initial shape back again. Hence the dendrite shape contains still the properties of a spiral.

We can also check the similarity between the limit model at $c = i$ and at $\alpha = i - 1$ of J_i . Let us now refer to the limit model at i as Q and the limit model at $i - 1$ as Z ; we then have according to corollary 3.3.2 that $Z = Q/(f_c^\ell)'(c) = Q/2i$. The limit model Q is given in 3.28.

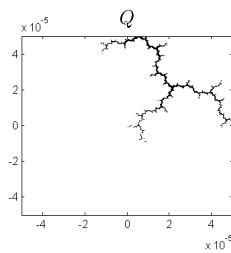


Figure 3.28: Magnification of J_i at $\alpha = i - 1$

We obtain the expected result: the figure 3.28 is exactly the same as the rotated and scaled Z in figure 3.29.

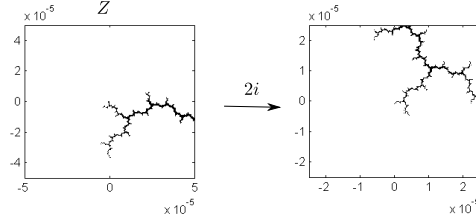


Figure 3.29: Rotating and scaling Z by $2i$ yields the same object as Q (as in figure 3.28). This verifies the similarity between the limit model at i , Q , and the limit model at $i - 1$, Z .

Remark: All magnifications of the Mandelbrot set are translated to the origin. We have done this because we encountered round-off errors in the figure toolbox of MATLAB.

We now wish to extend theorem 3.3.2 to the Mandelbrot set. We state here the result from Tan Lei [34].

Theorem 3.3.3 (Similarity between Julia sets and the Mandelbrot set) *Let c_0 be a Misiurewicz point. Then we have that there exists a $|\rho| > 1$, $r, r', s > 0$, a closed set $Z \subset \mathbb{C}$ with $\rho Z = Z$, and a $\gamma \in \mathbb{C} \setminus \{0\}$ such that*

$$\lim_{n \rightarrow \infty} (\rho_0^n \tau_{-c_0} J_{c_0})_r = Z_r,$$

$$\lim (\rho_0^n \tau_{-c_0} M)_{r'} = (\gamma Z)_{r'}$$

and

$$\lim_{t \in \mathbb{C}, t \rightarrow \infty} d_s(t\tau_{-c_0} M, t\gamma\tau_{-c_0} J_{c_0})$$

where $\rho_0 = (f_{c_0}^p)'(\alpha(c_0))$ and where $\alpha(c)$ is given by $\alpha(c) =: f_c^p(\alpha(c))$. Moreover, we have that

$$\gamma = \frac{(f_{c_0}^\ell)'(c_0)}{\frac{d}{dc}(f_c^\ell(c))|_{c=c_0} - \frac{d}{dc}(\alpha(c))|_{c=c_0}}.$$

Informally we could state that theorem 3.3.3 states that the Mandelbrot set is self-similar about a Misiurewicz point c_0 and that M and J_{c_0} are asymptotically self-similar up to a multiplication of a constant complex number γ . One can obtain some pretty interesting results by applying this theorem. We give two examples.

Example: Triple point

The upper triple point is located in between the period three bud and the branch at $c = i$. This three-point bifurcation is given by $c_0 = -0.1011 + 0.95629i$ and is a Misiurewicz point. In this case $\ell = 3$ and $p = 1$. With some elementary calculus we obtain the following values

$$\begin{aligned} \alpha &= \frac{1}{2}(1 - \sqrt{1 - 4c}) \approx -0.3276 + 0.57776i, \\ \rho_0 &= 2\alpha \approx -0.6552 + 1.15552i. \end{aligned}$$

Furthermore we have that $\frac{d}{dc}(f_c^\ell(c))|_{c=c_0} - \frac{d}{dc}(\alpha(c))|_{c=c_0} \approx -4.7515 + 2.06497i$ and $(f_{c_0}^3)'(c_0) \approx -6.4464 + 0.1808i$. Hence $\gamma = 1.15508 + 0.46394i$, with $\text{Arg}(\gamma) = 0.381929$ and $|\gamma| = 1.24477$. Finally we verify theorem 3.3.3 with the numerical result in figure 3.30.

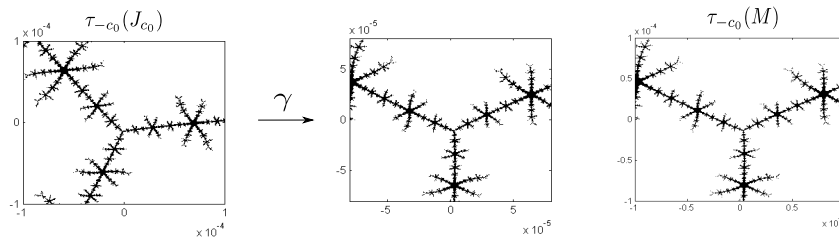


Figure 3.30: If we transform an area around the triple point $\tau_{-c_0}(J_{c_0})$ and apply γ the result will be similar to $\tau_{-c_0}(M)$

Example: Misiurewicz point at $c_0 = i$

For the Misiurewicz point at $c_0 = i$ we have that $\gamma = 1 + i/2$, with $\text{Arg}(\gamma) = 0.4637$ and $|\gamma| = \sqrt{5}/2$. Indeed we can verify theorem 3.3.3 again numerically as is shown in figure 3.31.

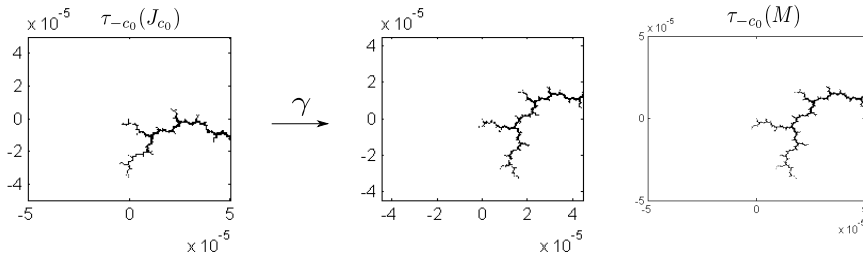


Figure 3.31: If we transform an area around the dendrite at $\tau_{-c_0}(J_{c_0})$ and apply γ , the result will be similar to $\tau_{-c_0}(M)$.

Example: Misiurewicz point at $c_0 = -0.7756\dots + 0.13646\dots i$

The Misiurewicz point at $c_0 = -0.7756\dots + 0.13646\dots i$ has a spiral structure. When we zoom in on a point close to $c_0 = -0.7756\dots + 0.13646\dots i$, as is done in figure 3.32, we see smaller Mandelbrot sets appearing.

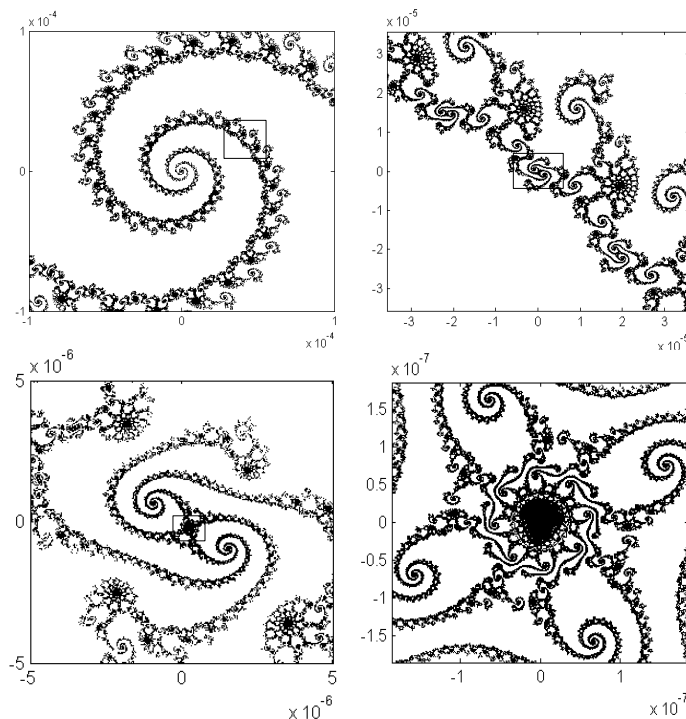


Figure 3.32: We have magnified part of the spiral of the Mandelbrot set (indicated with the rectangles) at $c_0 = -0.7756\dots + 0.13646\dots i$. Observe that a smaller Mandelbrot set is appearing in the last magnification. If one would magnify the corresponding Julia set one would not see these mini-Mandelbrot sets, since the Julia set J_{c_0} has empty interior.

Research has already been done by J.P. Eckmann and H. Epstein to the existence and the scaling properties of these sets in a neighbourhood of a Misiurewicz point [17]. Their result states that as we approach a Misiurewicz point, there is a sequence of copies of the Mandelbrot set which converge geometrically to c_0 with a ratio $1/\rho_0$, moreover the diameter of these copies decreases with $1/|\rho_0|^2$. Thus they will disappear as we zoom in on the Misiurewicz point c . Indeed since J_{c_0} contains no interior points M at c_0 will also not contain any interior points.

Chapter 4

The Lorenz attractor

The Lorenz attractor arises from the Lorenz system. The Lorenz system is derived from partial differential equations describing Rayleigh-Bénard convection, which studies how heat rises through an ideal gas which is cooled from above and heated from below. This system isn't closed meaning that if the fluid is heated enough it will 'leave' the system. E.N. Lorenz wanted to numerically show that this system has sensitive dependence on initial values. This fluid motion can be described as a system with infinitely variables, Lorenz made the enormously simplifying assumption that this sensitive dependence would still be present if all but three equations would stay constant. This brings us to the Lorenz system given by

$$\begin{aligned}x' &= \sigma(y - x), \\y' &= rx - y - xz, \\z' &= xy - bz.\end{aligned}$$

We denote the Lorenz system by $X' = \mathfrak{L}(X)$ with $X = (x, y, z)^T$. We are now dealing with a continuous time set, the state space is given by \mathbb{R}^3 and for the flow we write $\Phi(X_0, t)$ with $X_0 \in \mathbb{R}^3$.

Lorenz investigated the system for the parameters: $\sigma = 10$, $b = 8/3$ and $r = 28$. Numerically solving for initial states $X = (0, 1, 0)$ and $Y = (0, -1, 0)$, we obtain the figures 4.1(a), 4.1(b). The invariant figure to which the solution curves converge is called the Lorenz attractor.

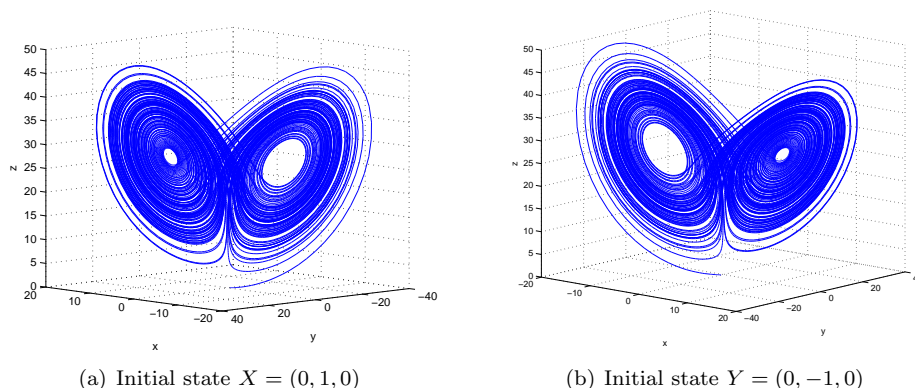


Figure 4.1: Solution curves of the Lorenz system with parameter values $\sigma = 10$, $b = 8/3$ and $r = 28$.

In this chapter we start with a discussion of the Lorenz system with a free choice of parameters. After which we restrict ourselves to the Lorenz system of the Lorenz attractor. We come to a brief discussion of the dynamics of the Lorenz attractor from a numerical and a theoretical perspective. To get a

better understanding of the dynamics we can create a simplification of the Lorenz system: the Rössler system. Rössler system won't preserve some characteristic features of the Lorenz system. Hence we will aim to create a model for the Lorenz system which contains all the characteristic behaviour of the Lorenz system. Then by performing an extensive theoretical research on this model we can give a thorough description of the dynamics and even prove that the model has an attractor.

4.1 Lorenz system

Similarly to the Hénon mapping in chapter 2 let us investigate some elementary properties of the Lorenz system $X' = \mathfrak{L}(X)$, such as stability of equilibria and possible trapping region.

A first observation of \mathfrak{L} yields that under reflection in the z -axis solutions stay invariant, i.e. if $(x(t), y(t), z(t))$ is a solution then $(-x(t), -y(t), z(t))$. As is also verified by the solution curves in figure 4.1(a) and 4.1(b)

We continue with an investigation of the equilibria. For $r < 1$ and $b > 0$ one will have a single equilibrium:

$$Q_0 = (0, 0, 0).$$

By linearising one obtains the eigenvalues of Q_0 :

$$\lambda_0 = -b, \quad \lambda_{\pm} = \frac{1}{2} \left(-(\sigma + 1) \pm \sqrt{(\sigma + 1)^2 - 2\sigma(1 - r)} \right).$$

Hence the origin is a sink. Furthermore one can prove that in this case all solutions tend to the origin. We omit the proof and refer to [14].

As we increase the r through one, we can make two observations:

- The origin will turn into a saddle point with a stable surface and an unstable curve, since the eigenvalues are given by $\lambda_+ > 0$, $\lambda_- < 0$ and $\lambda_0 < 0$. Consequently it is no longer true that all solutions tend to the origin.
- We get two additional equilibrium points: $Q_{\pm} = (\pm\sqrt{b(r-1)}, \pm\sqrt{b(r-1)}, r-1)$.

By assuming that $r > 1$ and $b > 0$ we will show below that a trapping region can be found for the Lorenz system.

Proposition 4.1.1 (Trapping region Lorenz) *There $\exists R > 0$ such that $\forall v_0 \in \mathbb{R}^3$ we have that $\Phi(v_0, t_0) \subset U$, in which U is the ellipsoid given by $V(x, y, z) = rx^2 + \sigma y^2 + \sigma(z - 2r)^2 < R$ than $\Phi(v_0, t) \subset U \forall t \geq t_0$*

Proof. Let us define the boundary of the ellipsoid ∂U by

$$rx^2 + y^2 + b(z - r)^2 = R$$

with $R > 0$. Take V as given in the proposition as the Lyapunov function; computing \dot{V} yields

$$\dot{V} = -2\sigma(rx^2 + y^2 + b(z - r)^2 - br^2).$$

If we could prove that $\exists R$ such that $\dot{V} < 0$ for all points which are not contained in the ellipsoid, ∂U , then all solution curves will enter the ellipsoid ∂U . Take $R > br^2$, this will imply that $\dot{V} < 0$. Concluding: all solution curves enter the ellipsoid $rx^2 + \sigma y^2 + \sigma(z - 2r)^2 < R$. \square

By construction of this trapping region we are now able to prove that the Lorenz system contracts area for certain parameter values. The proof is presented below.

Proposition 4.1.2 *If $\sigma + 1 + b > 0$ then the Lorenz system contracts area.*

Proof. Let \mathcal{S}^2 be a sphere in \mathbb{R}^3 ; furthermore let us define the image of \mathcal{S}^2 under a time- t map of the flow by $\mathcal{S}^2(t) := \Phi(\mathcal{S}^2, t)$, which is an ellipsoid. Define the volume of $\mathcal{S}^2(t)$ by $V(t)$. According to Liouville's theorem we have

$$\frac{dV}{dt} = \int_{\mathcal{S}^2(t)} \operatorname{div} \mathfrak{L}(X) \, dx dy dz .$$

Computing the divergence yields

$$\frac{dV}{dt} = -(\sigma + 1 + b)V .$$

From the initial conditions we have that $V(0) = 1$, hence $V(t) = e^{-(\sigma+1+b)t}$, thus the rate of contraction is given by $e^{-(\sigma+1+b)t}$. So in the cases that $\sigma + 1 + b > 0$ the Lorenz system contracts area. \square

4.2 Lorenz attractor

We now restrict ourselves to the investigation of the Lorenz system for the parameter values: $\sigma = 10$, $b = 8/3$ and $r = 28$. For these values a chaotic attractor occurs: the Lorenz attractor.

4.2.1 Dynamics

The Lorenz system corresponding to the Lorenz attractor is given by

$$\begin{aligned} x' &= 10(y - x) \\ y' &= 28x - y - xz \\ z' &= xy - (8/3)z . \end{aligned}$$

From now on when referring to the Lorenz system we will mean the Lorenz system corresponding to the Lorenz attractor.

First observe that by proposition 4.1.2 from section 4.1 that the Lorenz system contracts area, thus similarly as with the Hénon attractor, the Lorenz attractor has area zero.

We also obtain from section 4.1 that the Lorenz system has three equilibria:

$$Q_0 = (0, 0, 0), \quad Q_{\pm} = (\pm\sqrt{72}, \pm\sqrt{72}, 27) .$$

We can split the dynamics into two parts: dynamics of the equilibrium point at Q_0 and dynamics of the two equilibria Q_{\pm} .

Dynamics at Q_0

Computing the eigenvalues of the equilibrium at the origin yields

$$\lambda_0 = -8/3, \quad \lambda_{\pm} = -\frac{11}{2} \pm \frac{\sqrt{1201}}{2} .$$

The behaviour around the origin can be obtained by linearising the set of differential equations around the origin:

$$\tilde{X}' = \begin{pmatrix} \lambda_- & 0 & 0 \\ 0 & \lambda_+ & 0 \\ 0 & 0 & \lambda_1 \end{pmatrix} \tilde{X} .$$

The phase portrait of this linearisation is displayed in figure 4.2.

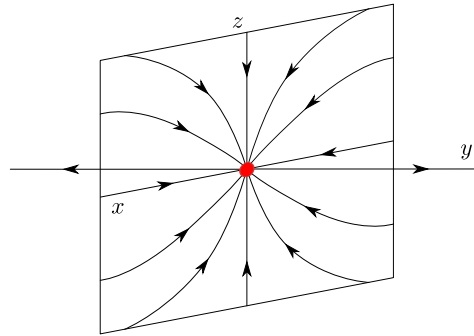


Figure 4.2: Phase portrait of the linearised Lorenz system at the origin. We see that the origin has a stable surface and unstable curve.

The linearisation has an unstable curve and a stable plane. Observe that all the solution curves in the stable plane will tend to origin tangentially to the z -axis.

Dynamics at Q_{\pm}

Computing the eigenvalues of Q_{\pm} yields a single negative eigenvalue and two complex conjugate eigenvalues. By symmetry in the z -axis of the Lorenz system we can conclude that solution curves spiral in opposite direction to each other around Q_{\pm} , as is represented in figure 4.3.

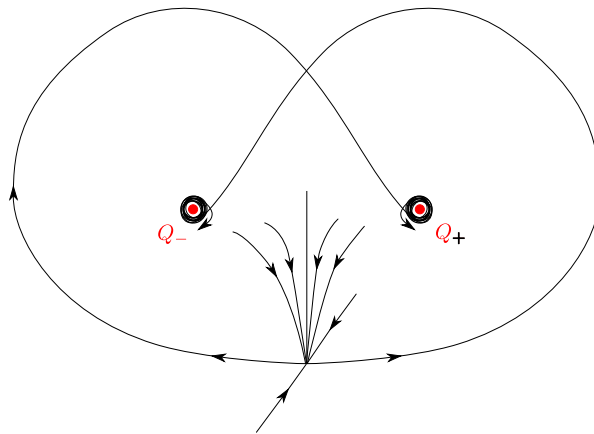


Figure 4.3: The solution curves move in opposite direction around the equilibria Q_{\pm} .

This spiralling around Q_{\pm} is a characteristic feature of the Lorenz system. This process is clearly visible when we follow a solution curve in the zx -plane, see figure 4.4.

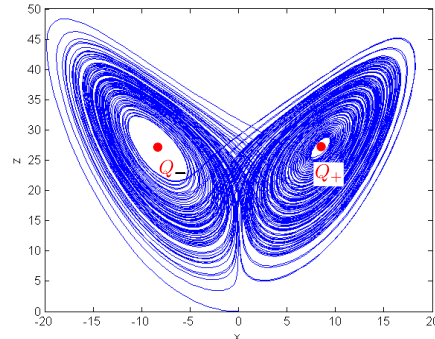


Figure 4.4: Numerically generated figure of a solution curve in the zx -plane. Observe the spiralling around the equilibria Q_{\pm} .

Following the solution curve in figure 4.4 we see that it spirals around each of the equilibria. However when a critical distance is reached from a Q_{\pm} the solution curve will be ejected and spiral around Q_{\mp} , after which the process repeats. The number of turns that a solution curve makes around one equilibrium before it leaves the spiral is not specified. Furthermore it is thought that for a sequence of not too large numbers, representing the turns that the solution curve makes around each of the equilibria, there exists a path on the Lorenz attractor, however this statement is still unproven [23].

Chaotic dynamics of the Lorenz system

With the behaviour around the equilibria we can already describe the chaos generating mechanism of the Lorenz system. We do this by following the solution curves with initial values corresponding to a segment, I , of the line connecting Q_- to Q_+ as indicated in figure 4.5.

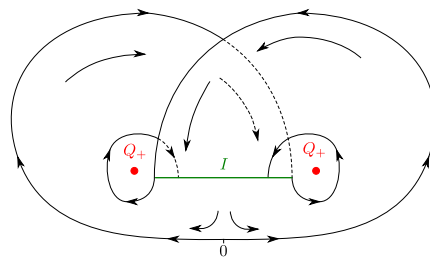


Figure 4.5: Solution curves with initial values corresponding to the line segment I as they make a full turn around Q_{\pm} . Following these solution curves we obtain that the overall process can be described as stretch, split and merge.

As the solution curves tend towards the origin they will be stretched until they are so far apart that they split. This stretching is a consequence of the stable curve and this splitting is a consequence of the unstable plane at the origin. The solutions curves will then move around Q_- or Q_+ and then, as they return to the origin, they will be merged. The Lorenz system can then be summarized as a stretch-split-merge process. This stretch-split-merge process has as consequence that solution curves

which start near to each will separate, this gives us good grounds to believe that the Lorenz system has sensitive dependence on initial values.

4.2.2 Numerical investigation

The chaos in the Lorenz system was discovered by Lorenz through a numerical investigation [24]. We will cover some of his results and in doing so present evidence that the Lorenz system has sensitive dependence on initial values.

Single solutions with respect to time

Numerically solving the Lorenz system with initial value $X_0 = (0, 1, 0)$ yields figure 4.6.

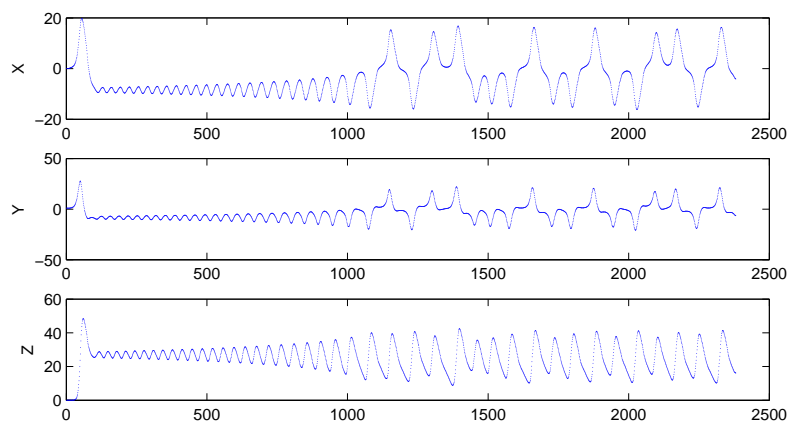


Figure 4.6: The three solution curves: $x(t)$, $y(t)$ and $z(t)$ with initial value $X_0 = (0, 1, 0)$.

We observe that the behaviour of $x(t)$ and $y(t)$ look pretty similar. This follows from their physical interpretation, let us quote Lorenz [24]: ‘In these equations x is proportional to the intensity of convective motion, while y is proportional to the temperature difference between the ascending and descending currents, similar sign denoting that warm fluid is rising and that cold fluid is descending.’ Consequently the intensity of convection is directly related to the temperature difference of the fluids.

We are left with $z(t)$ which is proportional to the distortion of the vertical temperature profile from its equilibrium. Hence $z(t)$ is related to $y(t)$ in absolute sense. For a more detailed description and perhaps derivation of these equations we refer to [24].

For simplicity we restrict further discussion to $y(t)$. One can extend the arguments to $x(t)$ and $z(t)$ by the physical relation between the solutions. In figure 4.6 one sees an instability at the beginning, i.e. the rapid increase of $y(t)$. The physical interpretation is that there is an increase in temperature difference between the ascending and descending current, which leads to even colder sinking fluid and even warmer ascending fluid, until it ascends so much that it get carried away over the top of the system. Then $y(t)$ seems to tend to a steady state solution for a while. At $t = 500$ the amplitude of the solution begins to rapidly increase until $y(t)$ at approximately $t = 1100$ hits the vertical axis. This corresponds to an unstable state due to fact that the difference between the ascending and descending currents is zero; it could go either way: warm fluid descending and cold fluid ascending or warm fluid ascending and cold fluid descending. Once this critical state is reached $y(t)$ will show unpredictable behaviour every time it hits the vertical axis. This can be considered as evidence for sensitive dependence of initial values of the Lorenz system.

One-dimensional dynamics

The chaotic feature in the Lorenz attractor can be reduced to an one-dimensional system. We stated earlier that a solution curve spiralling around Q_{\pm} will spiral around Q_{\mp} if a certain critical distance is reached from the equilibrium. Furthermore with a more thorough investigation we can conclude that this critical distance determines at which point the solution curve will enter the spiral [24]; consequently this will determine the amount of turns needed before it leaves the spiral. A suitable feature which determines this critical distance is the one-dimensional dynamics of the z -maxima.

We can investigate the dynamics of the z -maxima by considering consecutive maxima's, as is displayed in figure 4.7.

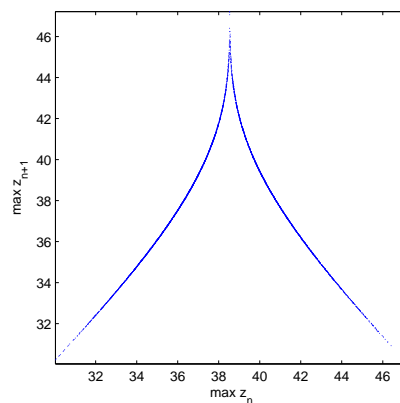


Figure 4.7: The numerical generated plot of the old maxima, $\max z_n$, against the new maxima, $\max z_{n+1}$.

The figure corresponds closely to a variation on the Baker transformation called the Tent map, which is given by

$$T : x \mapsto \begin{cases} 2x \bmod 1 & \text{if } x < 1/2 \\ 2 - 2x \bmod 1 & \text{if } x \geq 1/2 \end{cases} \quad \text{with } x \in [0, 1). \quad (4.1)$$

The Tent map is visualized in figure 4.8.

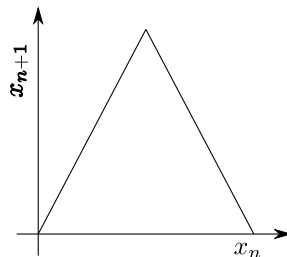


Figure 4.8: The Tent map

Taking $T(x_{n-1}) = x_n$ consider the orbit corresponding to an initial value x_0 . Now consider the perturbed orbit $\tilde{x}_0 = x_0 + \epsilon$ with $\epsilon > 0$, then for k sufficiently large the orbits will separate since

$|\tilde{x}_k - x_k| = |2^k \cdot \epsilon|$, hence the Tent map shows sensitivity on initial values. We can extend this argument to the map of the z -maxima. However we first need to define the map corresponding to the z -maxima.

Call the z -maxima map Z_{\max} . The map Z_{\max} can be defined in a similar way to the tent map in equation 4.1. Apart from scaling and translation the only difference is that the multiplication by two of x , in $2x$ and in $2(1-x)$, in equation 4.1 is replaced by the derivative of figure 4.7 at $\max z_n$. Write the derivative of figure 4.7 at $\max z_n$ as Γ_n and set $Z_{\max}(\max z_{n-1}) = \max z_n$. Then for the initial value $\max z_0$ and perturbed initial value $\max \tilde{z}_0 = \max z_0 + \epsilon$ with $\epsilon > 0$ it follows that $|\max \tilde{z}_k - \max z_k| = |\Gamma_0 \cdot \dots \cdot \Gamma_k \cdot \epsilon|$. From figure 4.7 it follows that the derivative in absolute value is everywhere greater than one, hence Z_{\max} has sensitive dependence on initial values. Returning to the interpretation of the z -maxima, we conclude that the turns that a solution curve makes around each equilibria behaves chaotic.

Remarks:

- In the paragraphs above we have not formally proved sensitivity of initial values in the sense of definition 2.3.3. However the proof that the Baker transformations has sensitive dependence on initial values (proposition 2.3.1) can be used to proof sensitive dependence on initial values of the Tent map. This proof can then be extended to the map Z_{\max} by creating a lower bound of $|\max \tilde{z}_k - \max z_k|$ by use of a different base.
- We can also view the Lorenz system with a free choice of the parameter r by its consecutive z -maxima. For as r varies the shape of figure 4.7 changes. Numerically generating the range of the z -maxima against the parameter r we obtain a bifurcation diagram of the Lorenz system; for an extended discussion we refer to [1].

4.2.3 Lyapunov exponents and numbers in flows

In section 2.3.2 we showed how to compute Lyapunov exponents and numbers for systems with a discrete time set. We will now extend this to systems with a continuous time set.

Definition 4.2.1 (Lyapunov number, exponent for a continuous time set) *The Lyapunov number, respectively the Lyapunov exponent of a flow $\Phi(x_0, t)$ is defined as the Lyapunov number, respectively the Lyapunov exponent of the associated time-one map, i.e. $\Phi^1(x_0)$.*

The calculation of these values is not completely the same as was treated with discrete systems, since the value of $D\Phi^1(x_0)$ isn't explicitly known.

Take a differential equation $\dot{x} = f(x)$ with $f : \mathbb{R}^m \rightarrow \mathbb{R}^m$ and flow Φ^t , then we have for an initial value x_0 that

$$\frac{d\Phi^t(x_0)}{dt} = f(\Phi^t(x_0)).$$

By the chain rule we obtain

$$\frac{dD\Phi^t(x_0)}{dt} = Df(\Phi^t(x_0)) \cdot D\Phi^t(x_0). \quad (4.2)$$

The equation above is also called the variational equation. By the definition of the flow we must have that $D\Phi_0(x_0) = I$, where I is the identity matrix, since $\Phi(x_0, 0) = x_0$. Thus by solving equation 4.2 we can find $D\Phi_t(x_0)$ for a given orbit and thus calculate the Lyapunov numbers and exponents. We can proceed in exactly the same way in the numerical computation of the Lyapunov numbers and exponents as we do in Appendix C with Gram-Smidt orthonormalization method.

Example: Numerical calculation of the Lyapunov exponent and dimension of the Lorenz attractor

Numerically computing the Lyapunov exponents and dimensions of the Lorenz attractor yields

$$h_1 = 0.9061 \quad h_2 = -2.2787 \cdot 10^{-4} \quad h_3 = -14.5695 \quad D_\ell = 2.06.$$

We see similarly to the Hénon attractor that it is contracted in one direction and expanded in another direction. The expanding direction corresponds to the sensitivity on initial values of the Lorenz system. As with the Hénon attractor the Lorenz attractor has a Cantor set structure. In the case of the Lorenz attractor we have infinite disconnected surfaces due to the stretch-split-merge process and hence the Lyapunov dimension is slightly above 2.

We can check our Lyapunov exponents by the result that $e^{h_1+h_2+h_3}$ is equal the average volume contraction of the Lorenz attractor. The average volume contraction, given in the proof of 4.1.2, is $e^{-(\sigma+1+b)}$. We obtain

$$e^{-(\sigma+1+b)} = 1.1605 \cdot 10^{-6} \approx e^{h_1+h_2+h_3} = 1.1641 \cdot 10^{-6}.$$

We observe that the error is acceptable.

The Lyapunov exponent h_2 in the example above is almost zero. Indeed it is the case that in a perfect world without numerical errors the Lyapunov exponent, h_2 , would be equal to zero. This follows from the next theorem.

Theorem 4.2.1 (h_i of an autonomous flow) *A bounded orbit of an autonomous flow has always one Lyapunov exponent equal to zero or otherwise we will have that it has an equilibrium point in its ω -limit set.*

The definition of ω -limit set extended to continuous times sets is given as follows.

Definition 4.2.2 (ω -limit set) *Let (M, T, Φ) be a dynamical system and $x \in M$. The ω -limit set of x is given by*

$$\omega(x) = \{y \in M \mid \exists \{t_j\}_{j \in \mathbb{N}} \subset T, \text{ such that } t_j \rightarrow \infty \text{ and } \Phi^{t_j}(x) \rightarrow y\}.$$

An important property of the time t -map, $D\Phi^t(x_0)$, is that it maps small variations tangent to an orbit at time 0, to the tangent of the the orbit at time t . The derivation can be found in [1].

Proof of theorem 4.2.1. Take a differential equation $\dot{x} = f(x)$ with $f : \mathbb{R}^m \rightarrow \mathbb{R}^m$ and flow Φ^t . It holds that for an initial value $x_0 \in \mathbb{R}^m$ that if the $\omega(x_0)$ doesn't contain any equilibrium points, then $f(\Phi^t(x_0)) \neq 0$ for $t > 0$. It is given that $f(\Phi^t(x_0))$ is bounded for all $t > 0$. Thus there exists $\gamma, \Gamma \in \mathbb{R}^m$ such that $0 < \gamma < |f(\Phi^t(x_0))| < \Gamma, \forall t > 0$. Now let us represent the total expansion in the direction of $f(x_0)$ after n time units by $E(n)$. Then we can bound this $E(n)$ by

$$0 \leq \lim_{n \rightarrow \infty} \frac{1}{n} \log \gamma \leq \lim_{n \rightarrow \infty} \frac{1}{n} \log E(n) \leq \lim_{n \rightarrow \infty} \frac{1}{n} \log \Gamma \leq 0.$$

Hence the Lyapunov exponent in the direction tangent to the orbit equals zero. \square .

4.2.4 Attractor

We will now generalize the definition of attractor to discrete and continuous time sets.

Definition 4.2.3 (Attractor) Let (M, T, Φ) be a dynamical system and $x \in M$. An $\omega(x)$ is called an attractor if and only if there exists an arbitrarily small neighbourhood of $\omega(x)$ such that $\Phi(U \times \{t\}) \subset U$ and such that

$$\bigcap_{i=0}^{\infty} \Phi^i(U) = \omega(x)$$

for all $0 < t \in T$.

We shall use a weaker definition of attractor for the Lorenz attractor, more specifically we adopt the definition used by Tucker in his Phd. thesis [36].

Definition 4.2.4 (Tucker Attractor) Define a dynamical system (M, T, Φ) . Then $\Lambda \subset M$ will be called a Tucker attractor if and only if

1. Λ is compact and Φ^t -invariant .
2. There exists an open set $U \subset M$ with $\Lambda \subset U$ such that for each $x_0 \in U$ we have that $\Phi(x_0, t) \in U$ for all $0 < t \in T$ and such that $\bigcap_{t \geq 0} \Phi(U, t) = \Lambda$.
3. (Transitivity) Given any points $y_1, y_2 \in \Lambda$ and open neighbourhoods $V_j \subset M$, $j = 1, 2$ such that $y_j \in V_j$. Then there exists a solution curve which begins in U_1 and passes through V_2 .

It follows that an attractor implies Tucker attractor. Since all three conditions are properties of the ω -limit set. It is clear that the first two conditions in the Tucker must be properties of an attractor, for they imply invariance and attracting. The last condition may seem a little strange, but this guarantees that the Λ in definition 4.2.4 is a single attractor, to illustrate this we present the following example.

Example: non-attractor

Take the set of differential equations

$$\begin{aligned} x' &= x - x^3, \\ y' &= -y. \end{aligned}$$

A quick investigation of the dynamics yields that the system contains a single saddle point at the origin and two sinks located at $(\pm 1, 0)$. Drawing the phase portraits one obtains figure 4.9.

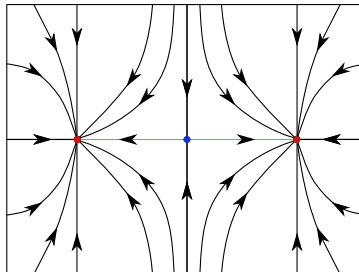


Figure 4.9: An non-transitive system: solutions in the left half plane will converge to the left sink and solutions in the right half plane will tend to the right sink.

It seems plausible that the green line is a Tucker attractor. Let us check this. Property one and two of Tucker's definition of attractor are satisfied. Property three isn't satisfied since solutions in each half plane tend to a single sink, thus the invariant set isn't transitive. However a single sink does correspond to a Tucker attractor.

4.3 Rössler attractor

For complicated systems it is quite often a fruitful idea to investigate a simplification. In a similar way that the Lozi map is a simplification of the Hénon map, the Rössler system is a simplification of the Lorenz system. The Rössler system is given by the set of differential equations

$$\begin{aligned}x' &= -(y + z), \\y' &= x + ay, \\z' &= b + xz - cz.\end{aligned}\tag{4.3}$$

Numerically solving the differential equation above for the parameters $a = 0.2$, $b = 0.2$ and $c = 5.6$, yields figure 4.10.

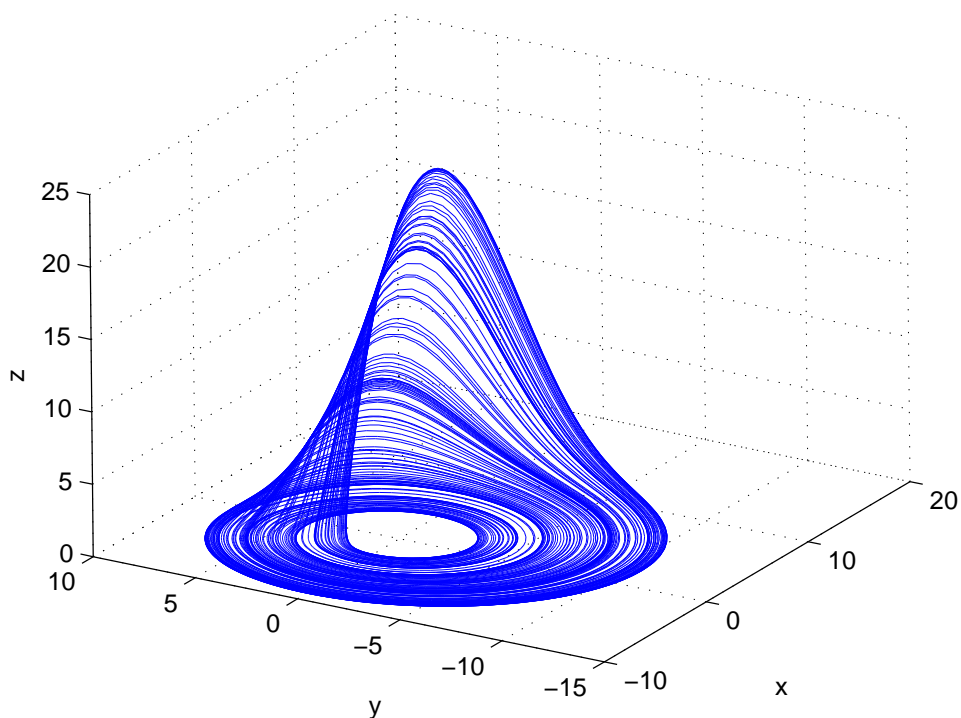


Figure 4.10: The Rössler attractor. Observe how the solution curves get folded double as they make a rotation.

Let us give a better explanation what the transformation corresponding to the set of differential equations in 4.4 does. We have graphically represented this process in figure 4.11.

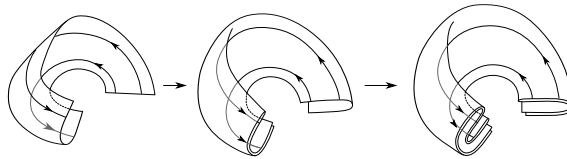


Figure 4.11: Stretch and fold operation in the Rössler attractor: we have drawn here the transformation performed on an initial line segment as we make three complete turns around the z -axis. With each turn it gets stretched and folded double.

Following an initial line segment as we make a turn beginning from the negative x -axis, we see that as we move forward in time the segments get stretched till we have made about half a turn. Completing the turn we see that the band folds double and the process repeats. This transformation corresponds to the stretch and fold process that we have seen in so many chaotic systems: Hénon and Lozi map, Baker transformation etc. This is an indication that the Rössler attractor is chaotic. One also sees that the Rössler-attractor is a simplified model of the Lorenz attractor since the Lorenz system performs a stretch-split-merge operation.

4.4 A model for the Lorenz system

We are now going to create a model for the Lorenz system from which we can give an extensive description of the dynamics. This model was created by Guckenheimer and Williams [19]. It was shown by Tucker that this model indeed corresponds to the Lorenz system for certain parameters [36].

The treated investigation will take place in two parts: first a reduction from the dynamics from \mathbb{R}^3 to \mathbb{R}^2 , this will lead to the proof that the model is an attractor, secondly a continuation of the reduction from \mathbb{R}^2 to \mathbb{R} , this will lead to the proof that the model has sensitive dependence on initial values.

4.4.1 Creating a model for the Lorenz system

The model of the Lorenz system must satisfy the characteristic properties of the Lorenz system which we came across in previous sections. Let us summarize these properties.

Characteristic properties of the Lorenz system

1. Invariance of solution curves under reflection in the z -axis.
2. Three equilibria: $Q_0 = (0, 0, 0)$, $Q_{\pm} = (\pm\sqrt{72}, \pm\sqrt{72}, 27)$. Q_0 has three eigenvalues, $\lambda_1, \lambda_+, \lambda_-$ satisfying $\lambda_- < -\lambda_+ < \lambda_1 < 0 < \lambda_+$. Q_{\pm} has one negative and two complex conjugate eigenvalues.
3. The chaotic generating mechanism corresponds to a stretch-split-merge operation, as indicated in figure 4.5.
4. Lorenz system contracts area (Lorenz attractor has volume zero).

We start the model by placing an equilibrium at the origin. The model of the Lorenz system will only need to preserve relative size, hence according to property 1 we choose the eigenvalues $\lambda_- = -3$, $\lambda_0 = -1$, $\lambda_+ = 2$ for the equilibrium at origin.

Now let us assume that the model for the Lorenz system satisfies a linear system inside the T -shaped object as given in figure 4.12.

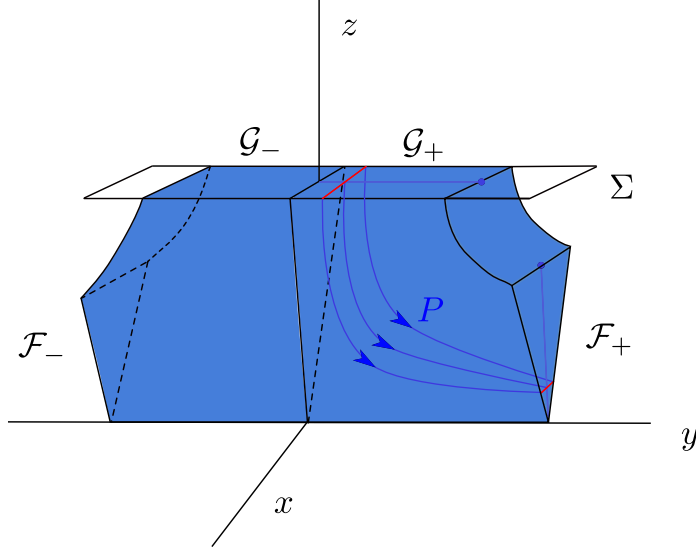


Figure 4.12: The behaviour of solution curves inside the T-shape. Observe how the map P maps solution curves from \mathcal{G}_\pm to \mathcal{F}_\pm , respectively. Also observe that the mapping maps a line parallel the y -axis in \mathcal{G} to a line parallel to the z -axis in \mathcal{F}_\pm

Define Σ to be the plane given by $|x|, |y| \leq 20, z = 27$, see figure 4.12. Then define $\mathcal{G} \subseteq \Sigma$ to be the plane $|x| \leq 20, z = 27, |y| = d < 27$. \mathcal{G} is then given by the top of the T -shape in figure 4.12. Let us also define $\mathcal{G}_+ = \mathcal{G} \cap \{y > 0\}$ and $\mathcal{G}_- = \mathcal{G} \cap \{y < 0\}$. the linearized system inside T will be given by:

$$\begin{aligned} x' &= -3x, \\ y' &= 2y, \\ z' &= -z. \end{aligned}$$

Observe that the given system satisfies property 1.

We now want to describe how the solutions which start in \mathcal{G} are mapped onto the sides \mathcal{F}_\pm of the T -shape, see figure 4.12. The solutions curves with initial values on the line $y = 0, z = 27$ will all converge to the origin. For the other solutions one can define a mapping P given by

$$P(x, y, 27) = (c \cdot \text{sgn}(y), x|y|^{3/2}, |y|^{1/2}) \tag{4.4}$$

with c a constant chosen such that $\mathcal{G}^+, \mathcal{G}^-$, is mapped onto $\mathcal{F}_+, \mathcal{F}_-$, respectively, [14]. This corresponds to the splitting mechanism of property 3. Observe that this map also satisfies property 1.

From the exponents of P in equation 4.4 we observe that $1/2 < 1 < 3/2$ hence we have a contraction in x - direction and an expansion in y -direction inside T . This is also made explicit by

$$\lim_{y \rightarrow 0} \frac{\partial P_2}{\partial x} = 0, \quad \lim_{y \rightarrow 0} \frac{\partial P_3}{\partial y} = \infty.$$

Thus the mapping P performs a stretch and split operation.

In accordance to property 3 we will need to return the solution curves back to R by a merging mechanism. This is done by placing two equilibrium points in the plane $z = 27$: one at $Q_- = (-10, -20, 27)$ and one at $Q_+ = (10, -20, 27)$. Assume that Q_{\pm} has one negative and two complex conjugate eigenvalues, such that solutions will spiral around the equilibria in accordance with property 2. This spiralling operation is performed by the mapping $D : \mathcal{F}_{\pm} \rightarrow \mathcal{G}_{\pm}$ as indicated in figure 4.13.

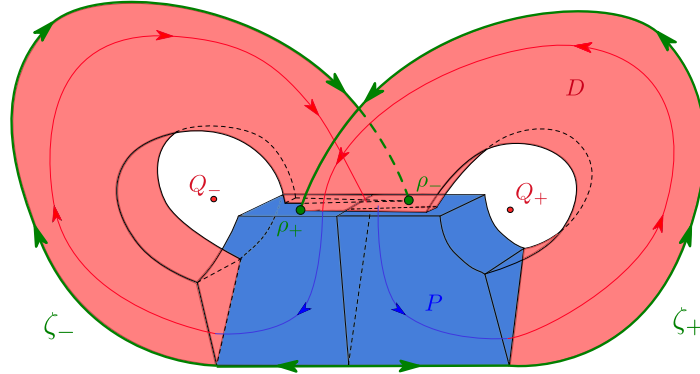


Figure 4.13: The mapping $D : \mathcal{F}_{\pm} \rightarrow \mathcal{G}_{\pm}$ and $P : \mathcal{G} \rightarrow \mathcal{F}_{\pm}$. The solution curves ζ_{\pm} correspond to the unstable curve at the origin, these will intersect the plane \mathcal{G} at ρ_{\pm} .

In figure 4.13 we have also indicated the solution curves ζ_{\pm} corresponding to the unstable curve at the origin. ζ_{\pm} move upwards around \mathcal{G} after which they will intersect \mathcal{G} at the point $\rho^{\pm} = (\pm x^*, \mp y^*)$. These unstable solution system will play an important role in the discussion of the dynamics of the model for the Lorenz system.

4.4.2 Return map

We can now define the return map $\Psi = D \circ P : \mathcal{G} \rightarrow \mathcal{G}_{\pm}$. This map returns points inside \mathcal{G}_{\pm} by following their solution curve around \mathcal{G}_{\pm} for a single rotation. Hence this mapping is called a return map, although it doesn't 'return' the line $y = 0, z = 27$.

Recall that Σ is the plane given by $|x|, |y| \leq 20, z = 27$. We make some assumptions on how the solution behave in this plane.

- The lines $y = \pm 20, z = 27$ on the sides of Σ correspond to the stable curves at Q_{\pm} .
- Solution curves shall enter perpendicularly to Σ . Thus since by the choice of eigenvalues and by the conditions that no solution curves can intersect the stable curve at the edge of Σ , solution curves spiral away from Q_{\pm} .

We can now extend the map Ψ to complete Σ . Following Hirsch in [14] we make the following assumptions.

- **Return condition.** Define $\Sigma_+ = \Sigma \cap \{y > 0\}$ and $\Sigma_- = \Sigma \cap \{y < 0\}$. Assume that all solutions entering any point Σ_{\pm} will return to Σ_{\pm} in forward time. Thus let us define the time-one map $\Psi : \Sigma_+ \cup \Sigma_- \rightarrow \Sigma$ which exactly describes the properties indicated in figure 4.14. By symmetry of the model we assume that $\Psi(x, y) = -\Psi(-x, -y)$.
- **Contracting and Expanding.** Assume that for $\mu \neq 0$ the Ψ maps the line $y = \mu$ in Σ to the line $y = g(\mu)$ such that it is contracted in the x -direction. Assume that Ψ expands in the

y -direction such that $g'(y) > \sqrt{2}$; thus Σ_{\pm} will be expanded in the y -direction by a factor greater than $\sqrt{2}$.

- **Hyperbolicity condition.** Let us finally assume that $D\Psi$ maps vectors in Σ_{\pm} whose slopes are ± 1 to vectors with a bigger slope $v > 1$. This implies that sectors given by $|y| \geq |x|$ shall be mapped under Ψ to areas with slopes of bigger magnitude.

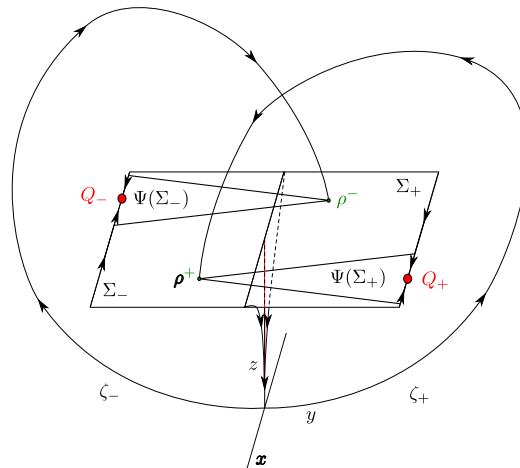


Figure 4.14: A schematic view of the Lorenz model on the plane Σ .

These assumptions mean that

$$\Psi(x, y) = (f(x, y), g(y)).$$

By the contracting and expanding we have that $g'(y) > \sqrt{2}$ and $0 < \partial f(x, y)/\partial x < c < 1$. Furthermore the hyperbolicity condition implies that Ψ contracts area, to see this consider the tangent plane given by $|y| \geq |x|$ as indicated in figure 4.15. By the hyperbolicity condition we have that Ψ maps the tangent plane to even steeper slopes. In doing so the area is contracted, hence this will correspond to property 4 of the Lorenz system.

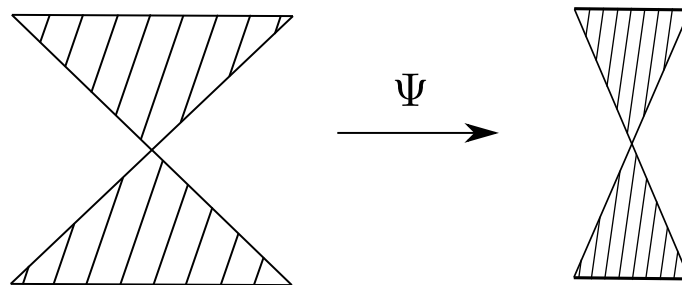


Figure 4.15: Schematic view of the hyperbolicity condition. The hyperbolicity condition maps the lines $|y| = |x|$ to steeper slopes and consequently contracts area.

4.4.3 The Tucker attractor of the Lorenz model exists

Before we continue observe that $\Psi(x, 0)$ is not defined, however we do have that

$$\lim_{y \rightarrow 0^\pm} \Psi(x, y) = \rho^\pm.$$

To find the attractor we first need to find a trapping region, which we will refer to as R . Take $R \subset \Sigma$ with $|y| \leq y^*$. Let us define $R_\pm = R \cap \Sigma_\pm$. By the expanding and contraction condition one can prove that this is a trapping region [14]. The action on the trapping region is displayed in figure 4.16.

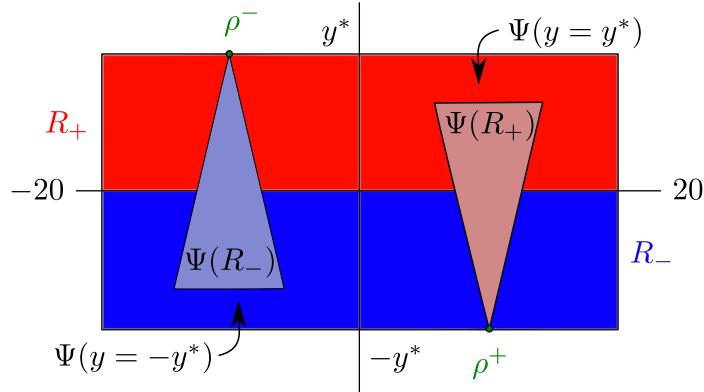


Figure 4.16: Action on the trapping region R : R gets split into two triangles whose lower and upper sides respectively get mapped further away from the lines $-y^*, y^*$.

We will show that

$$A = \bigcap_{n=0}^{\infty} \overline{\Psi^n(R)}$$

is a Tucker attractor generated by the map Ψ . Moreover by proving this one obtains that

$$\mathcal{A} = \bigcup_{t \in \mathbb{R}} \Phi_t(A) \cup \{(0, 0, 0)\}$$

is an attractor for the model of the Lorenz system. We now come to the main theorem of this section:

Theorem 4.4.1 (\mathcal{A} is an attractor) \mathcal{A} is an attractor of the model of the Lorenz system.

Proof. The proof that \mathcal{A} is a Tucker attractor for the flow follows immediately if we prove that A is a Tucker attractor for the map Ψ .

We first need to prove that \mathcal{A} is closed and invariant. We have that A is closed. We actually don't have that A is invariant since the line $y = 0$ is undefined for the mapping Ψ this is however not the case for the flow, since the solutions which pass through $y = 0$ are defined.

For any $(x, y) \in \text{Int}(\Sigma)$, we have $\exists n > 0$ such that $\Psi^n(x, y) \in R$, this implies that

$$\bigcap_{n=0}^{\infty} \Psi^n(\text{Int}(\Sigma)) \subset A.$$

Since $\text{Int}(\Sigma) \supset \Psi(R)$ we already have the ' \supset ' case. Thus condition two of Tucker attractor is also satisfied:

$$A = \bigcap_{n=0}^{\infty} \Psi^n(\text{Int}(\Sigma)).$$

The transitivity property is a bit harder. We need to have that for $p_1, p_2 \in A$ and W_j open neighbourhoods of the p_j with $j = 1, 2$ that there exists a solution curve connecting a point in W_1 to a point in W_2 such that $\Psi^n(W_1) \cap W_2 \neq \emptyset$ for $n \geq 0$. A key-role in this proof is played by the expansion in y -direction. Take $U \subset R$ a finite collection of sets, then we define the projection of U onto the y -axis by $\Pi_y(U)$. The length of $\Pi_y(U)$ shall then be denoted by $\ell_y(U)$, this is well-defined by the definition of U . Observe that if $U = V_1 \cup V_2$ where $V_1 \cap V_2 = \emptyset$ then $\ell_y(U) = \ell_y(V_1) + \ell_y(V_2)$. Before being able to continue the proof we will be needing a lemma.

Lemma 4.4.1 *For all $W \subset R$, $\exists n > 0$ such that $\Pi_y(\Psi^n(W))$ is the interval $[-y^*, y^*]$ i.e. $\Psi^n(W)$ meets each line $y = c$ in R*

Proof. Let us first look at a special case: assume that W' stretches from the line $y = 0$ to $y = \pm y^*$. Thus we have that $\ell_y(W') = y^*$. Now $\Psi(W')$ will be connected, thus by the expansion in y direction we have that $\ell_y(\Psi(W')) > \sqrt{2}y^*$. $\Psi(W')$ will cross the line $y = 0$, since it cannot exceed y^* . Thus if we apply Ψ another time to $\Psi(W')$, we will have that $\ell_y(\Psi^2(W')) > 2y^*$. Observe $\Psi^2(W')$ consists out of two parts contained in Σ^+ extending to ρ^- and one in Σ^- extending to ρ^+ , thus the $\Psi^2(W')$ shall not leave the rectangle R . We may now conclude that $\Pi(\Psi^2(W')) = [-y^*, y^*]$.

The generalization follows from the special case. Suppose now that W is indeed connected and does not cross $y = 0$. We have seen that by applying Ψ we will increase the length by a factor of $\sqrt{2}$. Observe that a splitting into two connected sets will only take place if we cross $y = 0$. Thus the length of W under mapping of Ψ^n will increase until it crosses the line $y = 0$, let us denote the resulting set by \hat{W} . Then there exists a pair of connected sets \hat{W}^\pm with $\hat{W}^\pm \subset \{R^\pm \cap \hat{W}\}$ and $\ell_y(W) = \ell_y(\hat{W}^+ \cup \hat{W}^-)$. For $\Psi(\hat{W}^\pm)$ we have that they extend to the tips of ρ^\pm since $y = 0$ intersects \hat{W} . If one of the sets $\Psi(\hat{W}^\pm)$, hits $y = 0$ then we are done because of the special case. If this is not the case then just apply Ψ again and they will grow without bound. Thus $\exists n > 0$ such that $\Pi(\Psi^n(\hat{W})) = [-y^*, y^*]$. With the previous result we also have immediately proven the case when the initial set W does cross $y = 0$. \square

Continuation of theorem 4.4.1. We can now continue the proof by making use of the above lemma. Observe that by contraction in the x -direction we have that

$$|\Psi^k(x_1, y) - \Psi^k(x_2, y)| \leq c^k |x_1 - x_2|.$$

Let us for now assume that $W_2 = B_\epsilon(p_2)$. We have that the width of R is equal to 40. Let us choose $m \geq 0$ such that $40c^m < \epsilon$. We know that $\Psi^{-m}(p_2)$ is well-defined since $p_2 \in \Lambda$. Now define $(\xi, \eta) = \Psi^{-m}(p_2)$. As a consequence of lemma 4.4.1 we have that

$$\Pi_y(\Psi^n(W_1)) = [-y^*, y^*],$$

thus we may choose $(\xi_1, \eta) \in \Psi^n(W_1)$. Define $(\tilde{x}, \tilde{y}) = \Psi^n(\tilde{x}, \tilde{y})$ with $(\tilde{x}, \tilde{y}) \in W_1$. Then we can obtain

$$|\Psi^{m+n}(\tilde{x}, \tilde{y}) - P_2| = |\Psi^m(\xi_1, \eta) - P_2| = |\Psi^m(\xi_1, \eta) - \Psi(\xi, \eta)| \leq 40c^m < \epsilon.$$

Thus we can conclude that there is a solution beginning in W_1 passing through W_2 . \square

4.4.4 One-dimensional dynamics

With the map Ψ we have reduced the dynamics from \mathbb{R}^3 to \mathbb{R}^2 , but we can even reduce the dynamics further. We have that if two points share the same y -coordinate in Σ then they will be mapped onto the points whose y -coordinates are given by $g(y)$ and thus are the same again. Furthermore a contraction between these two points in x -direction shall take place. This already gives an indication that we only need to keep track of the lines $y = \text{constant}$, which implies that the dynamics of Ψ are determined by the one-dimensional dynamics of $g(y)$.

Let the interval I be given by $[-y^*, y^*]$. We have that $g(y)$ will be defined for $y \in I \setminus \{0\}$. By the assumption on Ψ we have that $g'(y) > \sqrt{2}$, that $0 < g(y^*) < y^*$ and $-y^* < g(-y^*) < 0$ and also that $\lim_{y \rightarrow 0^\pm} g(y) = \mp y^*$. We are interested in the dynamics of the time-one map g hence we will be interested in the corresponding orbit, thus define

$$g : y_{n-1} \mapsto y_n, \quad y_{n-1} \in I.$$

We come to the iteration graph corresponding to g , presented in figure 4.17.

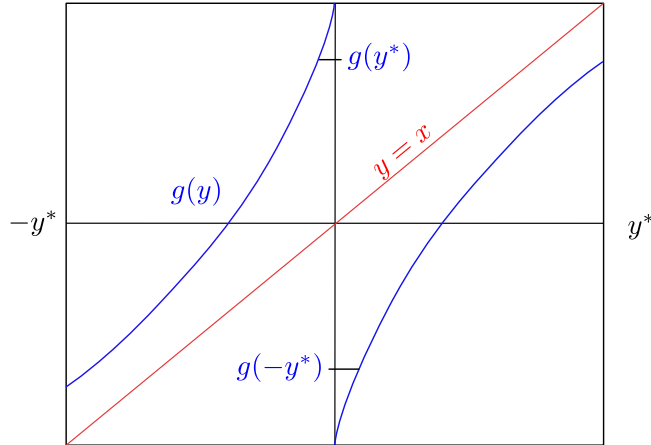


Figure 4.17: Iteration graph of $g: g(y_n)$ against y_n .

By graphical iteration one can then get an idea how the orbits corresponding to g and g^{-1} behave, see figure 4.18.

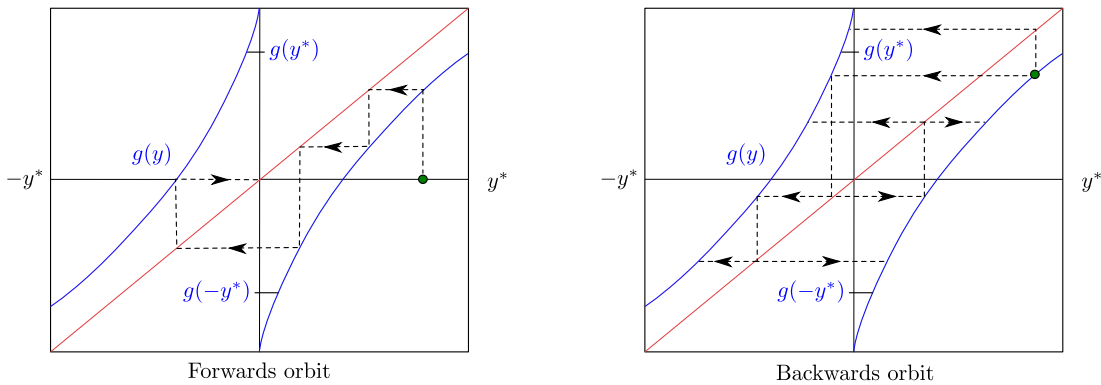


Figure 4.18: A forward orbit and backward orbits. Observe with the forward orbit that it ends as soon as $g^n(y_0) = 0$. Observe with the backward orbits that the points in the interval $[g(-y^*), g(y^*)]$ have two images under g^{-1} , while the points in the interval $(-y^*, g(-y^*))$ and $(g(y^*), y^*)$ only have one preimage.

Forward orbits are uniquely determined and end as soon as $g^n(y_0) = 0$. Backwards orbits have two preimages in the interval $[g(-y^*), g(y^*)]$, while the points in the interval $(-y^*, g(-y^*))$ and $(g(y^*), y^*)$ only have one preimage.

Lemma 4.4.2 *For the mapping g and $y_0 \in \text{Int}(I)$ we have that*

1. *The forward orbit corresponding to y_0 is uniquely determined.*
2. *There exist infinitely many distinct backward orbits corresponding to y_0 .*

Proof. Property 1 follows directly from figure 4.17.

Now Property 2, take a backward orbit corresponding to y_0 i.e. $\{y_0, y_{-1}, \dots\}$. We have that for a point $y_0 \in (-y^*, y^*)$ there exist infinite many distinct backward orbits. It is given that y_{-n} has two preimages if $y_n \in [g(-y^*), g(y^*)]$ and one if $y_n \in (-y^*, g(-y^*)) \cup (g(y^*), y^*)$. If y_{-n} has indeed only a single preimage then according to figure 4.17 we have that y_{-n-1} is contained in $[g(-y^*), g(y^*)]$ and hence has two preimages. We have just a single case remaining: what if $y_{-n} = \pm y^*$? If this is the case then we have that y_{-n+1} has two preimages one of which is the endpoint $\pm y^*$ and the other one isn't equal to one of the endpoints. Thus we may conclude that there exist infinite many distinct backward orbits. \square

We will now connect the above lemma to the Tucker attractor A . We claim that each of these backward orbits corresponding to y_0 has a unique point in $A \cap \{y = y_0\}$. The main idea of the proof is to create a nested intersection which verifies the above claim.

Take a line $y = y_{-n}$ in R represented by J_{-n} , and corresponding to a single backwards orbit. We then have that $\Psi^n(J_{-n})$ is a closed subinterval in J_0 for each n . We have that

$$\bigcap_{n \geq 0} \Psi^n(J_{-n}) \tag{4.5}$$

is non-empty since $\Psi^n(J_{-n}) \subset J_0$. Furthermore this is a nested intersection since $\Psi^n(J_{-n}) \subset J_{-n+1}$. By construction we have that the points in the nested intersection have backward orbit corresponding to y_0 , furthermore the intersection of two nested intersections corresponding to two different backward orbits will be equal to the empty set.

We have that equation 4.5 contains a unique point of intersection of all the nested sequence since the length of the interval y_{-n} will be reduced to zero due to contraction in the x -direction (by a factor $0 < c < 1$).

These results can be extended to the Tucker attractor \mathcal{A} in R . This give us an insight into the structure of \mathcal{A} .

Proposition 4.4.1 *The attractor \mathcal{A} for the Lorenz system meets each of the lines in R , $y = y_0 \neq y^*$, in infinitely many distinct points. In forward time all of the solution curves through each point on this line either:*

1. *Meet the line $y = 0$ and consequently tend to the equilibrium at the origin.*
2. *Continually reintersect R , with the property that the distance between the intersection points on the line $y = y_n$ tending to 0 as time increases.*

We can also get an insight into the chaos present in this system by using one-dimensional dynamics. An indication of chaos can already be seen by exploring the structure of $\Psi^k(R)$ with $k > 0$. The structure of $\Psi(R)$ was already given; let us now look at $\Psi^2(R)$. We know that points in a neighbourhood of the line $y = 0$ will get mapped onto $\pm y^*$. Using once again the fact that $y \in [g(-y^*), g(y^*)]$ has two preimages and $y \in (-y^*, g(-y^*)) \cup (g(y^*), y^*)$ has one preimage, we obtain figure 4.19.

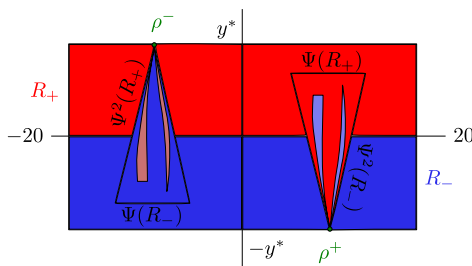


Figure 4.19: The chaotic process of folding (or bending) revealed in the model for the Lorenz-attractor.

Now the presence of chaos is made visible. Using once again the kneading of dough paradigm we see that the mapping Ψ performs a stretching and folding on the ‘dough’, R . One might also suggest the correspondence of figure 4.17 with the period doubling map, although note that these two figures are not conjugate.

Supplying the evidence with concrete proof, we have the following proposition.

Proposition 4.4.2 *The function g has sensitive dependence on initial values.*

Proof. This follows from the fact that $g'(y) > \sqrt{2}$. The full proof can be found in [14].

This sensitive dependence will then be seen back in A and this behaviour will be seen back in \mathcal{A} for a neighbourhood of R .

Let us state one more proposition which results from the dynamics of g :

Proposition 4.4.3 *The periodic points of Ψ are dense in A .*

Sketch of proof. We will only present the proof that periodic points of g are dense in $[-y^*, y^*]$, the proof that this extends to Ψ can be found in [14].

Take a subset $J \subset [-y^*, y^*] \setminus \{0\}$. Similar to the proof in lemma 4.4.1 we can prove that there exists an $n > 0$ such that g^n is a bijective map from the subinterval $J' \subset J$ onto either $(-y^*, 0]$ or $[0, y^*)$. Depending on the J' we have that either $J' \subset g^n(J')$ or $J' \subset g^{n+1}(J')$. Thus we have by Brouwer’s fixed point theorem that $g^n(J')$ or $g^{n+1}(J')$ has a fixed point and hence g has a periodic point. Since J , was any subset, we have proved that the periodic points of g are dense in $[-y^*, y^*]$.

We end this section with a summary of the properties that we have proven for the mapping Ψ restricted to the attractor A .

Theorem 4.4.2 (The dynamics of the model of the Lorenz attractor) *The evolution operator restricted to the attractor A of the Lorenz model has the following properties*

1. Ψ has sensitive dependence on initial values.
2. Periodic points of Ψ are dense in A .
3. Ψ is transitive on A .

Chapter 5

Concluding remarks

Our journey through the dynamics of chaotic systems and fractals has now come to an end. However let us take a look back at the path we have trodden.

We began with an exploration of the Hénon and Lozi map in chapter 1. We came across the famous conjecture that $\overline{W^u(p)} = \mathcal{H}$. Concluding that the Hénon map is perhaps more complicated than initially thought we aimed to investigate a simplification: the piecewise linear Lozi map. For the Lozi map we could indeed prove that for a set in the parameter plane $\overline{W^u(p)} = \mathcal{L}_{a,b}$ holds. Hénon and Lozi maps for some parameter choices have sensitive dependence on initial values, this is due to the bending which takes place at each iteration. Furthermore this bending can lead to attractors which are fractals. We continued with a numerical investigation and showed that by making use of Lyapunov exponents we can determine the stability of dynamical systems and also give an approximation of the dimension. This brought us to the Lyapunov bifurcations diagrams of the Hénon and Lozi map with which we could determine the behaviour in the parameter plane. It is shame that there was no time left for an extensive discussion of the symmetry in the bifurcation diagrams, however these will be presented in further publication. Finally at the end of this chapter we investigated the possibility of multiple attractors and we saw that this behaviour is not only characteristic to theoretical models such as the Hénon map, but also in a physical experiment: the pendulum with three magnets.

Continuing to chapter 3; we began with the discussion of the complex Newton method. By numerically generating the basins of attraction we concluded that the complex Newton method in some cases won't converge to a root for a set of full measure, in contrast to the real Newton method. We also saw the complexity of the fractal basin boundaries of the Newton method. This doesn't just apply to the boundary of the basins of attraction of the Newton method, but to most basin boundaries of rational polynomials, i.e. Julia sets. In the numerical discussion of Julia sets the construction of field lines and equipotential curves played an important role. However we could also use the equipotential curves and field lines for theoretical purposes, this brings us to theorem 3.2.6 in which we proved that for complex functions we can divide the Julia sets into two sets: connected and Cantor sets. This leads to the behaviour of the Julia set, J_c , in the parameter plane: the Mandelbrot. We discussed the external dynamics by making use of equipotential curves and field lines, and the internal dynamics by investigating the attractive periods of the J_c corresponding to the buds. Finally at the end of this chapter we explored a similarity between the Mandelbrot set and Julia sets in a neighbourhood of Misiurewicz points.

The systems investigated in chapter 1 and 2 has state spaces which were subsets of \mathbb{R} and \mathbb{R}^2 (since $\mathbb{R}^2 \cong \mathbb{C}$)¹. In the chapter 4 we studied the Lorenz system which is a system with state space \mathbb{R}^3 . Following the discussion of Lorenz himself in [24] we proved numerically that this system has sensitive dependence on initial values by decreasing the dynamics from \mathbb{R}^3 to \mathbb{R} . This numerical idea also

¹The pendulum and three magnets is an exception to this since it has state space $M = \mathbb{R}^4$

extends to the theoretical model of the Lorenz system in which we observed that by reducing the three-dimensional dynamics to the two dimensional dynamics we could prove that the model was a Tucker attractor, and by reducing it even further, to one-dimensional dynamics we could proof the presence chaos. It was a pity that we could not investigate the Lorenz system in the parameter plane as we did with the other systems.

We have now given an extensive investigation on the dynamics of chaotic system and fractals. However we won't deceive the reader in stating that this is complete. Furthermore we will go as far as stating that this is far from complete. So much research has been done on the treated subjects , that it would be impossible to contain all this information in this humble thesis. Thus we advise the reader, the journeyman in the world of chaotic system and fractals, after perhaps a short rest, to continue his journey without guidance of this work (or perhaps with, we refer to the Bibliography which contains many suitable literature) to enter a world of ever expanding horizons.

Appendix A

Lozi-map

In this Appendix we present the smoothed Lozi map and proof the statement $\mathcal{L}_{a,b} = \overline{W^u(X)}$.

A.1 Smoothed Lozi mapping

Recall the Lozi map

$$L_b^a : (x, y) \mapsto (1 - a|x| + y, bx).$$

Preserving some of the properties of the Hénon mapping and Lozi mapping we create a smoothed L_b^a given by

$$L_{a,b}^\epsilon : (x, y) \mapsto (1 - aS_\epsilon(x) + y, bx).$$

Where $a, b \in \mathbb{R}$ and $S_\epsilon : \mathbb{R} \rightarrow \mathbb{R}$, the smoother, is given by

$$S_\epsilon : x \mapsto S_\epsilon(x) = \begin{cases} |x| & \text{if } |x| \geq \epsilon \\ (x^2/2\epsilon) + \epsilon/2 & \text{if } |x| < \epsilon \end{cases}$$

with $0 < \epsilon < 1$.

We see that for $|x| \geq \epsilon$ the properties of the Lozi mapping are preserved. For the values $|x| < \epsilon$ we smooth the map with an x^2 -term which corresponds to a Hénon-like map. As we decrease ϵ $L_{a,b}^\epsilon$ will approximate $L_{a,b}$ since

$$\lim_{\epsilon \rightarrow 0^+} S_\epsilon(x) = |x|.$$

Let us now numerically verify that the Lozi mapping is indeed similar to $L_{a,b}^\epsilon$ for ϵ sufficiently small. Taking parameters corresponding to the Lozi attractor $a = 1.7$, $b = 0.5$, we obtain figure A.1.

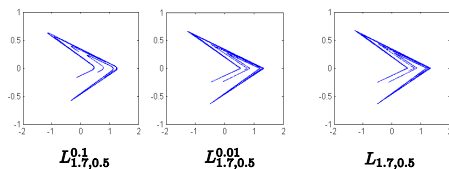


Figure A.1: Left we have used the mapping $L_{1.7,0.5}^\epsilon$ with $\epsilon = 0.1$ and $\epsilon = 0.01$ and right we have used the mapping $L_{1.7,0.5}$. Observe how $L_{1.7,0.5}^\epsilon$ bends the endpoints such that they become differentiable. As ϵ is decreased in $L_{1.7,0.5}^\epsilon$ the corresponding attractor approximates the attractor corresponding to $L_{1.7,0.5}$ really well.

We observe that at the endpoints the $L_{1.7,0.5}^\epsilon$ bends the attractor such that becomes differentiable. As ϵ is decreased the attractor corresponding to the mapping $L_{1.7,0.5}^\epsilon$ begins to resemble more and more the the attractor corresponding to the mapping $L_{1.7,0.5}$.

For a more extensive research on the smoothing Lozi map we refer to [3]

A.2 Proof $\mathcal{L}_{a,b} = \overline{W^u}(X)$

We will proof that $\mathcal{L}_{a,b} = \overline{W^u}(X)$ for certain parameter values a, b following the original paper of Misiurewicz on this subject [29]. We won't actually proof that $\overline{W^u}(X)$ corresponds to an attractor but assume that for a trapping region G we have that $\bigcap_{n=0}^{\infty} L^n(G) = \mathcal{L}_{a,b}$. The proof that $\bigcap_{n=0}^{\infty} L^n(G)$ is an attractor can be found in [29].

First some things concerning notations. We will replace the overline in $\overline{W^u}(X)$ with the closure symbol i.e. $\text{Cl}(W^u(X))$. We will uses overlines to indicate the lines which connect vertices. Furthermore instead of $L_{a,b}$ we will just be writing L

We use various assumptions on the parameter a, b for different proofs. These assumptions are listed below and visualized in figure A.2.

1. $0 < b < 1, a > 0$
2. $a > b + 1$
3. $2a + b < 4$
4. $a > \frac{1}{2}\sqrt{3b^2 + 4 + \sqrt{(3b^2 + 4)^2 - 32b^3}}$
5. $b < \frac{a^2 - 1}{2a + 1}$
6. $a\sqrt{2} > b + 2$

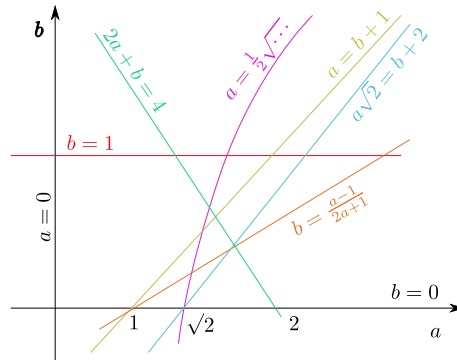


Figure A.2: The six assumptions that are made on the Lorenz-mapping to proof that $\mathcal{L}_{a,b} = \overline{W^u}(X)$.

From figure A.2 observe that some of these assumptions imply each other: (1)(5) \rightarrow (2), (1)(6) \rightarrow (2), and (1)(6) \rightarrow (4)

We restrict our attentions to the parameter plane given by (1) the rest of the assumptions are needed for the coming proofs. One can also prove the results for other values of a, b we will refer the reader once again to [29].

Before finally beginning with the proof let us note that the last assumptions (6) isn't used in the proof $\mathcal{L}_{a,b} = \text{Cl}(W^u(X))$. It is used in proving that $\mathcal{L}_{a,b}$ is an attractor, note that the parameters for Lozi attractor ($a = 1.7, b = 0.5$) don't satisfy this assumption.

Elementary properties

We assume that (1) holds and that $a + b > 1$. We have that L is a homeomorphism, which maps points from the left half plane into the right half plane and vice versa. We have two fixed points given by :

$$X = \left(\frac{1}{1+a-b}, \frac{b}{1+a-b} \right) \quad \text{and} \quad Y = \left(\frac{1}{a-1+b}, \frac{b}{a-1+b} \right).$$

Both are saddle points. X corresponds to the saddle fixed point in the Lozi attractor. Since the Lozi map is piecewise linear the local stable and unstable manifolds corresponding X can be found by calculating the eigenvectors of the derivative matrix at X . The local unstable manifold, in the upper half plane, consists out of two parts: one starts from X and intersects the x -axis at the point

$$Z = \left(\frac{(2+a+\sqrt{a^2+4b})}{2(1+a-b)}, 0 \right),$$

the other part shall move from the fixed point into infinity. The stable manifold, in the left half plane, is perpendicular to the unstable manifold and consists also out of two parts: one starts in X until it intersects the y -axis at the point

$$T = \left(0, \frac{2b-a-\sqrt{a^2+4b}}{2(1+a-b)} \right)$$

and the other part starts in X and goes to infinity.

The previous statements are visualized in figure A.2.

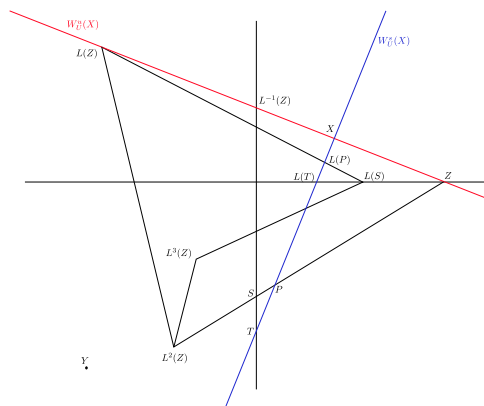


Figure A.3: Schematic view on the Lozi mapping. X is the saddle fixed point in the Lozi attractor. The corresponding local stable and unstable manifolds ($W_U^s(X)$ and $W_U^u(X)$) are linear functions.

It is important to keep this figure in mind when reading the coming proofs.

Trapping region

We begin by finding a trapping region. The triangle $ZL(Z)L^2(Z)$ will be denoted by F .

Proposition A.2.1 *If a, b satisfy (1)(2)(3), we will have that $L(F) \subseteq F$*

Proof. From assumption (1) and (2) we have that Z must lie to the right of the origin. From this it follows that $L(Z)$ must be contained in the second quadrant. It then follows that $L^2(Z)$ must be contained in the lower half plane, since the corresponding y -coordinate is smaller than that of Z .

We have already seen how a transformation can be splitted in subtransformations with the Hénon mapping. We can split the Lozi mapping into two parts $L(x, y) = L_1(L_2(x, y))$ with

$$L_1(x, y) = \left(x - \frac{a}{b}|y|, y \right), \quad L_2(x, y) = (1 + y, bx). \quad (\text{A.1})$$

L_1 corresponds to shifting points to the left with the exception of those on the x -axis and L_2 corresponds to a shift plus reflection.

Let us denote the intersection of the lines $\overline{L(Z)L^2(Z)} \cup \overline{L^2(Z)Z}$ with the y -axis by S . Since the y coordinate of $L^{-1}(Z)$ bounds the y coordinate of S it follows that $L(S)$ must lie left from Z . If we apply L to S , then by equation A.1 we have that $L(S) = L_1(L_2(S))$. $L_2(S)$ lies on the x -axis, thus $L(S)$ lies right to of $\overline{L^2(Z)L^3(Z)}$ or $\overline{L^3(Z)L(Z)}$. Therefore if $L^3(Z) \in F$ then $L(S) \in F$.

$L(F)$ is a polygon with vertices: $Z, L(Z), L^2(Z), L^3(Z)$ and $L(S)$. Thus if $L^3(Z) \in F$ then we have that $L(F) \subset F$.

Due to the linearity of L the set $L(F)$ lies in between $\overline{L^2(Z)Z}$ and $\overline{L(Z)Z}$. Thus we must have that $L(Z)$ lies to the right of $L^2(Z)L(Z)$ to finish the proof. This however needs a few pages of tiresome computations we will omit these and present the result of Misiurewicz, which states that if $L^2(Z)$ lies in the left half plane, the problem reduces to the inequality $(4 - 2a - b)(1 + a - b)^2 > 0$, which is indeed true by the assumptions (1)(2)(3). \square

We state some consequences of proposition A.2.1. We have that

$$L(\overline{L(Z)L^2(Z)} \cup \overline{L^2(Z)Z}) \setminus \{L(Z), Z\} \subset \text{Int}(F) \quad \text{and} \quad L(\overline{L(Z)L^{-1}(Z)}) = \overline{L^2(Z)Z}.$$

It follows from $L^{-1}(F) \subset L^{-4}(F)$ and the previous statements that $L^{-4}(F)$ is an open neighbourhood of $\overline{ZL^2(Z)} \cup \overline{L(Z)L^2(Z)} \cup \overline{L(Z)L^{-1}(Z)}$. We know that $\overline{L^{-1}(Z)Z}$ belongs to the local unstable manifold, therefore $L^{-1}(\overline{L^{-1}(Z)Z}) \subset \overline{L^{-1}(Z)Z}$. Thus there exists a rectangle R inside the first quadrant with sides parallel to the eigenvector corresponding the unstable manifold such that

$$\text{Int}(R) \supset \overline{L^{-1}(Z)Z} \setminus L^{-4}(\text{Int}(F)) \quad \text{and} \quad L(R) \subset \text{Int}(R) \cup L^{-4}(\text{Int}(F)).$$

This last statement follows from $\overline{f^{-1}(Z)Z} \subset \text{Int}(R) \cup L^{-4}(\text{Int}(F))$.

Define $G = R \cup L^{-4}(F)$, which is a compact neighbourhood of F . We show that this is a trapping region.

Theorem A.2.1 *If a, b satisfy (1)(2)(3), then $L(G) \subset \text{Int}(G)$*

Proof. From the definition of G it follows that $L(R) \subset \text{Int}(G)$. We have that $L^4(R) \supset L^4(\text{Int}(R)) \supset L^4(\overline{L^{-1}(Z)Z} \setminus L^{-4}(\text{Int}(F))) \supset \overline{ZL(Z)} \cup \overline{ZL^2(Z)}$, this implies that $L(F \setminus L^4(R)) \subset \text{Int}(F)$. Thus $L(G \setminus R) = L(L^{-4}(F) \setminus R) = L^{-4}(L(F \setminus L^4(R))) \subset L^{-4}(\text{Int}(F)) \subset \text{Int}(G)$. It follows then that $L(G) \subset L(R) \cup L(G \setminus R) \subset \text{Int}(G)$. \square

We now obtain an equality between the images of G and F as the next lemma indicates.

Lemma A.2.1 $\tilde{G} = \tilde{F}$ with $\tilde{G} = \bigcap_{n=0}^{\infty} L^n(G)$ and $\tilde{F} = \bigcap_{n=0}^{\infty} L^n(F)$.

The proof can be found in [29].

Assume now also assumption (4) and (5). By straightforward computation one sees that (4) implies that $L^2(Z)$ must lie left from \overline{XT} , furthermore from assumption (5) we obtain that S lies above T . Thus $\overline{L^2(Z)Z}$ and \overline{XT} intersect each other at the point P shown in the figure A.2. Together with proposition A.2.1 we have that all vertices are located with respect to each as figure A.2 suggests.

Denote the triangle XZP by H_0 and define $H = \bigcup_{n=0}^{\infty} L^n(H_0)$. We will now prove the following proposition.

Proposition A.2.2 *Assume a, b satisfy (1)(3)(4)(5). It follows that*

- a. $\partial H \subset \overline{XP} \cup W^u(X)$.
- b. $L(H) \subset H$.
- c. $H \subset F$.
- d. $\tilde{H} = \bigcap_{n=0}^{\infty} L^n(H)$ is equal to \tilde{F} .

Proof. (a) follows from the fact the \overline{XP} is contained on the local stable manifold and the lines \overline{XZ} and \overline{PZ} lie on the global unstable manifold.

(b), (c) follow immediately from the definition.

Let us now prove (d). Define $H_n = \text{Cl}(L(H_{n-1} \setminus H_0))$. Observe by figure A.2 that H_1 is equal to the triangle $XL(Z)L(P)$. Two vertices of the triangle H_n shall always be contained on the \overline{XP} , however the vertex Z under iteration of L can move to the left or right of \overline{XP} . This means that $H_n = \emptyset$ or H_n is equal to a triangle with one line on \overline{XP} and one vertex equal to $L^n(Z)$.

First look at the case when $H_n \neq \emptyset \forall n \geq 0$. We have that $L(F)$ is equal to the polygon $ZL(Z)L(S)L^3(S)L^2(S)$ thus we have that $L(F) \setminus (H_0 \cup H_1)$ is contained in the lower half plane, implying that all points $L^n(Z)$, with $n \geq 1$, lie in the left half plane. We now know that the $L^n(Z) \in F$ stays in a bounded region hence, since L is also linear hyperbolic in the left half plane, they have to converge to a fixed point in this domain which must be Y ; consequently $Y \in F \subset \text{Int}(G)$. Due to the fact the G is a trapping region which contains the local stable manifold of Y we obtain that $W^u_Y \subset G$, but by computation of the eigenvalues of Y we have that half of $W^u(Y)$ goes to infinity [29] and thus we have a contradiction.

The contradiction implies $\exists k \in \mathbb{N}$ such that $H_n \neq \emptyset$ for $n \leq k$ and $H_n = \emptyset$ for $n > k$. Hence we can rewrite the H as $H = \bigcup_{n=0}^k L^n H_0$, which implies that H is a polygon.

Let us take a look at the images of the line piece $\overline{L(Z)L^2(Z)}$. We have that for $1 \leq n \leq k-1$

$$L^n(\overline{L(Z)L^2(Z)}) = \overline{L^{n+1}(Z)L^{n+2}(Z)}.$$

$L^{k-1}(\overline{L(Z)L^2(Z)})$ will then consist out of two disjoint set sets: one part is contained in H_0 and the other part in an interval which joins $L^k(Z)$ with some point of \overline{XP} in the lower half plane. Since \overline{XP} lies on the stable manifold and due to the fact that points in the fourth quadrant will get mapped in the first quadrant we obtain that $L^k(\overline{L(Z)L^2(Z)})$ is union of two sets: one in H_0 and the other in H_1 ; we obtain that $L^k(\overline{L(Z)L^2(Z)}) \subset H$. We have that $\partial L^k(F) = L^k(\partial F) \subset W^u(X) \cup L^k(\overline{L(Z)L^2(Z)}) \subset H$, and thus since H is polygon and therefore simply connected, $L^k(F) \subset F$, thus we have that $\tilde{F} \subset \tilde{H}$. The reverse inclusion follows from (c). \square

We are now able to proof $\tilde{G} = \text{Cl}(W^u(X))$, which is given below.

Theorem A.2.2 *Let a, b satisfy (1)(3)(4)(5), then $\tilde{G} = \text{Cl}(W^u(X))$.*

Proof. Take $A \notin \text{Cl}(W^u(X))$. Then $\exists \epsilon > 0$ such that $B_{2\epsilon}(A) \cap W^u(X) = \emptyset$. Due to proposition A.2.2 we have that $\partial H \subset \overline{XP} \cup W^u(X) \subset W^s(X) \cup W^u(X)$. Vertices on \overline{XP} will converge to $X \in \text{Cl}(W^u(X))$ for sufficiently large n , thus we have that for sufficiently large n that a ball with center A and radius

ϵ is disjoint from $\partial L^n(H)$. We have that the Lozi mapping is contracting due to the assumption that $b < 1$ which implies that the area of $L^n(H)$ will converge to zero as $n \rightarrow \infty$. Therefore $A \notin L^n(H)$ for n sufficiently large, which implies that $A \notin \tilde{H}$. Thus we have that $A \notin \text{Cl}(W^u(X))$ implies $A \notin \tilde{H}$, which is the same as stating $\tilde{H} \subset \text{Cl}(W^u(X))$

From lemma A.2.1 and proposition A.2.2 (d) we have that $\tilde{H} = \tilde{G}$. We have that $X \in \text{Int}(G)$, since X is a fixed point, then since $L(G) \subset G$ and \tilde{G} is closed, we obtain $\tilde{G} \subset \text{Cl}(W^u(X))$. This completes the proof for we now have that $\tilde{G} = \text{Cl}(W^u(X))$. \square

By our assumption this completes the proof since $\tilde{G} = \mathcal{L}_{a,b}$.

Remarks:

- The region F is not a trapping region since $W_V^u(p)$ is f invariant. For a trapping region we need that the closure is mapped into the interior under the mapping L .
- With the construction of a trapping region in theorem A.2.1 it follows that the Lozi attractor has area zero. The proof is similar to proposition 2.1.1 in which we proved that the Hénon attractor has area zero.

Appendix B

Base three expansion for the Triadic Cantor set

By writing the elements of the triadic Cantor set in terms of base three expansions we can prove that the Cantor set is only identified with base three expansions with digits 0 and 2. We prove this below.

Proposition *Let $x \in [0, 1]$, then x will be contained in the Cantor set if and only if x has a base three expansion using only the digits 0 and 2.*

When working in base three we will write subscript three right of the expansion, for example $1/3 = (0.1)_3$.

Sketch of proof. C is constructed by continuously removing parts of C_n . Let us refer to these parts which are removed from C_{n-1} to C_n as the trema corresponding to C_n . The trema of C_1 is given by the interval $(1/3, 2/3)$. The new endpoints of C_1 with respect to C_0 correspond in base three to

$$1/3 = (0.1)_3 \quad \text{and} \quad 2/3 = (0.1222222 \dots)_3 .$$

Observe now that these endpoints have two representation:

$$1/3 = (0.2222222 \dots)_3 \quad \text{and} \quad 2/3 = (0.2 \dots)_3 .$$

C_1 contains all the point in $[0, 1]$ except those with a one at their first position since the trema corresponds to $(1/3, 2/3)$. The endpoint of C_1 won't be removed since these points have two representations. Continuing in a similar manner we see that the trema's corresponding to C_2 are given by the intervals $(1/9, 2/9)$ and $(7/9, 8/9)$, thus C_2 contains all points without a one in the first and second position. Continuing in this way we indeed obtain that $C = \bigcap_{k=0}^{\infty} C_k$ contains all points in $[0, 1]$ without a one in their base three expansion. \square

A consequence of this proposition and the fact that each real number has at most 2 representations in base 3, is that the Cantor set is uncountable. Which is pretty special since the Cantor set also has also measure zero.

Appendix C

Numerical calculation of Lyapunov exponents

We will now present a short overview how one can numerically calculate Lyapunov exponents by making use Gram-Smidt orthonormalization.

Label the Lyapunov exponents such that $h_1 \geq h_2 \geq \dots \geq h_m$. Let us first concentrate on how to find h_1 .

Finding h_1

Since h_1 is the biggest Lyapunov exponent it will correspond to the biggest eigenvalue. Taking initial value $x^{(0)} \in \mathbb{R}^n$ and an initial perturbation vector $w^{(0)} \in \mathbb{R}^n$. Setting $u^{(0)} := w^{(0)} / \|w^{(0)}\|$. We integrate the J_0 over a single time step $u^{(0)}$

$$w^{(0)} := J_0(x^{(0)})u^{(0)} .$$

Let us continue this process in a similar manner. Define $u^{(i)} := w^{(i)} / \|w^{(i)}\|$, $x^{(i)} := \Phi^1(x^{(i-1)})$ and

$$w^{(i)} := J_i(x^{(i)})u^{(i)} .$$

We then have that $\|w^{(i)}\|$ represents the one step growth in the direction of the biggest eigenvalues. Thus repeating the process n times we will obtain the total expansion or attraction given by

$$r_1^{n-1} \approx \|w^{(n-1)}\| \cdot \dots \cdot \|w^{(0)}\| .$$

Thus the biggest Lyapunov exponent is given by

$$h_1 = \frac{1}{n} \log(\|w^{(n-1)}\|) + \dots + \log(\|w^{(0)}\|) .$$

Finding h_1 and h_2

Let us move on to finding h_2 . The problem that arises is that vectors have the tendency to align in the direction corresponding to the biggest Lyapunov exponent, this problem can be overcome by orthonormalizing the vectors at each iteration. Take initial perturbation $w_1^{(0)}, w_2^{(0)} \in \mathbb{R}^n$ such that $w_1^{(0)} \perp w_2^{(0)}$. Then define $u_k^{(0)} := w_k^{(0)} / \|w_k^{(0)}\|$ with $k = 1, 2$, take an initial value $x^{(0)} \in \mathbb{R}^n$ with $k = 1, 2$ and define $x^{(i)} := \Phi^1(x^{(i-1)})$. Integrating J_i over a single time step $u_k^{(i-1)}$ yields

$$\begin{aligned} z_1^{(i)} &= J_i(x^{(i-1)})u_1^{(i-1)} , \\ z_2^{(i)} &= J_i(x^{(i-1)})u_2^{(i-1)} . \end{aligned}$$

This leads us to the following Gram-Smidt orthonormalization algorithm.

$$\begin{aligned} w_1^{(i)} &= z_1^{(i)} \\ u_1^{(i)} &= w_1^{(i)} / \|w_1^{(i)}\| \\ w_2^{(i)} &= z_2^{(i)} - (z_2^{(i)}, u_1^{(i)})u_1^{(i)} \\ u_2^{(i)} &= w_2^{(i)} / \|w_2^{(i)}\| \end{aligned}$$

Observe that $u_1^{(i)}$ and $u_2^{(i)}$ are orthogonal and that $u_1^{(i)}$ and $u_2^{(i)}$ span the same subspace as $z_1^{(i)}$ and $z_2^{(i)}$.

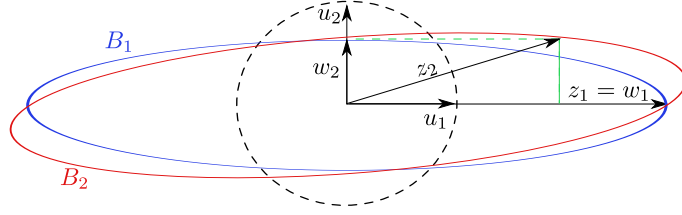


Figure C.1: Gram-Schmidt orthonormalization in progress: The vectors z_1 and z_2 get orthogonalized the result are the vectors w_1 and w_2 respectively. The normalization of w_1, w_2 gives us to the vectors u_1, u_2 respectively. We have also drawn the ellipsoid corresponding to the vectors z_1, z_2 , the ellipsoid B_1 and corresponding to the vectors w_1, w_2 , the ellipsoid B_2

In the figure C.1 we have represented the operation that the orthonormalization algorithm performs. We have removed the superscripts for clarity reasons.

A point of interest is the area of the ellipsoid generated by the vectors w_1 and w_2 , represented in the picture by B_1 . This will be equal to the area of the ellipsoid corresponding to the vectors z_1 and z_2 given by B_2 , since $|\det([z_1 \ z_2])| = |\det([w_1 \ w_2])|$. The area of the vectors z_1 and z_2 corresponds to the average area contraction per iteration, hence rewriting the determinant we obtain that the average area contraction is given by $A = \|w_1\| \|w_2\|$. We also know that the average area contraction per iterate is given by multiplying the two biggest Lyapunov numbers. Hence for n large, we have

$$\begin{aligned} h_1 + h_2 &\approx \frac{1}{n} \log \left(\prod_{k=1}^n \|w_1^{(k)}\| \|w_2^{(k)}\| \right) \\ &= \frac{1}{n} \sum_{k=1}^n \log(\|w_1^{(k)}\| \|w_2^{(k)}\|) \\ &= \frac{1}{n} \sum_{k=1}^n \log(\|w_1^{(k)}\|) + \frac{1}{n} \sum_{k=1}^n \log(\|w_2^{(k)}\|) \\ &\approx h_1 + \frac{1}{n} \sum_{k=1}^n \log(\|w_2^{(k)}\|) \end{aligned}$$

Thus we obtain

$$\begin{aligned} h_1 &\approx \frac{1}{n} \log(\|w_1^{(n-1)}\|) + \dots + \log(\|w_1^{(0)}\|), \\ h_2 &\approx \frac{1}{n} \log(\|w_2^{(n-1)}\|) + \dots + \log(\|w_2^{(0)}\|). \end{aligned}$$

The general case: Gram-Schmidt orthonormalization method.

Generalizing the result we can obtain an algorithm to find all m -Lyapunov exponents simultaneously. Take $u_k^{(0)} := w_k^{(0)} / \|w_k^{(0)}\|$ where $w_k^{(0)}$ with $k = 1, 2, \dots, n$ are initial perturbations perpendicular to each other, take an initial value $x^{(0)} \in \mathbb{R}^n$ with $k = 1, 2$ and define $x^{(i)} := \Phi^1(x^{(i-1)})$. Integrating J_i over a single time step $u_k^{(i-1)}$ yields

$$z_k^{(i)} = J_i(x^{(i-1)})u_k^{(i-1)}$$

This leads us to the following algorithm.

$$\begin{aligned} w_1^{(i)} &= z_1^{(i)} \\ u_1^{(i)} &= w_1^{(i)} / \|w_1^{(i)}\| \\ w_2^{(i)} &= z_2^{(i)} - (z_2^{(i)}, u_1^{(i)})u_1^{(i)} \\ u_2^{(i)} &= w_2^{(i)} / \|w_2^{(i)}\| \\ &\vdots \\ w_m^{(i)} &= z_m^{(i)} - (z_m^{(i)}, u_1^{(i)})u_1^{(i)} - \dots - (z_m^{(i)}, u_{m-1}^{(i)})u_{m-1}^{(i)} \\ u_m^{(i)} &= w_m^{(i)} / \|w_m^{(i)}\| \end{aligned}$$

The volume of the ellipsoid spanned by the set $\{z_1, \dots, z_m\}$ will be given by $V = \|w_1\| \dots \|w_m\|$. Similarly to the case for the two biggest Lyapunov exponents we can generate all the Lyapunov exponents by

$$\begin{aligned} h_1 &\approx \frac{1}{n} \log(\|w_1^{(n-1)}\|) + \dots + \log(\|w_1^{(0)}\|) \\ &\vdots \\ h_m &\approx \frac{1}{n} \log(\|w_m^{(n-1)}\|) + \dots + \log(\|w_m^{(0)}\|). \end{aligned}$$

Appendix D

Riemann sphere

The Riemann sphere, which we have denoted by $\hat{\mathbb{C}}$, is given by \mathbb{C} and ‘the point at infinity’, i.e. $\hat{\mathbb{C}} = \mathbb{C} \cup \{\infty\}$. We shall now present method to construct the Riemann sphere. Take a unit sphere place at the top a N for North-pole and at the bottom a S for South-pole, then place this sphere on \mathbb{C} such that S is placed on the origin and such that N is placed vertically above S , we will refer to the sphere as \mathbb{S}_s^2 . We can construct an injective mapping $h : \mathbb{C} \rightarrow \mathbb{S}_s^2$. We do this by drawing a straight line which connects $z \in \mathbb{C}$ to N , the North-pole, as represented in figure D.1 . The point at which this line intersects the sphere will be $h(z) \in \mathbb{S}_s^2$.

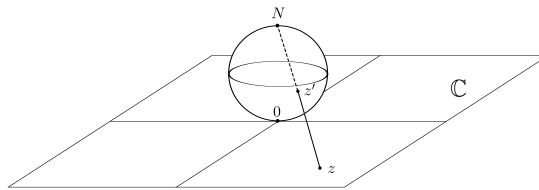


Figure D.1: A point $z \in \mathbb{C}$ is mapped on the sphere, \mathbb{S}_s^2 , by creating a straight line from z to N , the intersection with sphere, z' , corresponds to the point on \mathbb{S}_s^2 .

So how is this connected to $\hat{\mathbb{C}}$? Well we can associate $\hat{\mathbb{C}}$ to \mathbb{S}_s^2 by making use of the mapping h . Easiest is to imagine that we fold \mathbb{C} around \mathbb{S}_s^2 . N will then be associated with the point at infinity, which can be thought of as a gigantic circle at the boundary of \mathbb{C} or equivalently $|z| \rightarrow \infty$.

The reader might be wandering why it is necessary to identify $\hat{\mathbb{C}}$ with a sphere. Well, we know that $\mathbb{C} \cong \mathbb{R}^2$, however by identifying $\hat{\mathbb{C}}$ with a sphere we observe that $\hat{\mathbb{C}}$ isn't isomorphic to \mathbb{R}^2 . Hence it is better to consider $\hat{\mathbb{C}}$ as a sphere instead a plane and the point at infinity.

Remark: Such a mapping h can be made explicit we refer to [23] and from making it explicit of course a lot of interesting properties will follow; we can for example proof that any line or circle under h gets mapped unto a circle on \mathbb{S}_s^2 , furthermore the mapping preserves angles, i.e. conformal. A more extensive treatment can be found in most complex analysis text-books we refer for example to [32].

Appendix E

Path connectedness of $\hat{\mathbb{C}} \setminus K_f$

We will now look into the path connectedness of $\hat{\mathbb{C}} \setminus K_f$ for a complex polynomial f .

Theorem E.1 (Path connectedness of $\hat{\mathbb{C}} \setminus K_f$) *The set $\hat{\mathbb{C}} \setminus K_f$ is pathwise connected.*

Sketch of proof. We only show the proof for the family of Julia sets corresponding to f_c . The general case can be found in [9].

Take $R > 2$. From proposition 3.2.5 we obtain that

$$|f_c(z)| > |z| \quad \forall z \in \mathbb{C} \text{ with } |z| \geq 2.$$

Now let us define

$$Q_0 = \{z \in \mathbb{C} \mid |z| > R\} \cup \{\infty\}.$$

It follows that $f_c^{-1}(Q_0) \subset Q_0$. Due to the choice of the R we will have that $\lim_{n \rightarrow \infty} f_c^n = \infty$ for all $z \in Q_0$. We now have that every bounded orbit cannot enter Q_0 , since then by the previous statement it would be unbounded. Let us define

$$Q_n = f_c^{-n}(Q_0) \quad , \quad n \in \mathbb{Z}_+.$$

See figure E.1 for a visualizations of these Q_n 's.

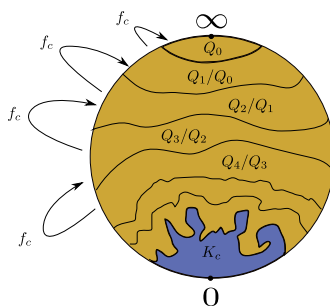


Figure E.1: The Riemann sphere subdivided by Q_{n+1}/Q_n and the filled Julia set, K_c . We have constructed the Q_n in such a way that $Q_n = f_c^{-n}(Q_0)$. Thus as one observes from the figure every point in $\hat{\mathbb{C}}$ is connected to Q_0 and hence path connected to the point at infinity.

It follows that Q_n must be open since f_c is analytic. Q_0 is path connected. A path in Q_0 containing $\{\infty\}$ will be mapped under f_c^{-n} unto a path which also contains infinity, since f_c is complex analytic. Thus all points in $\hat{\mathbb{C}}$ are connected to the point at infinity. Hence we conclude that Q_∞ is pathwise connected. \square .

Appendix F

Self-similarity of Julia sets

We will now give an outline of the proof for theorem 3.3.2 for the periodic case.

We will be first needing a result of Douady and Hubbard about Misiurewicz points.

Proposition F.1 *A Misiurewicz point c has the following properties:*

1. *The orbit corresponding to $f_c(0)$ is eventually repulsive periodic.*
2. *$K_c = J_c$, K_c has no interior.*

For a proof we refer to [16].

Let us once again state Tan Lei's theorem concerning self-similarity of invariant closed sets.

Theorem F.1 (Self-similarity of an invariant closed set A) *Let f be a rational map in \mathbb{C} and A a closed set completely invariant under f . Assume that $z_0 \in \mathbb{C}$ is an eventually repelling periodic point for f , i.e. $f^p(f^\ell(z_0)) = f^\ell(z_0)$ with $p \geq 1$ and $\ell \geq 0$. Then A is ρ -asymptotically self-similar about z_0 , where ρ is given by the eigenvalue of the eventually periodic orbit i.e. $(f^p)'(f^\ell(z_0))$. Then there exists a conformal mapping $\varphi : \overline{U} \rightarrow V$ where U is an open neighbourhood of z_0 , such that the limit model of A at z_0 is given by*

$$\frac{1}{\varphi'(z_0)}\varphi(A \cap \overline{U}).$$

Furthermore, if z_0 is periodic then we can choose the mapping φ in such a way that it satisfies $\varphi'(z_0) = 0$.

In the case that z_0 is eventually repulsive periodic and satisfies $(f^\ell)'(z_0) \neq 0$, the corresponding limit models of A at z_0 and $f^\ell(z_0)$ are equal up to multiplication by a constant given by $f^\ell(z_0)$.

Let us state a lemma which we will make use of in the proof of the above theorem.

Lemma F.1 *Suppose U, V are neighbourhoods of $z_0 \in \mathbb{C}$ and $g : U \rightarrow V$ is a complex analytic map with a fixed point at z_0 i.e. $g(z_0) = z_0$, with $|g'(z_0)| \neq 1, 0$. We will then have that there exists a conformal mapping $\varphi : V \rightarrow U$ with $\varphi(z_0) = 0$, $\varphi'(z_0) = 1$ such that g is (locally) conjugate under φ to its linear part $z \rightarrow \rho z$ given by*

$$\varphi \circ g \circ \varphi^{-1}(z) = \rho z.$$

The explicit form of φ will then be given by

$$\varphi(z) = \lim_{n \rightarrow \infty} \rho^n ((g^{-1})^n(z) - z_0).$$

For a proof we refer to [16].

Sketch of proof for the periodic case theorem F.1. Let us now assume that z_0 is periodic. Then we have that the function f^p has a fixed point at z_0 ; furthermore we have that $|(f^p)'(z_0)| \neq 1, 0$ since we are dealing with a repelling periodic orbit. Now let us define $\rho = (f^p)'(z_0)$; then applying lemma F.1 that there exists a mapping $\varphi : V \rightarrow V_0$ with $\varphi(z_0) = 0$, $\varphi'(z_0) = 1$ such that

$$\varphi \circ f^p(z) = \rho(\varphi(z)).$$

We know that there exists an $r > 0$ such that $\overline{\mathbb{D}_r} \subset V_0$. Let us also define $U = \varphi^{-1}(\mathbb{D}_{r/\rho})$ and $B = \varphi(A \cap \overline{U})$. We are now going to prove that B is ρ -self-similar. We have that $f^p(U) = \varphi^{-1}(\mathbb{D}_r) \subset V$ and $\overline{U} \subset f^p(U)$ since $|\rho| > 1$. Using some elementary topology and the fact the A is f -invariant, one can obtain

$$f^p(A \cap U) \cap U = A \cap U. \quad (\text{F.1})$$

For a proof see lemma 3.4 in [34].

Applying φ to both sides of equation F.1 and using that φ is bijective we obtain that

$$\rho(B \cap \mathbb{D}_{r/\rho}) = B \cap \mathbb{D}_{r/\rho}.$$

Thus $(\rho B)_{r/\rho} = B_{r/\rho}$ and we conclude that B is ρ -self-similar around 0. The last part of the proof follows from the fact that if we have a $\varphi : V \rightarrow V_0$ with $\varphi(z_0) = 0$, $\varphi'(z_0) \neq 0$ then for a closed set $R = A \cap \overline{U} \subset V$, $\varphi(R)$ is asymptotically self-similar around z_0 . We shall not bother the reader with the technical proof (see proposition 2.4 in [34]); we will just state the result that by making use of this property one can obtain that B is asymptotically ρ -self similar about z_0 with the limit model equal to

$$\frac{1}{\varphi'(z_0)} B = B = \varphi(A \cap \overline{U}),$$

since $\varphi'(z_0) = 1$. \square

Bibliography

- [1] K.T. Alligood, T.D. Sauer and J.A. Yorke, *Chaos an Introduction to Dynamical Systems*, Springer-Verlag 1996.
- [2] B. Aulbach, The fundamental existence theorem on invariant fiber bundles, *Journal of Difference equations and Applications* **3** (1998), 501-537.
- [3] M.A. Aziz-Alaoui, C. Robert and C. Grebogi, Dynamics of a Hénon-Lozi-Type Map, *Chaos, Solitons and Fractals* **12** (2001), 2323-2341.
- [4] B. Barna, Über die divergenzpunkte des Newtonschen Verharens zur Bestimmung von Wurzeln algebraischer Gleichungen, *II. Publ. Mathematicae* **4** (1965), 387-397.
- [5] M. Barnsley, *Fractals Everywhere*, Academic Press 1988.
- [6] M. Benedicks and L. Carleson, The Dynamics of the Hénon Map, *Ann. Math* **133** (1991), 73-169.
- [7] B. Bielefeld, Y. Fisher and F.v. Haesler, Computing the Laurent series of the map $\Psi : \mathbb{C} \setminus \overline{\mathbb{D}} \rightarrow \mathbb{C} \setminus M$, *Advances in Applied Mathematics* **14** (1993), 25-38.
- [8] H. Broer, F. Takens, *Dynamical Systems and Chaos*, Epsilon Uitgaven 14 2009.
- [9] H. Brolin, Invariant Sets under Iteration of Rational Functions, *Arkiv für Mathematik* **6** (1965), 103-136.
- [10] H.W. Broer and F. Verhulst (ed.), *Dynamische Systemen en Chaos*, Epsilon Uitgaven 14 1990.
- [11] L.O. Chua and T.S. Parker, *Practical Numerical Algorithms for Chaotic Systems*, Springer-Verlag 1991.
- [12] J.H. Curry, L. Garnett and D. Sullivan, On the Iteration of a Rational Function: Computer Experiments with Newton's Method, *Commum. Math. Phys.* **91** (1983), 267-277.
- [13] R.L. Devaney, *An Introduction to Chaotic Dynamical Systems*, Benjamin, 1986; reprint Addison-Wesly 1989.
- [14] R. L. Devaney, M. W. Hirsch and S. Smale, *Differential Equations, Dynamical systems and an Introduction to chaos*, Elsevier 2004
- [15] A. Douady and J.H. Hubbard, *Exploring the Mandelbrot Set*, Orsay Notes 1984.
- [16] A. Douady and J.H. Hubbard, Étude Dynamique des Polynômes Complexes, *Publication Matheématique d'Orsay* (1985)
- [17] J.P. Eckmann and H. Epstein, Scaling of Mandelbrot Sets generated by Critical Point Preperiodicity, *Commum. Math. Phys.* **101** (1985), 283-289.
- [18] G.A. Edgar, Measure, *Topology and Fractal Geometry*, Springer-Verlag 1992.
- [19] J. Gluckenheimer and R. F. Williams, Structural Stability of Lorenz Attractors, *Publications Mathématiques de l'I.H.E.S.* **50** (1979), 59-72.
- [20] C. Grebogi, E. Ott and J.A. Yorke, Chaotic Attractors in Crises, *Physical Review Letters* **48** (1982), 1507-1510.
- [21] F.v. Haesler and H.O. Peitgen, Newton's Method and Complex Dynamical Systems, *Acta Applicandae Mathematicae* **13** (1988), 3-58.

- [22] M. Hénon, A Two-Dimensional Mapping with a Strange Attractor, *Comm. Math. Phys.* **50** (1976), 69-77.
- [23] H. Jürgens, H. Peitgen and T. D. Saupe, *Chaos and Fractals*, Springer-Verlag 1992.
- [24] E.N. Lorenz, Deterministic Nonperiodic Flow, *Journal of the Atmospheric Sciences* **20** (1963), 130-141.
- [25] W.C. de Melo and J. Palis, *Geometric theory of dynamical systems*, Springer-Verlag 1982.
- [26] J.W. Milnor, *Dynamics in one complex variable*, Annals of Mathematics Studies 2006.
- [27] J.W. Milnor, On the concept of Attractor, *Comm. Math. Phys.* **99** (1985), 177-195.
- [28] M. Misiurewicz and B. Swec, Existence of a Homoclinic Orbit for the Hénon Map, *Comm. Math. Phys.* **75** (1980), 285-291.
- [29] M. Misiurewicz, *Strange attractors for the Lozi Mappings*, 1980.
- [30] J. Pales and F. Takens, *Hyperbolicity and Sensiive Dynamics at Homoclinic Bifurcations*, Cambridge University Press 1993.
- [31] H.O. Peitgen and P.H. Richter, *The Beauty of Fractals*, Springer-Verlag 1986.
- [32] E.B. Saff and A.D. Snider, *Fundamentals of Complex Analysis*, Prentice Hall 2003.
- [33] H.G. Schuster, *Deterministic Chaos, an Introduction*, Physik-Verlag 1984.
- [34] Tan Lei, Similarity between the Mandelbrot Set and Julia sets, *Comm. Math. Phys.* **134** (1990), 587-617.
- [35] Tan Lei (ed.), *The Mandelbrot Set, Theme and Variations*, Cambridge University Press 2000.
- [36] W. Tucker, The Lorenz Attractor Exists, *C.R. Acad. Sci. Paris Ser. I. Math* **328** (1999), 1197-1202.